Graduate Theses & Non-Theses   Student Scholarship

Spring 5-3-2023

A STUDY OF BIOCHAR PRODUCTION VIA CONTINUOUS VACUUM-ASSISTED PYROLYSIS

Max Wohlgenant

A STUDY OF BIOCHAR PRODUCTION

VIA CONTINUOUS VACUUM-ASSISTED PYROLYSIS

By

Max Wohlgenant

A thesis submitted in partial fulfillment of the requirements for the degree of

Master of Science

Materials Science & Engineering

Montana Tech

2023

Abstract

The present study focuses upon the design, fabrication, and feasibility of the bulk production of scientific biochar for mobile delivery. In the 2022 annual report, the National Academies of Science, Engineering, and Medicine recommended the integration of mobile, decentralized reactors that employ flexible manufacturing and circular economic principles. Biochar production, involving the thermal degradation of biomass under an inert atmosphere to yield remediation media is an ideal material to satisfy this recommendation. Many potential application sites, such as abandoned mines, are remote and limit the construction of large infrastructure. The continuous vacuum-assisted pyrolysis (CVAP) reactor was designed to: increase biochar throughput, provide process sensing/automation, and determine the effects of bulk production. Reactor design was completed by modifying existing technologies and incorporating previously unexplored induction heating. Fabrication and design of the CVAP reactor were performed according to industrial safety standards and best-practices. The feasibility of bulk production was evaluated based upon the characteristics of the produced biochar, reactor performance, and project economics. Due to production delays, existing biochar samples were thoroughly characterized to serve as a baseline for future analysis. The performance of the reactor greatly improves upon previous designs: increasing throughput, decreasing the burden upon the operator, and providing increased safety interlocks. Finally, the CVAP reactor operational costs are less than traditional batch reactors by a factor of 21. Preliminary results from this study indicate promising results for future development of bulk biochar processing.

Keywords: biochar, pyrolysis, modular reactor, design, characterization

Dedication

I would like to dedicate this work to my beloved cat Horatio.

Acknowledgements

I would like to foremost thank my advisor, Dr. Richard LaDouceur, for his inspiration, encouragement, and support. I would also like to acknowledge the assistance from my committee members: Dr. Mario Caccia, Steve Tarrant, and Ryan Munson. Finally, I would like to recognize the hard work and dedication of industry partners, peers and undergraduate research assistants, specifically: Jeffery John, Benjamin Mossman, Kerry O'Leary, Julie Muretta, Ron Hruban, Daniel Goettlich, Mitchell Harvey, Alex George, Zainab Nasrullah, Oluwatosin Adebayo, James Adams, Ben Burkhalter, Alex Schaff, Ethan Heggem, Jason Brown, and Duncan Sterk, without whom this project would not have been completed.

Table of Contents

List of Tables

List of Figures

List of Equations

1. Introduction

1.1. Biochar

Biochar is fundamentally defined as a heterogeneous carbon-rich substance [1]. Biochar

has been produced throughout history, first appearing among the Amazonian people between 450

BC and 950 AD. Due to the relatively low nutrient levels in the rainforest, the Amazonians

would utilize biochar, known as *terra preta*, to both fix carbon and trap nutrients in the soil. The

addition of the biochar would effectively transform degraded soil into rich and stable humus.

The Amazonians would produce this biochar by burning large volumes of buried forest deadfall

and organic waste [2]. This process, utilizing high heat and low oxygen conditions, has since

become known as pyrolysis or carbonization. To date, biochar is still most commonly produced

through the pyrolysis process. Pyrolysis is defined as the thermal decomposition of a substance

within a chemically inert atmosphere [3]. The purpose of pyrolysis is to retain desired

constituents while driving off volatile elements, transforming the bulk, surface, and structural

characteristics of the material. During biochar production, water, alcohol, and organic molecules

are driven from the biomass, leaving a porous, carbon-rich adsorbent behind [4]. The resulting

porosity and surface chemistry of the biochar heavily influence the adsorption selectivity and

capacity. Biochar performance characteristics are optimized by adjusting pyrolysis parameters,

such as temperature and heating rate, in addition to varying the organic feedstock and chemically

activating the surface [5]. Precise control of these parameters allows for the production of lab-

scale biochar, but large-scale production requires further study to determine economic feasibility.

1.2.   Modular Reactors

Process engineering is critical to material and commodity manufacturing globally. To accommodate the recent emphasis placed upon industry to facilitate decarbonization, the historic principles involved in process design must be reevaluated. In the 2022 New Directions for Chemical Engineering Report, the National Academies of Science, Engineering, and Medicine emphasize the need for flexible manufacturing practices, including scaled-down and scaled-out processes [6]. Flexible manufacturing processes place a premium upon efficient, environmentally-conscious, and economical production to develop a circular economy. Circular economies are designed to reduce pollution by utilizing waste products, extending the design life of products, and integrating sustainable feedstocks. In addition to the alteration of product and feedstock characteristics, processing facilities must also be redesigned for flexible manufacturing. Instead of a few, large processing and refining facilities, the National Academy of Engineering urges the development of many, modular facilities. By creating these modular facilities, the production can be taken directly to the feedstock, vastly decreasing the carbon footprint associated with transportation by truck, rail, or pipeline [6]. Additionally, these modular facilities can be easily modified or expanded upon to accommodate a variety of feedstocks, and are thus easily tunable by application. Biochar production is an excellent process with which to test flexible manufacturing and circular economic principles. Biochar can be produced from a variety of sustainable feedstocks in portable reactors; additionally, byproducts of pyrolysis (syngas and bio-oils) can be refined into substitutes for petroleum products [7]. To date, questions linger regarding the scalability of high-grade biochar production [1].

2. Background

2.1. Biochar Production Methods

Due to the increasing interest in the utilization of biochar for environmental remediation, several mechanisms of production have been developed [1]. On a fundamental level, each method produces biochar by thermochemical conversion through thermal decomposition in an oxygen-limited environment. The decision to utilize a particular technology often results from the type of biomass feedstock provided and the desired product characteristics. The main industrially-practiced biochar production methods are: torrefaction, gasification, hydrothermal carbonization, and pyrolysis, which will be presented in detail below [8].

2.1.1. Torrefaction

The torrefaction of biomass is commonly utilized to increase the heating values of biomass-based fuels [9]. During the torrefaction process (Fig. 1), biomass is heated to temperatures between 250-320°C (482-608°F) in the absence of oxygen.
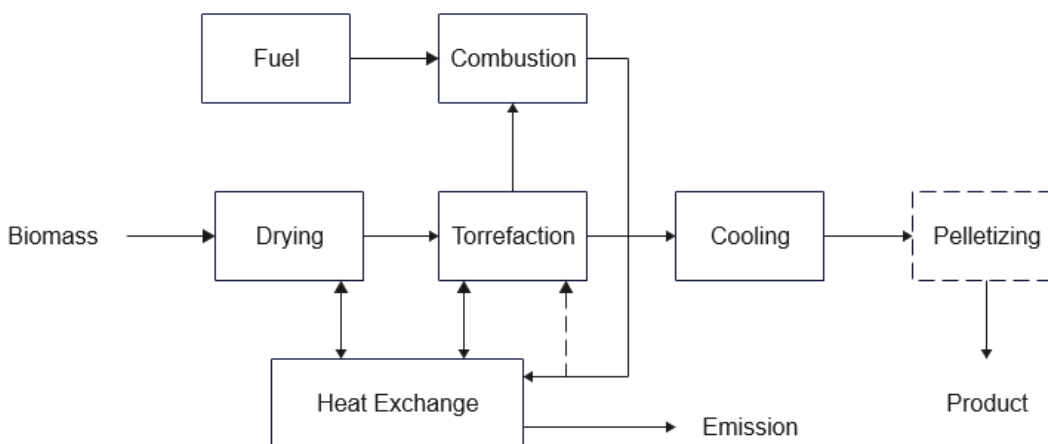
Figure 1: Closed-loop torrefaction process diagram including preparation, reheating, and post-processing operations to produce biochar pellets with an increased energy density. Figure adapted from [9].

As a result, a partial amount of the volatile matter (approximately 20%) in the biomass is removed in the form of a process synthesis gas (syngas) [9]. In torrefaction, syngas is known as torgas and is often combusted to power the torrefaction reactor. Due to the removal of volatile matter, the characteristics of the produced biochar are altered. Fiber structures present in the biomass are converted to lesser cellulose molecules, causing the material to become brittle. In addition, the biomass becomes hydrophilic after torrefaction. Most importantly however, the heating value of the product gradually increases with process temperature and soak time. With most woods, torrefaction can increase the heating value from 19 MJ/kg (8,169 BTU/lb) up to 30 MJ/kg (12,898 BTU/lb) [9]. The increase in the heating value stems from the volatilization of surface and bonded waters, which absorb heat before increasing the bulk temperature when present. The heating value of a material represents the amount of heat generated per unit mass during an ideal combustion reaction. Increasing the heating value is significant when the combustion of a material is utilized for heating. An increase in the heating value allows for more product (heat) to be produced from a fixed quantity of input material. Despite the added benefit with respect to the heating value, torrefaction is not considered a suitable method for producing biochar for remediation applications. As stated previously, roughly 20% of the starting mass is volatilized during torrefaction due to the moderately low temperatures. Over these temperatures, water is driven from the biomass, but many additional volatile molecules remain [8]. The existence of these molecules prevents the surface of the biochar from being morphologically conducive to high-adsorption capacity.

2.1.2. Gasification

The gasification of biomass is commonly utilized when syngas production is prioritized. Gasification is fundamentally defined as the thermochemical conversion of a carbon-rich solid

into a gas in the presence of a gasifying agent [10]. During the gasification process (Fig. 2), biomass is heated to temperatures between 700-1000°C (1292-1832°F) in diminished oxygen to produce syngas and heat [11]. Next, the syngas can be conditioned with reducing agents to effectively refine the gas. Finally, the conditioned gas is either collected or combusted to produce electricity.
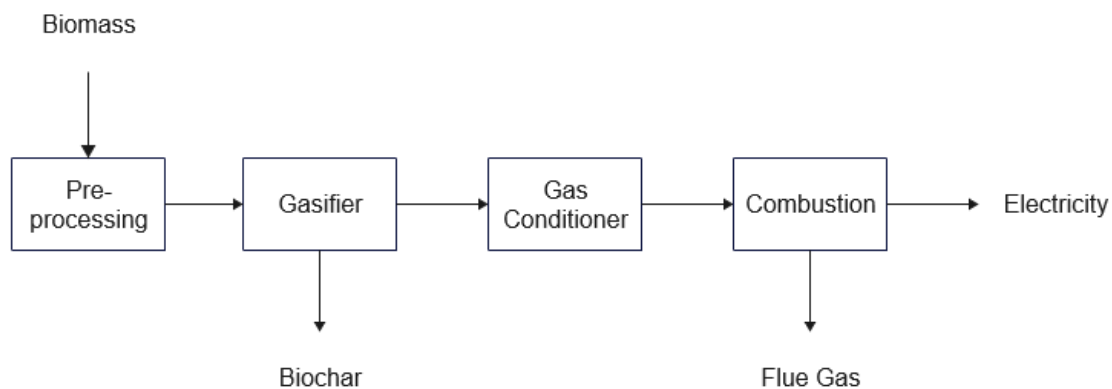
Figure 2: Gasification process diagram including post-processing operations to generate biochar and electricity. Figure adapted from [11].

Gasification reactors are commonly configured as fixed beds, fluidized beds, or entrained flow. Fixed bed reactors are simple to design, but usually produce small batches and suffer from non-uniform heating issues. Fluidized bed reactors are much more complex, but provide uniform heating and improved solid-gas contact. Entrained flow reactors employ temperatures upwards of 1500°C (2732°F) to produce batches on a tonnage basis, and thus consume increased amounts of gas and power during operation [11]. The gasification process can be operated with a variety of atmospheres including oxygen, steam, carbon dioxide, supercritical water, or most commonly, air [12]. The atmosphere serves as an oxidizing agent during the reaction and, when combined with the syngas, causes an increase in the heating value of the syngas. Steam, carbon

dioxide, oxygen and supercritical water result in larger heating value increases, but air gasification is most common industrially due to its reduced operating cost. Generally, the air gasification process is operated as an endothermic reaction, and the air content may be adjusted to hold a specific gasification temperature. There are three products from the gasification reaction: biochar, syngas, and flue gas. Due to the process temperatures exceeding 700°C (1292°F), approximately 90% of the starting mass is lost to form process syngas [11]. This syngas, comprising of chiefly diatomic hydrogen, methane, and carbon monoxide is produced in large quantities during gasification and is considered the desired reaction product. Once the syngas has been treated, it is commonly combusted to produce electrical power and flue gas is exhausted to the environment. While syngas is produced in large quantities during gasification, the process yields small amounts of biochar. Consequently, if biochar is the desired reaction product, operators do not commonly choose to perform gasification.

2.1.3. Hydrothermal Carbonization

The hydrothermal carbonization (HTC) process is commonly utilized to produce biochar from moist biomass feedstocks, independent of energy input. In most carbonization processes, the energetic efficiency of the process is greatly increased with the addition of a pre-drying step. Hydrothermal carbonization (Fig. 3) utilizes biomass with moisture contents ranging from 75% to 90% under hot compressed water to produce hydrochar via thermochemical conversion [13]. During HTC, the hydrochar is the desired byproduct, but large amounts of acidic process water and carbon dioxide are produced as well. While HTC requires minimal feedstock preparation, the products require additional post-processing steps compared to other carbonization methods.
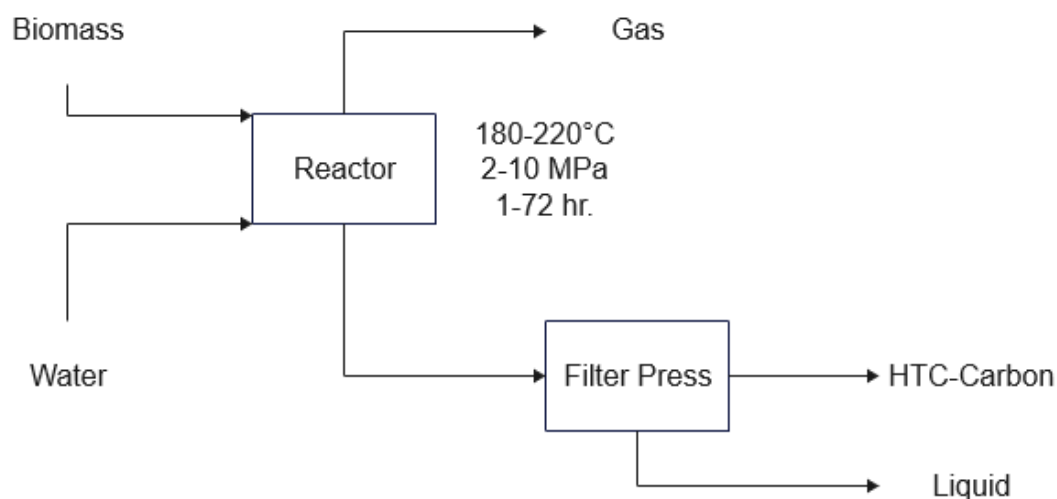
Figure 3: Hydrothermal carbonization process diagram depicting post-processing operations to generate hydrochar and CO_2-rich syngas. Figure adapted from [13].

Due to extensive post-processing steps, HTC is a more complex process than other carbonization methods. Operators can justify the complexity by designing systems to be environmentally-friendly and inexpensive. HTC occurs at low temperatures for carbonization, 180-220°C (356-428°F), decreasing the energy costs associated with operation [14]. In addition, HTC operation results in low emission levels from the dissolution of produced nitrogen oxides and sulfur oxides being retained in the process water. A simple HTC reactor utilizes a batch autoclave that is capable of supporting subcritical water and self-pressurization. Optimal HTC feedstock materials include algae and other marine biomass, where the water present acts as both a solvent and reaction medium. During HTC, subcritical water is pumped into the reactor to inexpensively increase the amount of reaction medium. Heat and pressure from the water weakens the hydrogen bonds in the biomass, shifting the dielectric constant, and catalyzing the reaction. Inside the reactor, hydrolysis, dehydration, decarboxylation, aromatization, and re-condensation occur simultaneously to produce hydrochar, and small amounts of carbon dioxide

[15]. While the evolved gas is collected from the reactor, the resulting hydrochar/process water slurry must undergo extensive post-processing. Typical steps involve solid-liquid separation in a dewatering unit and extensive drying operations for the hydrochar. After separation, the process water can be further reacted and distilled to produce bio-oils and solvents suitable to replace commercially available hydrocarbons [14]. Due to the complexity of the post-processing procedures, operators must be able to market both solid and liquid byproducts to make HTC economically viable.

2.1.4. Pyrolysis

The pyrolysis process is utilized to thermochemically convert biomass into a variety of renewable carbon-based products. Pyrolysis is the oldest and most industrially prevalent biochar production technology. Pyrolysis is fundamentally defined as high-temperature decomposition of a substance within a chemically inert atmosphere [3]. The process can accept a variety of feedstock materials, with lignocellulosic biomass being the most common. To date, lignocellulosic biomass is the largest source of renewable carbon on the planet [16]. To achieve optimal thermal distributions throughout the biomass and optimize reaction thermodynamics and kinetics, the feedstock is often dried and reduced in size to chips or powder. Due to the complexity of the biomass, temperatures of at minimum 300°C (572°F) must be achieved to deconstruct the strong bio-polymers present in lignocellulosic biomass. The absence of oxygen in the process prevents combustion from occurring (which would normally turn the biomass into ash), forming biochar [16]. During the bio-polymer deconstruction, the volatile molecules in the biomass are evolved to form a combustible gas. Of the combustible gases produced, most can be readily condensed at room temperature to produce bio-oil, a combustible liquid that can be further refined to replace petroleum-based fuels. The remainder of the syngas, primarily CO_2,

CO, H₂, and light hydrocarbons, can be combusted in an afterburning reactor to provide additional process heat. By utilizing the reaction products as a fuel source, the pyrolysis process (Fig. 4) can operate on a closed-loop [17].
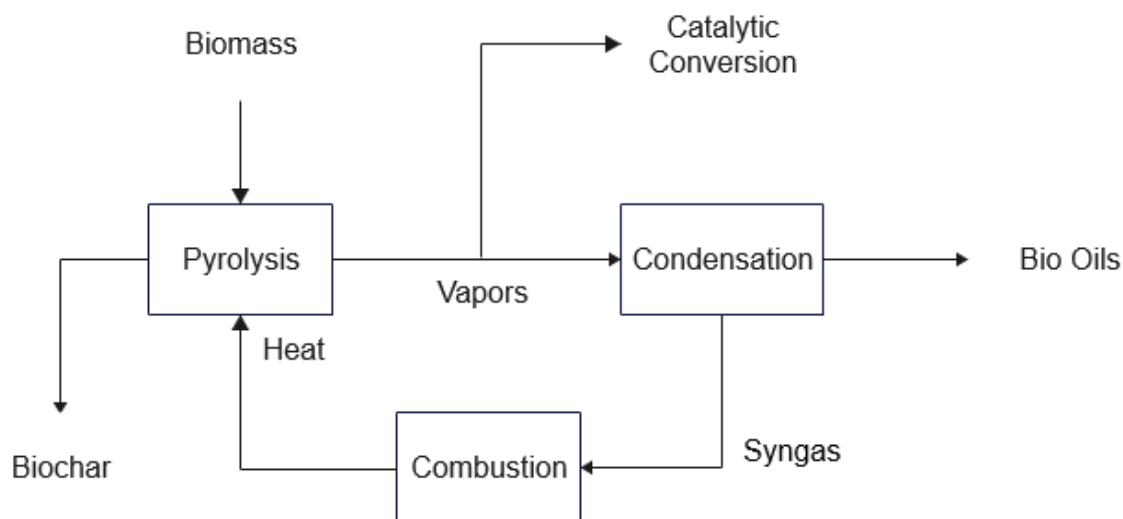
Figure 4: Closed-loop pyrolysis process diagram including post-processing operations to generate useable solid, aqueous, and gaseous products. Figure adapted from [17].

Pyrolysis requires heating in inert conditions to facilitate the desired thermochemical conversion. While pyrolysis is always operated within an oxygen-free environment, the process temperature can range between 300°C (572°F) and 1000°C (1832°F) [17]. A process temperature within this range is required to heat the material above its decomposition temperature to facilitate the destruction of the chemical bonds in the biomass. The pyrolysis process can be operated using three methods: slow, fast, and flash [18]. Slow pyrolysis involves heating rates less than 10°C (50°F) per minute and incentivizes biochar formation. Fast pyrolysis occurs with heating rates between 10°C(50°F)/min and 200°C(392°F)/min and promotes bio-oil production. Flash pyrolysis is utilized to produce solely gaseous products, where fine biomass particles reach the process temperature almost instantaneously. Contrasted

with slow and fast pyrolysis, flash pyrolysis processes must be operated at the maximum of the

pyrolysis range, 1000°C (1832°F). The ideal process temperature is dependent upon the desired

amounts and physicochemical properties of the reaction products (Fig. 5). The influence of

process parameters such as temperature will be discussed in detail in the following section of the

document.
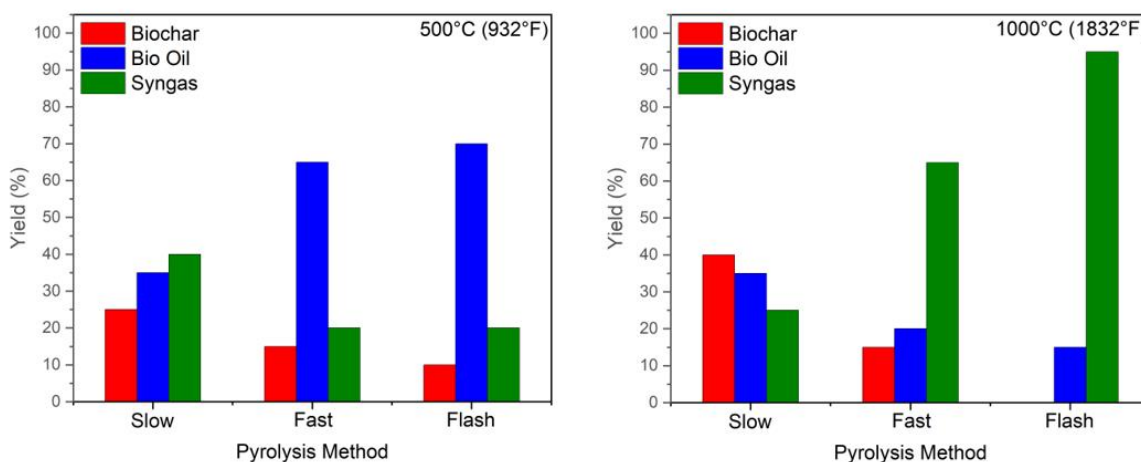
Figure 5: Influence of process temperature and residence time on pyrolysis product yields. Figure adapted from [18].

Pyrolysis is an attractive technology to operators for several reasons. Most significantly,

the infrastructure for most pyrolysis reactors can be readily configured to facilitate a variety of

operational conditions. For example, most heating elements will allow the process to operate at

temperatures ranging from 300°C (572°F) to 1000°C (1832°F). Additionally, the feed rates for

continuous pyrolysis systems can be easily adjusted to adjust both heating rate and residence

time. Consequently, the three aforementioned pyrolysis methods can be performed by a single

pyrolysis reactor by inexpensively altering the operating software. Another benefit to pyrolysis

is the ability to accept a large variety of feedstocks. Virtually any variety of biomass may be

used, and with the exception of flash pyrolysis, minimal drying and size reduction operations are required [19]. By adjusting the biomass feedstock and process parameters, operators can choose to prioritize the formation of specific byproducts. Finally, due to syngas afterburning operations, pyrolysis reactors have minimal health and safety impacts from volatile organic compounds. With the inclusion of a high-temperature combustion reactor (~800°C(~1472°F)), volatile organic compounds produced during pyrolysis are oxidized to form carbon dioxide and water vapor [17]. This post-processing operation ensures that the process is not only clean-burning, but the heat generated from the combustion can be utilized to supplement the pyrolysis reactor, decreasing the usage of fossil fuels or electricity. Furthermore, the bio-oils produced in the process can facilitate a similar function when combusted. With the exception of start-up operations, it is possible to design a pyrolysis reactor to operate without reliance on external electrical or fossil fuel supplies.

2.2. Effects of Process Parameters

Pyrolysis occurs under oxygen-limited conditions between 300°C (572°F) and 1000°C (1832°F) [18]. Furthermore, based on the heating rates and residence times, pyrolysis can be further subclassified into slow pyrolysis, fast pyrolysis, and flash pyrolysis. These process parameters: temperature, residence time, heating rate, and feedstock have a significant impact on the physicochemical properties of the reaction products [20]. The following sections detail the effects of the aforementioned process parameters on biochar properties.

2.2.1. Process Temperature

During the thermochemical conversion of biomass during pyrolysis, the process heat facilitates the deconstruction of the bio-polymers present in the feedstock. The cellulose-based and lignin-based bio-polymers require heat to break their bonding. By breaking these bonds, the

solid molecules can undergo a phase change and become biochar and evolved syngas. Due to the inherent structural complexity of the bio-polymers, large amounts of heat are required to facilitate this phase change. Previous experimentation has been able to draw relationships between thermochemical conversion percentage and process temperature using present yield calculations [21]. These experiments determined that biochar yield decreases and conversion increases as the process temperature increases. This trend is caused chiefly by the thermal degradation of cellulose and lignin structures into volatile compounds. As the temperature is further increased, two processes occur simultaneously; the rate of thermal degradation increases (forming volatiles), and the volatiles are further cracked to form bio-oils and syngas. Assuming that the reaction operates in a closed system and therefore total system mass is held constant, the formation of the bio-oils and syngas will result in a loss of up to 80% of the starting mass. This loss of volatiles is critical for the production of biochar as the fixed carbon content and pH (in water suspension) can increase as much as 200% and 8 logarithmic units, respectively [21]. The fixed carbon and high- pH are two physicochemical properties of biochar that facilitate environmental remediation applications. To summarize, the process temperature plays a vital role in the properties of biochar. As temperature increases, pH increases, product yield decreases, and carbon content increases. Operators can therefore adjust the pyrolysis temperature to generate biochar with specific physiochemical properties.

2.2.2. Residence Time

In addition to the process temperature, the residence time of biomass inside of the pyrolysis reactor has a major effect on the properties of the biochar [20]. While process temperature directly affects the thermochemical conversion of the feedstock, the residence time has more of an indirect affect. The residence time affects the transfer of heat from the process

through the feedstock. The governing principle of heat transfer is that heat always flows from

hot to cold media by three mechanisms: conduction, convection, and radiation [22]. The

majority of pyrolysis reactors utilize a resistive heating element that is external to the process

[17]. The element heats the reaction vessel via convection, which effectively transfers the heat

to the atmosphere inside the reactor via conduction. While these mechanisms of heat transfer are

of note when attempting to minimize process heat losses, they have little impact on the biochar

itself. The crucial heat transfer steps involve the convective heat transfer from the atmosphere to

the biomass particles and the conductive heat transfer between adjoining particles. In fixed-bed

reactors, the conductive heat transfer is especially crucial. As opposed to agitated or fluidized-

bed reactors, a majority of the particles are not in contact with the atmosphere. Because of this,

heat is not able to be convectively transferred from the heated gas. In all methods of heat

transfer, the rate of energy input is directly proportional to the resulting increase in temperature

of the material [22]. Operating under the assumption that the energy input is held at a constant

rate, the material will require a longer amount of time to undergo a larger increase in

temperature. Furthermore, increased distances between biomass particles and the heated

atmosphere will require longer residence times to reach the process temperature. As discussed in

the previous section, reaching the process temperature is crucial to producing biochar with the

desired properties.

Empirical data further serves to determine the quantifiable effects of residence time

during biochar production (Fig. 6). This data was collected from a fixed-bed pyrolysis reactor.
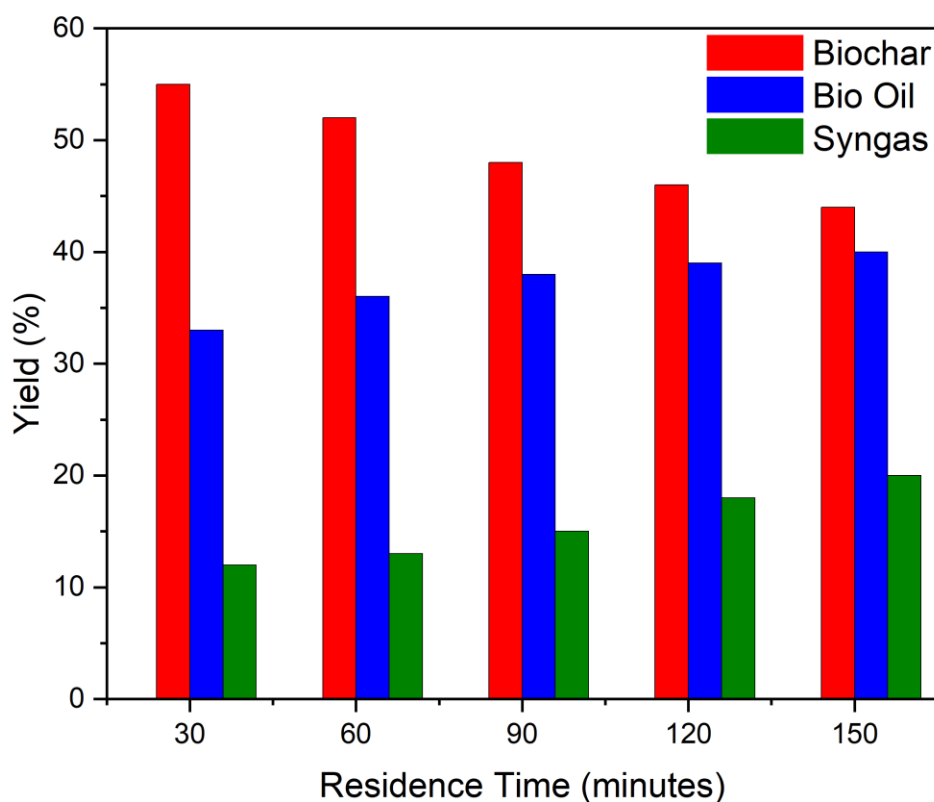
Figure 6: Histogram depicting the changes in pyrolysis product yields with increasing residence time. Figure adapted from [23].

The percent yield of biochar decreases as the residence time increases, due to increasing amounts of biomass reaching the process temperature and increasing the conversion to biochar. Further evidence of this occurrence is the simultaneous increase in yield of the volatile products, tar and biogas. Additionally, the biochar yield decrease between 120 min and 150 min is substantially smaller, indicating that the process temperature has been reached by the entirety of the sample at that time [23]. In operation, increases in residence times produce biochar with consistent properties, but energy costs may increase for fixed-bed reactors. These costs and the residence time can both be decreased by agitating, rotating, or fluidizing the sample bed. These

processes mix not only the biomass, but the process heat as well. Furthermore, more of the biomass will come into direct contact with heated atmosphere. To summarize, the residence time does not affect the properties of biochar as significantly as process temperature, but does affect the distribution of heat through the biomass.

2.2.3. Heating Rate

The process heating rate is a fundamental parameter that defines the pyrolysis method: slow, fast, or flash. For a batch process, the heating rate is controlled, and often limited, by the process heating element. In continuous processes, the heating rate is governed by both the resulting thermal gradient due to the process temperature and the material feed rate [20]. Typically, faster heating rates cause lateral shifts in the pyrolysis temperature, causing volatilization to appear to occur at higher temperatures [24]. The apparent increase in temperature results from the poor heat transfer through the biomass, which causes the bulk temperature to lag that of the process. Increased heating rates also increase the rate of thermal degradation as many compounds are volatilized simultaneously [25]. This simultaneous volatilization often causes fragmentation of the biomass and pore structures, resulting in smaller particle sizes and decreased microporosity. At lower heating rates, gases slowly escape the solid biomass in small quantities, leaving small pores behind. As the heating rate increases, the quantity of escaping gases also increases, creating larger pores. At extreme heating rates upwards of 50°C/min. (122°F/min.), the rate of volatilization causes a violent release of gases that cause the biomass to fracture [24]. Fracturing occurs when large amounts of gas are released simultaneously, resulting in the linking of pores to form channels. These channels converge to form cracks, weakening the structure, and may facilitate a size reduction. Overall, the biochar pore sizes increase with heating rate until fracturing occurs and porosity becomes

nonexistent [24]. To best enhance both biochar yield and microporous morphologies for remediation applications, heating rates in the range of 10°C/min-15°C/min (50°F/min-60°F/min) are required [25]. Bio-oil production is also increased up to 8% with the heating rates, while syngas production decreases due to the inability to generate secondary cracking reactions [24]. Operators are ultimately able to adjust the process heating rates to generate biochar with the desired pore sizes [20].

2.2.4. Feedstock

To facilitate the production of biochar via pyrolysis, a biomass feedstock must be used. Biomass is a biological, organic, or non-organic material derived from living or deceased organisms [26]. In addition, animal and industrial wastes are also classified as biomass as they can be processed to obtain biochar and energy. Biochar properties are significantly affected by the physicochemical properties of the biomass feedstock [27]. The moisture content of the biomass has a direct correlation to both the structure of the biochar in addition to the operating costs of the process. Low moisture in the feedstock is advisable due to the reduction of heat energy and residence time required to volatilize the water and produce biochar. Biomass by nature always experiences moisture retention, and pre-drying operations are often utilized to lower the moisture content before pyrolysis. Furthermore, by decreasing the moisture content, the produced biochar surface becomes more polyaromatic and graphite-like due to a longer effective pyrolysis time [27]. Lignin and cellulose content within the biomass impact pyrolysis product yields. High cellulose content favors the formation of tar and bio-oils, while high-lignin content favors the formation of biochar [28]. The difference of behavior during pyrolysis is due to cellulose-based compounds having a lower molecular weight than lignin. The lignin-based compounds are also very resistant to thermal degradation. Thus, increasing the lignin content in

the biomass feedstock will increase the biochar produced during pyrolysis [29]. The amount of lignin and cellulose in the biomass also has an effect on the specific surface area of the biochar. An increase of cellulose, which volatilizes during pyrolysis, increases the surface area of the biochar via the formation of porous channel structures [30]. Additionally, the presence of inorganic molecules in waste-derived feedstocks decreases the specific surface area of the resulting biochar. Consequently, operators are able to utilize feedstock sourcing as a process variable to generate biochar with specific physiochemical properties [27].

2.3.   Biochar Adsorption

Due to the nature of feedstock material and processing, biochar has a unique capacity as an adsorbing agent for a wide variety of contaminants. The adsorption mechanism of biochar to remove pollutants involves electrostatic interaction, ion exchange, pore filling, and precipitation [31]. The capacity, selectivity, and adsorption behavior result from the physicochemical properties of the biochar. The adsorption process (Fig. 7) includes: physical adsorption in which the adsorbate settles on the adsorbent's surface, precipitation and complexation in which the adsorbate deposits on the adsorbent's surface, and pore filling in which the adsorbate is condensed into the pore of the adsorbent [32].
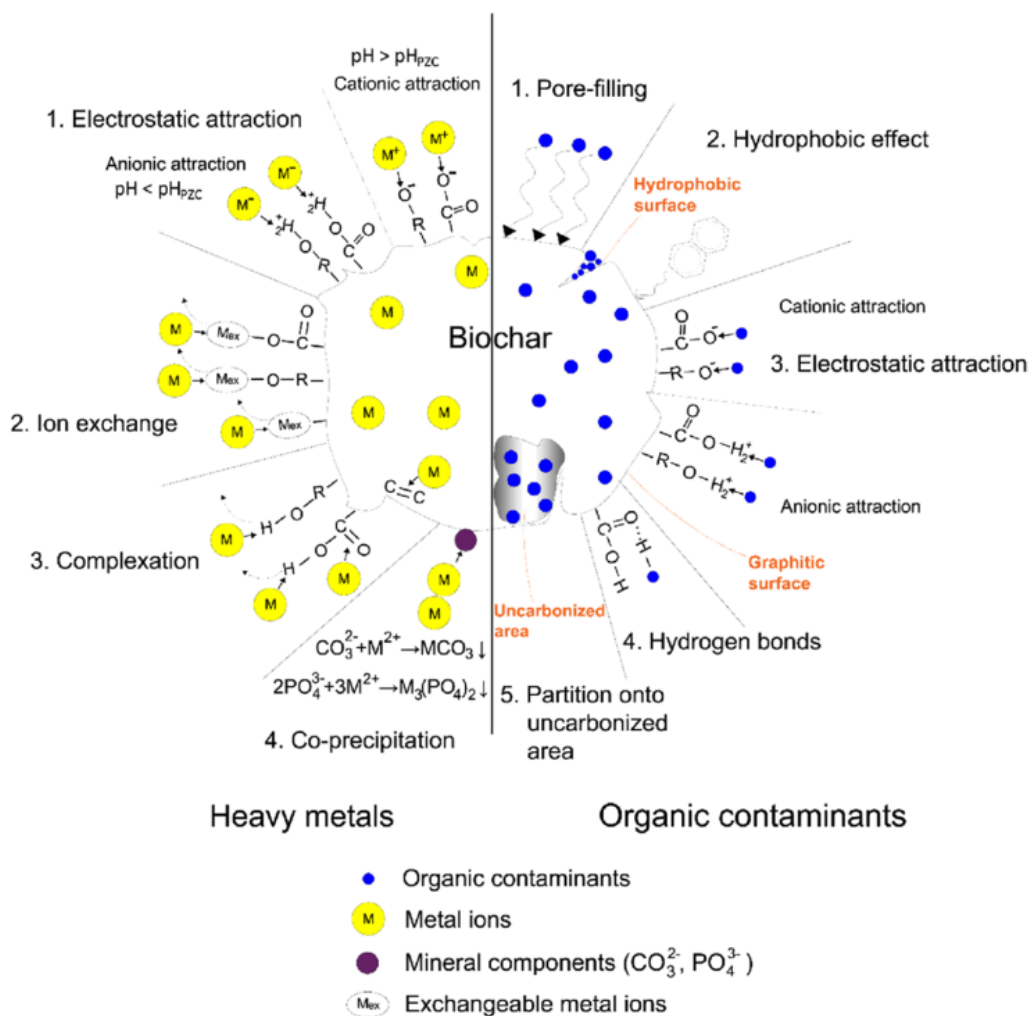
Figure 7: Adsorption mechanisms of biochar for the removal of inorganic (heavy metal) and organic contaminants. Figure as designed by [32].

Biochar exhibits a large variability of physicochemical properties such as high specific surface area and pH. This variability facilitates avenues to maximize the targeted adsorption of environmental pollutants for remediation efforts [33]. Thus, the remainder of the narrative will focus on the adsorption mechanisms for organic and inorganic environmental contaminants.

2.3.1. Inorganic Contaminant Adsorption

The mechanisms involved in the removal of inorganic contaminants (Fig. 7) are surface adsorption, electrostatic interaction, ion exchange, precipitation and complexation [31]. Surface

chemisorption is a process which involves the diffusion of metal ions into the pores of the

biochar, creating chemical bonds. The amount of surface adsorption is dependent upon the pore

volume and surface area of the biochar [34]. High-pyrolysis temperatures (700°C (1292°F))

enhance the surface area and pore volume of the biochar and result in increased surface

adsorption capacity. The selectivity of the biochar also influences the surface adsorption.

Metals exhibit different valence shells, which influence their affinities to surface adsorption [35].

Electrostatic interaction between charged metal ions and the biochar serves to limit the

mobilization of metals in solution [31]. The electrostatic interaction is facilitated by the presence

of negatively charged biochar in solution with positively charged metal ions. This attraction can

be increased by producing biochar at temperatures greater than 400°C (752°F) [36]. Ion

exchange involves the exchange of protons and cations from the metal with the dissolved salts on

the surface of the biochar [31]. The adsorption capacity is governed by the size of contaminant

and surface functional groups on the biochar [37]. By increasing the ion exchange capacity,

metal adsorption is also increased. The capacity for ion exchange begins to decrease as pyrolysis

temperatures increase upwards of 350°C (662°F) [38]. Biochar selectivity also affects the

capacity of ion exchange [39]. Precipitation is one of the most significant steps in the removal of

inorganic contaminants, involving the formation of mineral precipitates on the alkaline surface of

the biochar [31]. Alkalinity of biochar is caused by the thermal degradation of cellulose and

hemicellulose during pyrolysis. It has been observed that the alkalinity, and thus precipitation

efficiency, increases with pyrolysis temperature upwards of 300°C (572°F) [40]. The final

mechanism of inorganic adsorption is metal complexation, which involves the interaction of

specific metal ligands to form a complex on the biochar surface [31]. Biochar produced at

temperatures below 450°C (842°F) contain oxygen-bearing surface functional groups such as

phenolic, lactonic and carboxyl. This oxygen content increases the surface oxidation of the biochar, enhancing the metal complexation [41]. Plant-derived biochar has been shown overall to have increased surface complexation capacities compared to waste-derived biochar [42]. Operators with an understanding of the aforementioned adsorption mechanisms are able to adjust process parameters to produce biochar with the optimal selectivity for inorganic species.

2.3.2. Organic Contaminant Adsorption

The mechanisms involved in the removal of organic contaminants (Fig. 7) are partitioning, pore filling, electrostatic interaction, electron donor–acceptor interaction, and hydrophobic interaction [31]. Partitioning involves the diffusion of organic material into the non-carbonized portion of the biochar. The non-carbonized portion, consisting of crystalline or amorphous carbon, readily interacts with organic molecules, facilitating adsorption [42]. The capacity of partitioning is dependent upon the ratio between the carbonized and non-carbonized portions in the biochar. Pyrolysis temperatures between 200°C (392°F) and 350°C (662°F) produce biochar with optimal organic carbon fractions and thus, the highest capacity for partitioning [43]. Generally, the partitioning mechanism is most efficient when the biochar has a high-content of volatile matter [44]. Pore filling occurs in the mesopores (2–50 nm) and micropores (< 2 nm) of biochar. Pore filling is a physical adsorption process, so efficiency depends upon the polarities of the biochar and contaminant as well as the size of the contaminant [31]. Additionally, slow pyrolysis with temperatures above 700°C (1292°F) are recommended to produce biochar with the desired pore sizes and small amount of volatile matter required to facilitate efficient pore filling [45]. Electrostatic interaction is the main mechanism of adsorption for ionizable organic compounds, such as organic acids and bases, onto the positively charged surface of the biochar [31]. Its efficiency to attract or to repel pollutants depends upon the pH

and ionic strength of the aqueous solution [43]. The biochar surface exhibits positive charge at low pH and negative charge at high pH. Thus, the surface charge of the biochar is governed by the pH of the solution. Ionic strength of the solution also affects the ability of the contaminants and biochar to interact. As ionic strength increases, contaminants become more attracted to the other molecules in solution and decrease the adsorptive ability of the biochar [46]. Electron donor–acceptor interaction is applied to the adsorption of aromatic compounds onto graphene-like biochar [31]. This mechanism is facilitated by the ability of the biochar to donate or accept a π-electron to induce adsorption. While complete graphitization of biochar only occurs with residence times approaching the infinite, the process begins with pyrolysis temperatures greater than 1100°C (2012°F) [47]. However, the donor/acceptor behavior of the biochar π-electron is a function of a much lower pyrolysis temperature. Process temperatures above 500°C (932°F) yield biochar with electron donating behavior, while temperatures below yield biochar with electron accepting behavior [48]. If the electron donor/acceptor behavior of the biochar is equal and opposite to that of the organic contaminant, then adsorption will occur. The final mechanism of organic adsorption is hydrophobic interaction, which is commonly utilized for the removal of hydrophobic and neutral contaminants using graphene-structured biochar [31]. This mechanism requires less energy than partitioning, and is therefore more favorable. Adsorptive behavior of hydrophobic interaction is facilitated by the decrease of polar groups on the surface of the biochar due to the pyrolysis temperature [49]. Generally increasing the pyrolysis temperature above 700°C (1292°F) decreases the number of polar groups and increases the surface carbon concentration, increasing the adsorptive capacity of hydrophobic interaction [31]. Operators with an understanding of the aforementioned adsorption mechanisms are able to adjust process parameters to produce biochar with the optimal selectivity for organic species.

2.4. Batch Pyrolysis Reactor

Previous research at Montana Technological University has resulted in the production of a batch pyrolysis reactor. This prototype reactor (Fig. 8) is the culmination of two senior capstone projects, focusing on reactor design and automation, respectively. Reactor development was undertaken with the objective of producing biochar under tightly controlled operating conditions. Furthermore, sensing capabilities were integrated to facilitate a more detailed understanding of the pyrolysis process. Finally, the performance of this reactor was analyzed to assist in the development of future pyrolysis reactors at Montana Technological University.
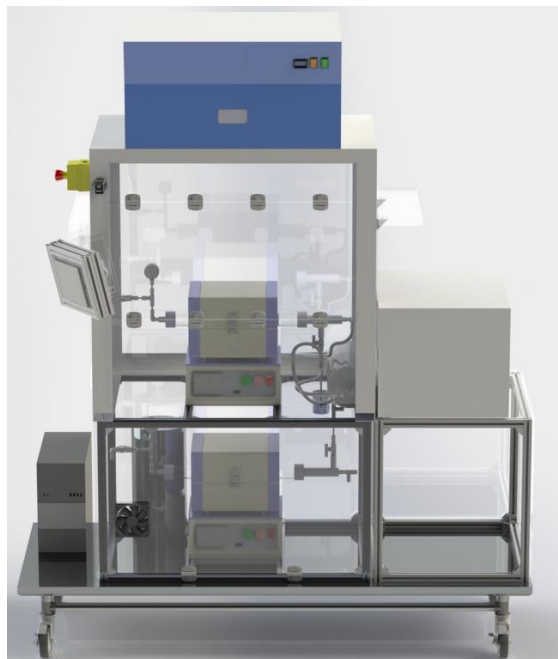
Figure 8: 3-D Model (SolidWorks® 2022) of the Montana Tech pyrolysis reactor featuring the fixed-bed pyrolysis furnace (top), syngas afterburner (bottom), and gas chromatograph (right).

This system performs three major operations: pyrolysis, syngas afterburning, and syngas analysis. Pyrolysis takes place in an inert gas purged, fixed-bed tube furnace. Compressed

argon gas (99.998% purity) provides a constant purge flow during operation to facilitate the nonreactive atmosphere required for pyrolysis. The pyrolysis syngas, with the inert gas acting as a carrier, is forced into a condenser where a majority of the condensable bio-oils are then trapped. The remaining syngas mixes with a stream of compressed air and is combusted in an afterburning furnace to prevent volatile organic compounds from being released into the atmosphere. Syngas analysis from an Agilent Gas Chromatograph is conducted in-situ with the pyrolysis reactor. The gas chromatograph detects quantitative amounts of hydrogen, methane, carbon monoxide, carbon dioxide, ethylene, ethane, propane, and propylene to the nearest 0.01% present in the syngas at a single point in time during the process. Quantitative analysis of process syngas allows future researchers to determine the feasibility of the addition of post-processing operations.

The batch pyrolysis reactor employs numerous sensing and automation features to facilitate system usability and process control. Both the pyrolysis and afterburning furnaces are split tube furnaces from MTI corporation. These furnaces feature programmable temperature and time-step setpoints, allowing for complex heating profiles up to 1000°C (1832°F). Additionally, the furnace control is able to hold the process temperature within 1°C (1.8°F) and apply heating rates up to 10°C/min (50°F/min). K-type thermocouples embedded into the process tube provide four points of measurement across the heating zone. The temperature across the heating zone is within +- 1% during operation. The inert gas flowrate is also regulated to +-1% of the setpoint using Aalborg mass flow controllers. This system is also equipped with a number of safety features. Relief valves are integrated into several areas to prevent over-pressurization and the entire reactor is enclosed within a polycarbonate fume hood in the event of a rupture. Atmospheric sensors, calibrated to detect combustible gasses, carbon monoxide and

nitrogen oxides are also present to alert operators of a release of toxins. Finally, an emergency stop button is included to protect both the operator and system infrastructure. All of the sensing and safety equipment is connected to an Allen-Bradley Micro850 Programmable Logic Controller (PLC). In addition to collecting and displaying process data in real-time, the PLC facilitates the automation of the process. Process automation not only decreases the workload on the operator, but also ensures that the system is operated correctly and protects the system from operator error.

Overall, the batch pyrolysis reactor performs satisfactorily. The system is able to uniformly produce biochar over the entire range of pyrolysis conditions. The throughput of the system is approximately 12g (0.42oz) per day, and consumes approximately 2000L (70cf) of argon gas, depending upon the process conditions. All of the system components are connected to a single 20A/120V circuit, resulting in a maximum power consumption of 19.2 kWh per day. Weekly preventative maintenance is also required for the system to ensure that bio-oil residues do not obstruct the plumbing. This system does exhibit numerous drawbacks, namely the small batch sizes. Assuming 24-hour operation, this system would require 28 days to produce 1kg (2.2lb) of biochar. Additionally, the process requires a substantial amount of consumable argon gas, which is not recycled. The configuration of the system also necessitates extensive cleaning operations. Ultimately, the increasing demand of biochar at Montana Technological University is rendering this reactor obsolete, but the design of this system provides a foundation for future pyrolysis reactor designs.

2.5. Continuous Pyrolysis Reactors

Continuous pyrolysis reactors are currently utilized in commercial sectors due to the increased product yields required to make biochar production economically feasible. Production

is only feasible for medium to large-scale biochar production due to the increased process complexity and cost, but provides an increased flexibility with regards to the biomass feedstock. Due to the long-term nature of their operations, these systems employ vacuum rather than a purge gas to generate the inert atmosphere required for pyrolysis. Current industrially practiced pyrolysis methods are classified as: drum-type pyrolizers, rotary kilns, and screw-type pyrolizers [50].

2.5.1. Drum-Type Pyrolizers

Drum-type pyrolizers (Fig. 9) utilize an internally or externally heated drum, mounted horizontally, to facilitate the process heating and material transport during pyrolysis [50].
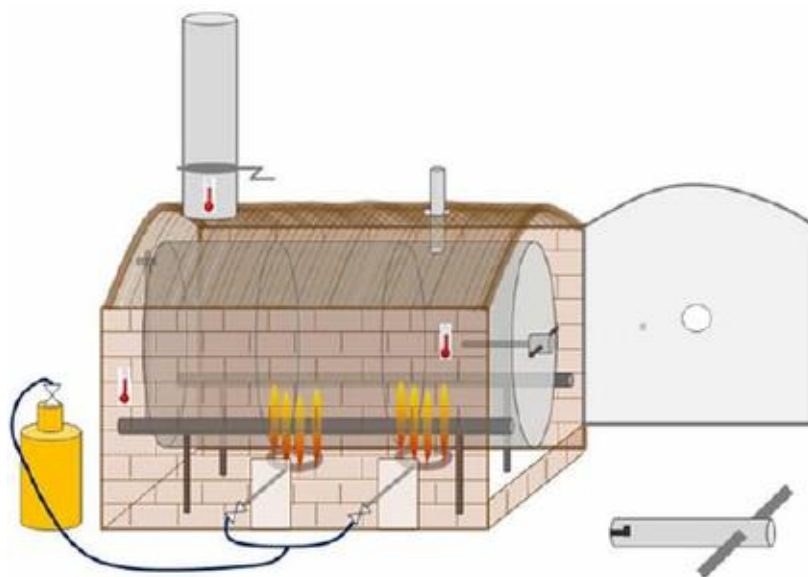
Figure 9: Drum-type pyrolizer schematic depicting an externally heated drum built inside of a refractory kiln to mitigate process heat loss. Figure as designed by [50].

On the interior of the drum are spiraled shelves that facilitate the lateral movement of material without the inclination of the process intake. The rotational speed of the drum is controlled to achieve a specified residence time for the biomass. Rotation of the drum also

serves to agitate and mix the biomass, creating uniform heating conditions. Process heating is facilitated by either externally heating or the placement of resistively heated rods in the interior of the drum [51]. Both methods of heating create operational compromises. External heating of the drum, especially for large processes is inefficient, as the heat must be conducted through the walls of the vessel. Additionally, the external heating elements experience convective losses from the atmosphere between the element and the drum. By constructing drum-type pyrolizers into refractory ovens, the heating efficiency can increase from 50% to 90% [52]. While internal heating mitigates process heat loss, the elements must be placed inside of the corrosive atmosphere of the process. The syngas produced during pyrolysis contains volatile organic compounds, which readily corrode the metal heating elements at temperatures above 450°C (842°F) [50]. Corrosive conditions require frequent inspection and replacement of the heating elements, resulting in process downtime. Due to their simplicity, drum-style pyrolizers are very economical to contract, but the existence and/or mitigation of heating losses result in increased operating costs [50].

2.5.2. Rotary Kilns

Rotary kilns (Fig. 10) utilize an externally heated drum, mounted at an incline, to facilitate the process heating and material transport during pyrolysis [50].
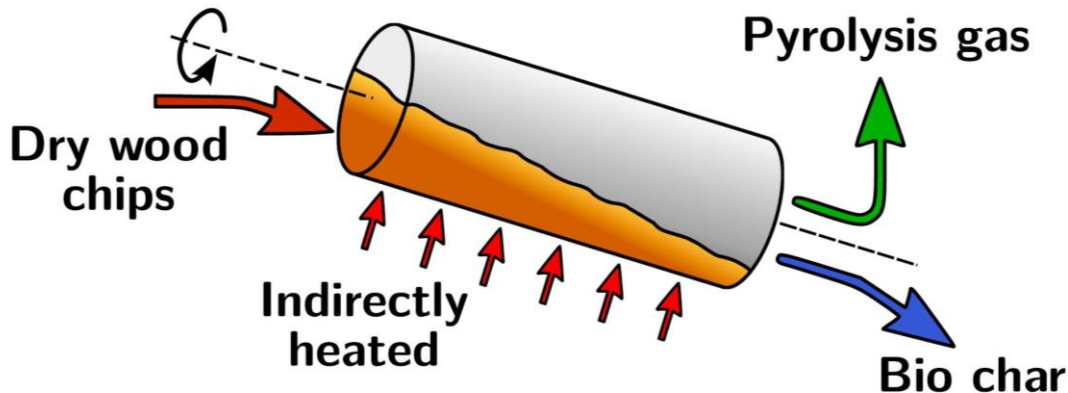
Figure 10: Rotary Kiln pyrolizer schematic depicting an externally heated inclined drum used to heat and move biomass through the process. Figure as designed by [53].

Rotary kilns operate in much the same manner as drum-type pyrolizers, with the exception that the drum is set on an incline. This inclination, combined with the rotation of the drum, facilitates the movement of material through the process [53]. A significant advantage to this design in the decreased energetics requires to transport the material. As the drum rotates and agitates the feedstock, gravity causes it to fall toward the outlet at a uniform rate [54]. Operators are able to utilize the material characteristics such as particle size, shape, and moisture content to specify the required angle of inclination and rotation speed to facilitate the desired residence time [55]. The significant drawback to this design feature is that the process becomes heavily feedstock driven, and even slight alterations to the feedstock preparation operations can impact the rate of feed through the reactor.

2.5.3. Screw-Type Pyrolizers

Screw-type pyrolizers (Fig. 11) utilize one or more internally or externally heated screw augers, mounted horizontally, to facilitate the process heating and material transport during pyrolysis [50].
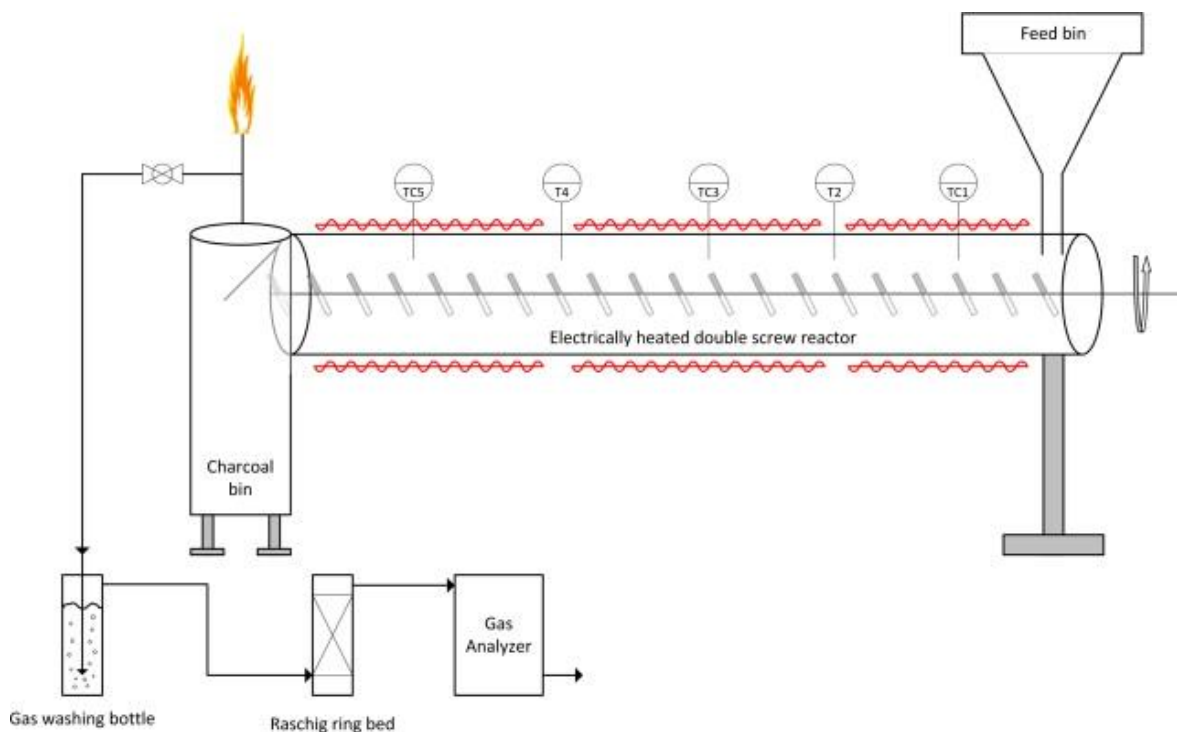
Figure 11: Screw-type pyrolizer schematic depicting two externally heated screw augers to facilitate material transport through the process. Figure as designed by [56].

Screw-type pyrolizers utilize one or several screw augers to move the material through the heating zone. Most materials are able to be fed with a single screw, but non-free flowing materials, such as moist powders, require two or more [57]. The spiraled blades of the screw facilitate the lateral movement of material without the inclination of the process intake. Screws also mix and agitate the feedstock to provide uniform heating during the process. Pitch of the screw blades may also be altered to maximize the movement of varying sizes and viscosities of feedstock. Rotational speed of the screw is controlled to achieve a specified residence time for the biomass. The clearance between the screw and the reactor wall is specified to facilitate efficient movement of the biomass, while simultaneously allowing enough bypass to prevent the binding of the screw [58]. Due to the relative size of screw augers compared to drums, these reactors require significantly less power to transport material. As with the drum-type pyrolizers,

these reactors can be either internally or externally heated. External heating of the process, especially for large systems is inefficient, as the heat must be conducted through the walls of the vessel. To avoid convective losses, electrical heating elements are placed in contact with the reactor walls [56]. Additionally, these reactors are insulated to retain the heat within the process. While internal heating mitigates process heat loss, the elements must be placed inside of the corrosive atmosphere of the process. To facilitate internal heating, the metal screw auger is connected to a power supply [59]. The electrical resistance increases along with the screw size, making uniform heating difficult. Furthermore, prolonged heating of most of the electrically conductive metals at the upper range of pyrolysis (1000°C (1832°F)), causes either melting or deformation. Mitigation of this requires the use of engineered metal alloys, which greatly increase the cost of the system. Overall, screw-type pyrolizers are the most common continuous reactor type, as they offer precise control of process conditions and are able to scale in size easily [50].

3. Research Objectives

Machine design, material selection, and usability principles were utilized to develop the novel Continuous Vacuum-Assisted Pyrolysis (CVAP) reactor. Additionally, chemical and morphological analyses were completed on products from the existing batch reactor to provide a baseline for future comparison. The results from the aforementioned work were used to complete the project and satisfy the following objectives:

- Increase the rate of lab-scale biochar production.

- Eliminate reliance on process consumables to facilitate semi-batch production.

- Facilitate biochar production over the entire range of pyrolysis temperatures.

- Develop a production method suitable for economical mobile delivery.

- Perform a characterization of reactor products to determine feasibility of large-scale production.

4. Methods and Materials

4.1. Reactor Design

The first step in the development of the continuous biochar reactor was to determine the method of biochar production: torrefaction, gasification, hydrothermal carbonization, or pyrolysis. While torrefaction generates large solid product yields (80%), the process is operated at temperatures between 250°C (482°F) and 320°C (608°F). These lower temperatures inhibit the volatilization of a significant number of molecules, leaving the surface of the biochar unaltered with respect to the original feedstock. Surface characteristics resembling the starting biomass are not conducive to the adsorption of organic and inorganic contaminants. The gasification process generates approximately a 10% yield of biochar, with the targeted product being combustible syngas. Additionally, the high process temperatures (>1000°C (>1832°F)) facilitate a complete breakdown of the biochar porosity and surface characteristics that drive adsorption. Hydrothermal carbonization operates in an aqueous atmosphere and is designed for moisture-rich feedstocks. The biomass sources utilized by researchers at Montana Technological University currently undergo pre-processing operations that include drying. Furthermore, the generated biochar is required to be dried and degassed for experimentation. Extensive post-processing separation and drying operations are not economically feasible to develop given the natures of the feedstock and desired product. Given the significant drawbacks to these technologies, the pyrolysis process was determined to be the optimal method for biochar production. Pyrolysis requires comminution and drying pre-processing operations, but requires no post-processing. Thus, pyrolysis systems can be designed with a small footprint, ideal for mobile delivery. In addition, vacuum pyrolysis systems eliminate reliance on process

consumables, a stipulation placed upon this system. Finally, these reactors can operate under a variety of temperature conditions to incentivize the formation of solid, liquid, or gas production.

The next determination necessary for development was the classification of the continuous reactor: rotary kiln, drum-type, or screw-type. Rotary kilns and drum-type pyrolizers require empty volume, called free board, of approximately 80% to facilitate the movement of material. This requirement necessitates the construction of large drums. Large drums result in large surface areas, and therefore increased heat lost to the environment. Heat loss in these reactors can be mitigated by extensive insulation structures, which are both costly and employ large footprints. Operation of both rotary kilns and drum-type pyrolizers without insulation is much too inefficient to be economical, but the addition of heavy insulation creates challenges during mobile delivery. Finally, the operating characteristics of these pyrolysis reactors are heavily dependent upon feedstock characteristics. Changes to feedstock size, moisture content, or species will require the material transport mechanisms to be adjusted each time. Given the significant drawbacks to these reactor classifications, the screw-type pyrolizer was determined to be the optimal style for the continuous reactor. Screw-type pyrolizers are able to accommodate a larger range of feedstock sizes than other continuous reactor types since the material is pushed by the blades of the screw. Pushing of material via the screw decreases the necessary free board to approximately 40%, half of that required by the other reactor types. The decrease in free board allows for a more compact system design, which is ideal for mobile delivery. Ultimately, the screw-type pyrolizer design was chosen as it best facilitates the project objectives.

4.1.1. Heating System

The first system to be designed for the continuous biochar reactor was to facilitate the process heating. Due to the continuous nature of the system, the heating rate of the biomass

would be controlled solely by screw feeding mechanism. Thus, it was not necessary to design the heating mechanism to accommodate specific heating rates. However, increased heating rates would decrease the time required to bring the system to the process temperature during start-up. A decreased start-up time was desired, as it would maximize the production time of the system. To attempt to mitigate heat loss during operation, the decision was made to constrain the design to require internal process heating. Internal heating eliminates heat loss between the elements and the process and thus, decreases the amount of insulation needed on the reactor vessel. Several heating mechanisms were explored including: resistive, solar, laser, and inductive. Resistive or Joule heating is the most commonly employed industrial heating technology, which utilizes the flow of current through an electrical conductor to produce heat. Joule's First Law (Eqn. 1) states that the resistive heating power (P) equals the product of the square of the current (I) and the resistance of the conductor (R).

$$P = I^2 * R \tag{1}$$

The heating power range in resistive elements is governed by the selection of the electrical conductor. Power adjustments within that range are performed by adjusting the current through the material. While simple to design and operate, most resistive heating systems are constrained to maximum heating rates of 10°C/min (50°F/min) [56]. Consequently, the reactor would require upwards of one hour to reach the upper range of pyrolysis temperatures. Additionally, placement of resistive heating elements inside the corrosive environment process decreases their operational life. Solar heating was also explored, as utilization of this technology would eliminate the carbon footprint of the system. Solar heating utilizes the concentration of solar rays to a central focal point using parabolic mirrors. Due to the dispersed nature of light, achieving elevated process temperatures using this mechanism is requires an extensive array of heliostats and heat exchangers, making this technology undesirable for mobile delivery. Laser

heating utilizes a laser beam with a large power density to deposit energy into a material. One advantage to laser heating is the small heating area of less than 1mm (0.039in), which would facilitate a compact design. However, the limited heating area would also require a substantial decrease in production rates. Laser systems also necessitate large amounts of energy, with standard efficiencies being 50% [60]. The footprint of the laser power supply would substantially dwarf that of the reactor itself by approximately 300%. Ultimately, induction was chosen as the heating mechanism for the continuous reactor. Induction heating is commonly applied to metallurgical processes for its ability to provide contactless rapid heating. Rapid heating is able to be achieved due to the absence of the convective heat losses seen with other mechanisms. Induction operates by passing a high-frequency alternating current through a copper coil to produce an alternating magnetic field. This field penetrates conductive materials (susceptors) and generates electric currents known as eddy currents. The flow of the eddy currents through the susceptor encounter resistance and facilitate resistive heating. In induction, the resistive heating is generated from within the susceptor and thermal gradients cause the heat to flow outward to the rest of the system. This heating mechanism allows for high-efficiency contactless heating and facilitates the completion of the objectives for the system [61].

Design for the induction system began with the material selection (Fig. 12) for the reactor vessel and the susceptor.
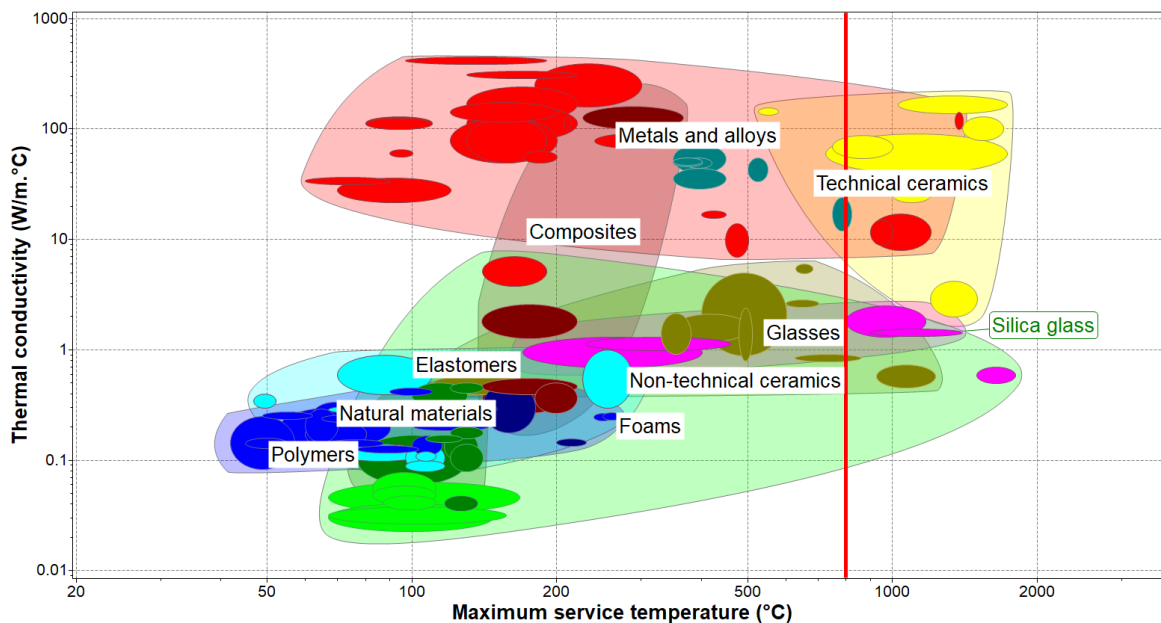
Figure 12: Material Selection Diagram (CES EduPack 2018) depicting thermal conductivity versus maximum service temperature to determine silica glass (quartz) for the reactor material. The temperature constraint of 800°C (1472°F) is represented by the vertical red line.

The reactor vessel material was required to be non-porous to seal under vacuum, able to withstand continuous operation at 800°C (1472°F), have low thermal conductivity to minimize the power consumption of the heater, and be non-magnetic to prevent interference with the inductive field. If the vessel coupled with the induction coil, the magnetic field would not reach the susceptor and heating would occur from the outside, not the inside as desired. Based upon these criteria, metals (conductivity), polymers (temperature), and most ceramics (porosity) were eliminated, with custom technical ceramics and glasses remaining. Quartz glass was chosen over technical ceramics for two reasons: technical ceramics are much more expensive due to complex fabrication processes and the quartz glass is translucent, offering in-situ views of the process. Additionally, the clarity of quartz glass facilitates the placement of an infrared temperature sensor to relay and control the process temperature. Finally, quartz glass has a maximum service temperature in air of 1100°C (2012°F), yielding a factor of safety of 1.375. The inductive

susceptor material (Fig. 13) was required to be able to withstand continuous operation at 800°C (1472°F), have high-thermal conductivity to provide uniform heating, and exhibit diamagnetic behavior to successfully couple with the inductive field.
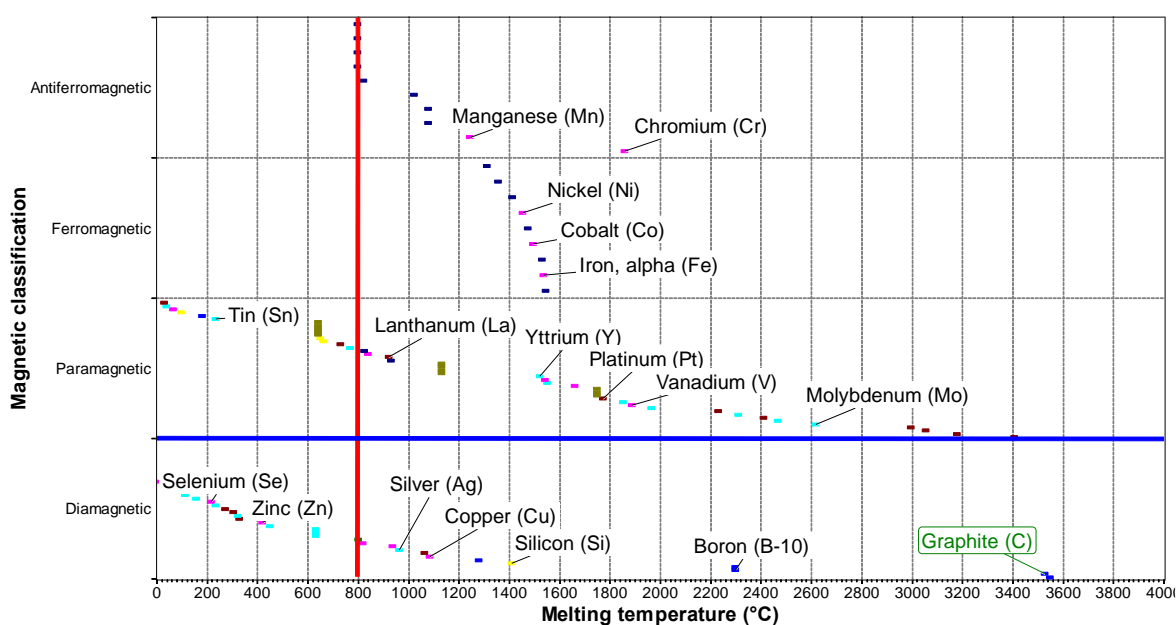
Figure 13: Material Selection Diagram (CES EduPack 2018) depicting magnetic classification versus melting temperature to determine graphite for the inductive susceptor. The temperature constraint of 800°C (1472°F) is represented by the vertical red line and the diamagnetic constraint is represented by the horizontal blue line.

Based upon these criteria, most metals and all polymers (temperature), ceramics (conductivity), and high-temperature steels (magnetic behavior) were eliminated. While high-temperature steels are useable to temperatures above 800°C (1472°F), but are not diamagnetic below their Curie temperature (~700°C (~1292°F)). Once the loss of magnetism occurs, heating control becomes difficult due to material properties changing from calibrated settings. Consequently, graphite was the chosen material for the susceptor. Graphite is commonly utilized commercially as an inductive susceptor for high-temperature applications [61]. The material is serviceable in vacuum systems up to 3000°C (5432°F), yielding a safety factor of 3.75. Due to

its placement inside the reactor, a large safety factor mitigates the concern of thermal runaway. Thermal runaway occurs when automation faults or process conditions cause an uncontrolled increase in the process temperature above the setpoint. Runaway often occurs due to trapped pockets of heat that are not recorded by sensors. With a maximum service temperature of 3000°C (5432°F), the graphite remains protected from thermal runaway events. This protection is desired due to the high-material cost of the graphite. Additionally, unanticipated degradation of the graphite will result in the accumulation of carbon in the produced biochar. Due to the high-carbon content of biochar, excess carbon from the graphite is not considered a contaminant and will not necessitate removal. Finally, graphite is considered a free-machining material, allowing for easy dimensional customization of the susceptor [62].

Given the materials selected for the reactor vessel and the susceptor and the desired process temperature range of 300°C-800°C (572°F-1472°F), the induction heating system (Fig. 14) was designed. MSI Automation (Wichita, KS) formulated a custom induction system to facilitate and control the process heating. The induction heater was comprised of three main components: copper coil, heat station, and power cabinet.
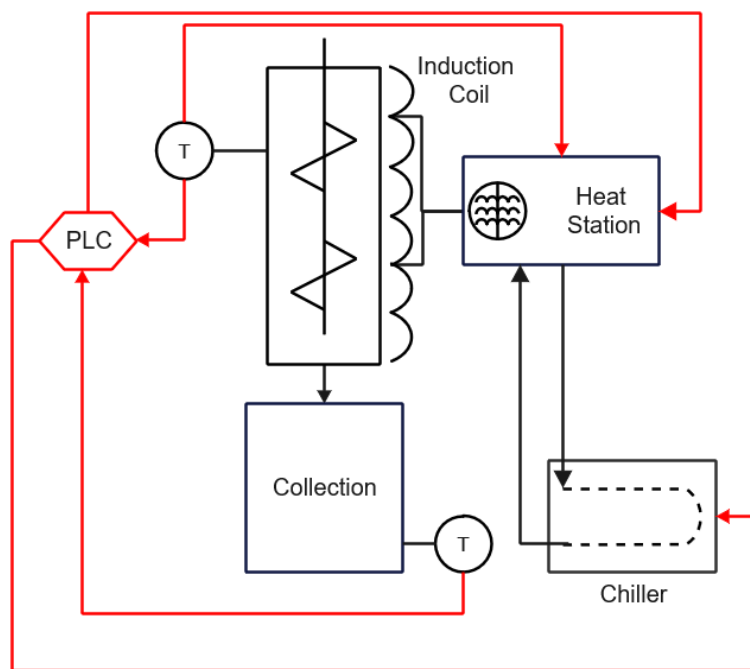
Figure 14: Heating system PID depicting the flow paths of process water (black) and control signals (red).

A power cabinet, constrained at 10kW (34121BTU/hr) by the electrical service at Montana Technological University, was designed to control the power supplied to the induction coil. The cabinet facilitates the regulation of power to the coil based upon feedback from a temperature sensor. An infrared laser temperature sensor was chosen for this system as it records the temperature from a location outside of the reactor. If the sensor was placed inside of the reactor, it would be exposed to the process temperatures and the metallic components could couple with the induction coil and generate a false reading. Due to the elevated process temperatures, an infrared sensor was not able to be sourced to sense temperatures over the entire range. Thus, a thermocouple was included in the design to provide temperature measurements below 150°C (302°F). A heat station was also designed, consisting of a transformer and capacitor bank, to generate the necessary outputs for induction heating. The heat station was connected to both power cabinet and copper coil. A copper coil was designed to provide the

geometry required to generate the inductive field in the reactor. The coil design was recommended by experts at MSI Automation to be sized 2.54cm (1in) larger in diameter and 5.08cm (2in) shorter in length than the reactor tube. This size mitigated risks of process heat melting the copper tubing and the inductive field coupling with other metal components in the system. Given the heat generated during operation, cooling water was required to ensure the integrity of the electrical components. The cooling water was required to remain at room temperature to prevent condensation on the plumbing, which would cause an electrical short. A recirculating chiller was chosen to remove heat from the water and bring the temperature down to ambient.

A final concern with the utilization of the induction heating system was the occurrence of thermal shock to the reactor materials. Thermal shock results from the formation of thermal stresses induced by heating. During process heating and cooling, thermal gradients are introduced into the reactor, causing cyclic tensile and compressive stress in the components. Thermal stresses in excess of the material yield strength result in fatigue failure of the components, thermal shock [63]. The two materials of concern were the fused quartz reactor tube and graphite auger. Given the lesser magnitude of the tensile strength, the thermal stress was compared to this material property to determine the in-service safety factor. As the components were fixed at each end, thermal stress, σ, was calculated (Eqn. 2) using the elastic modulus, E, coefficient of thermal expansion, α, and rise in temperature, ΔT.

$$\sigma = E * \alpha * \Delta T \tag{2}$$

Given the material properties for the graphite and quartz from the manufacturer and an increase in temperature of 780°C (1436°F), the stress safety factors were 1.55 and 7.42 for the fused quartz and graphite, respectively.

4.1.2. Syngas Handling System

To satisfy the second condition of pyrolysis, oxygen-deficiency, the syngas handling system was designed. With the project objective to eliminate the reliance upon process consumables to allow for mobile delivery, the utilization of an inert purge gas was eliminated. The remining mechanism to ensure oxygen-deficiency in the reactor was to operate under vacuum conditions. Operating under vacuum also serves to confirm the utilization of a graphite susceptor. In the presence of air, graphite begins to oxidize and degrade at temperatures as low as 600°C (1112°F), but remains serviceable up to 5000°C (9032°F) under vacuum [64]. The vacuum conditions imposed on the system will serve to remove the evolved syngas from the process as well. The system (Fig. 15) was designed to consist of three main components: vacuum pump, cold trap condenser, and digital vacuum gauge.
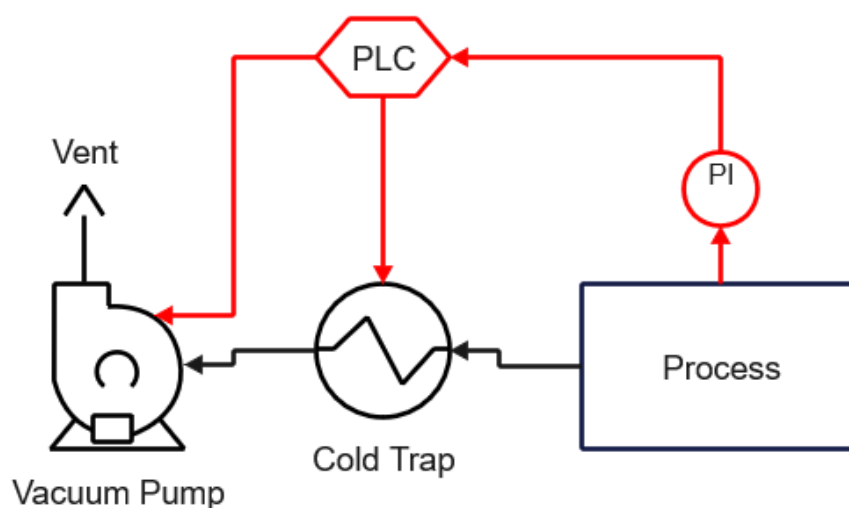
Figure 15: Syngas handling system PID depicting the flow paths of syngas (black) and control signals (red).

The HiScroll 12 vacuum pump, sourced from Pfeiffer Vacuum, was utilized to facilitate and control the vacuum pressure in the reactor. Scroll pumps are dry and oil-free and rely upon rotating spirals to remove gas from a system. The HiScroll 12 is equipped with an integrated drive, control unit, and pressure sensor in a PID loop to accept and hold a pressure setpoint. The setpoint is achieved by altering the throttling speed of the pump. Additionally, engagement of the gas ballast bleeds air into the system if power is lost. Existing vacuum pyrolysis reactors operate at pressures between 0.1Torr (0.002psi) and 150Torr (2.9psi). The ultimate pressure of the HiScroll 12 is 0.04Torr (0.0008psi), yielding a safety factor of 2.5. The maximum pumping rate was critical to ensure that all evolved syngas was removed and did not saturate the system with combustible gas. Assuming that the 70% mass lost during pyrolysis was lost instantaneously, the maximum rate of syngas formation would be 0.1948lpm (0.00688cfm). This assumption was based upon data collected during previously published experiments [21]. The maximum pumping rate of the HiScroll 12 is 201.67lpm (7.12cfm), yielding a safety factor of 1034.88. The cold trap, sourced from SH Scientific, was utilized to trap the condensable components of the syngas. A cold trap is comprised of a chilled vessel with process gas plumbed into the bottom. In order to reach the exit of the vessel, the flow path of the gas reverses direction and returns upwards. By switching the direction of fluid flow, the gas reduces velocity and undergoes an increased residence time. This increased residence time facilitates a large decrease in gas temperature, causing condensation. Cold trapping served to both eliminate harmful bio-oil condensation in the vacuum pump and facilitate easy collection for future research. The component employed three in-line cold traps immersed in a chilled ethylene glycol. According to industrial experts, the temperature of the cold trap should be at least 50°C (122°F) lower than the lowest species condensation temperature [65]. Given that laboratory

temperatures were controlled to 20°C (68°F), any species that may condense in the pump could be condensed by a -30°C (-22°F) cold trap. Thus, a -40°C (-40°F) cold trap from SH Scientific was selected, yielding a safety factor of 1.33. The digital vacuum gauge, sourced from Pfeiffer Vacuum, was integrated to provide the in-situ vacuum pressure and to quantify the difference between the pressure at the pump inlet and the process. Sensing the difference between the pressure sensors facilitates the ability to recognize leakage or obstructions in the system. Finally, the syngas handling system was designed to be connected to the pyrolysis reactor in a modular fashion to accommodate replacement with future syngas handing systems.

4.1.3. Material Transport System

The material transport system was designed to facilitate the continuous movement of biomass from the inlet hoppers, through the heating zone, and into the collection bin. Most crew-type pyrolizers are horizontally oriented. To maximize space for mobile delivery, the decision was made to orient the system vertically. In this configuration (Fig. 16), feedstock in the inlet hopper would fall due to gravity, slowed to the desired speed with the screw auger through the heating zone, and be dumped into the collection bin.
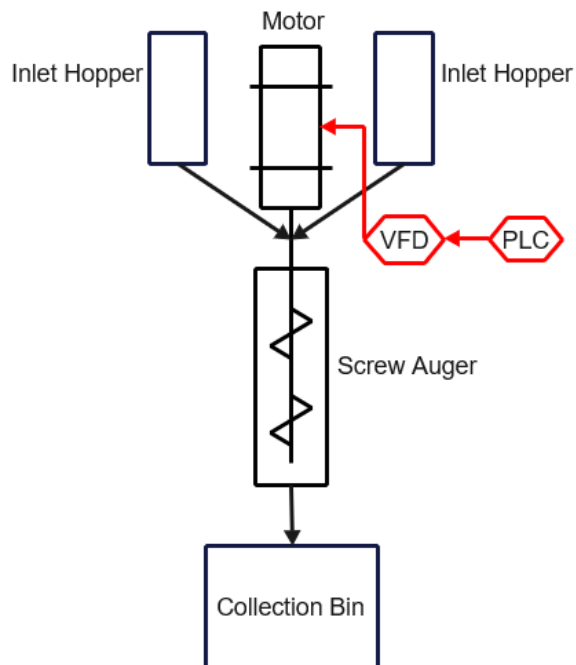
Figure 16: Material transport system PID depicting the flow paths of biomass (black) and control signals (red).

The capacity of the system was the next determination to be made. The objective of the reactor was to increase the production of biochar from the existing ~6.0g (0.035oz) batches. Discussions with researchers at Montana Technological University regarding preferred quantities of biochar yielded capacities of approximately 1.0kg (2.2lb). A safety factor of 2.5 was applied to this amount to mitigate concerns that 100% of the material would not migrate through the system as desired. At the time of design, the feedstock material planned for use in the reactor was industrial hemp (*cannabis sativa*). Assuming a uniform bulk density of 200kg/m^3 (12.49lb/ft^3) and that biochar yields are 25% by mass during production, the required feedstock volume to produce 2.5kg (5.5lb) of biochar is 0.05m^3 (1.77ft^3) [66,17]. With the system having a vertical orientation, two inlet hoppers with volumes of 0.025m^3 (0.885ft^3) were utilized to satisfy the volume requirement, simultaneously removing the screw auger from the interior of the hoppers. The collection bin at the termination of the process was sized with a larger volume for

several reasons: to support and distribute the weight of the reactor above, to facilitate space for integration of vacuum and sensor connections, and to allow for the placement of collection receptacles.

Due to the mobile nature of the system, the decision was made to design the screw auger to act as the inductive susceptor to decrease the size of the reactor. Thus, the presence of the auger within the inlet hopper would provide undesired and uncontrolled pre-heating. Raw graphite material was sourced from Ohio Carbon Blank (Willoughby, OH) upon the recommendation of both MSI Automation and faculty at Montana Technological University. Design engineers at Ohio Carbon Blank selected AR-12 (Table 1) for the auger based upon several criteria [67].

Table 1: Ohio Carbon Blank AR-12 Graphite material properties. Table adapted from [67].

AR-12 Graphite Material Properties and Characteristics			
Density	1.82g/cm^3	Max. Service Temperature	2760°C
Elastic Modulus	10.1GPa	Thermal Conductivity	112.4W/m^{2}K
Flexural Strength	58MPa	Thermal Expansion	5.90E-6°C^{-1}
Compressive Strength	127MPa	Poisson's Ratio	0.31
Tensile Strength	34.5MPa	Vickers Hardness	491HV

As opposed to extruded or laminated materials, AR-12 is molded and thus exhibits isotropic physical properties. Isotropic properties were ideal for the auger as the component would be experiencing both compressive and shear forces during operation. AR-12 was primarily chosen for the auger due to its high-strength properties. During operation, the compressive forces on the auger would be due to the material weight, so these forces were considered negligible. The most significant forces on the auger would be the shear stress upon the end of the component, opposite the motor. Maximum shear stress, τ_{max}, was calculated (Eqn.

3) with the maximum torque from the motor, T_{max}, the radius of the end of the auger, r, and the polar second moment of area, J.

$$\tau_{max} = \frac{T_{max} * r}{J} \qquad \text{(3)}$$

Given the maximum torque of 32.00N*m (283.25lbf*in) and radius of 0.013m (0.5in), the maximum shear stress on the auger would be 1.24MPa (180.32psi). Shear strength of a material is commonly approximated as 60% of the ultimate tensile strength [68]. The shear strength of AR-12 was approximated to be 20.68MPa (3000psi), yielding a safety factor of 16.64. American Society of Mechanical Engineers (ASME) B31.3 302.3.1(b) stipulates that the allowable shear stress on a shaft can be 80% of the shear strength, yielding a safety factor of 13.34 on the standard [68]. Given the auger material selection, the geometry of the component was designed. The American Society of Agricultural and Biological Engineers (ASABE) EP389.2 stipulates the pitch of flighting (distance between blades) to be between 0.9 and 1.5 times the diameter of the shaft [70]. Additionally, industrial experts recommend a flighting pitch of 1.0 times the shaft diameter for dry powders [71]. Designing an auger with standard pitch for use on powders facilitates a range of loading ratios between 40% and 45%, generating a capacity of 0.046kg (0.10lb) of hemp biomass for 0.0245m (1.0in) of blade length. Increasing the capacity of the auger by enlarging the blades was desired to boost the production rate of biochar. In order to facilitate standard flanged connections, which will be presented later, the auger vessel was designed to have an inner diameter of 0.12m (4.75in). Allowing for material bypass to mitigate the risk of binding and breaking the auger, the outer blade diameter was given 0.002m (0.075in) of clearance. The final design of the auger (Fig. 17) resulted in 0.12m (4.6in) diameter blades on standard pitch around the 0.051m (2in) shaft with a per blade capacity of 0.15kg (0.33lb).
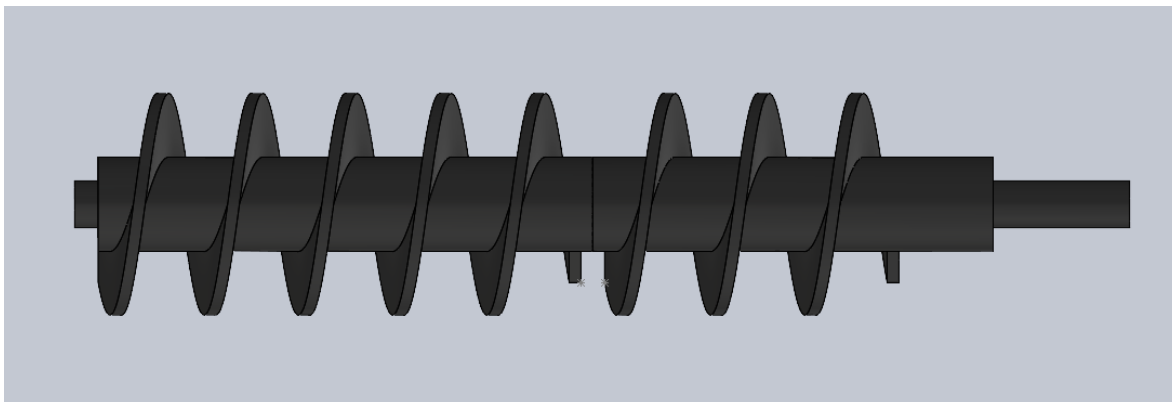
Figure 17: 3-D Model (SolidWorks® 2022) of graphite transport auger with 0.12m (4.6in) diameter blades on a standard pitch.

An additional consideration made for the material transport system was the electric motor to rotate the auger and transfer material through the heating zone. Due to the size constraints of mobile delivery, the system was designed to be as compact as possible. Consequently, production methods requiring extended dwell times result in low feed speeds. To facilitate precise control at low speeds, a step motor was needed. Opposed to other types of motors, step motors are driven by square wave to impart a partial rotation (step) on the shaft. This control allows for infinitely low speeds to be achieved. Additionally, bipolar step motors operate in the clockwise and counterclockwise directions. In this system, stepping forward and back can serve to keep the feedstock agitated with low feed speeds. Most step motors rotate in 1.8-degree steps. Given a heating zone of 0.31m (12in), a residence time of one hour would require 11 seconds between steps. With negligible resistance due to the auger, the motor selection was largely unconstrained. To minimize cost, a standard step motor (STP-MTRACH-42202) was sourced from Automation Direct. Due to the high-thermal conductivity of the graphite auger, the connection between the motor and auger could reach 800°C (1472°F) during operation, 730°C (1346°F) above the temperature rating of the windings. To mitigate this, a thermally resistive

shaft was placed between the two components. Height constraints on the system limited the shaft length to less than 0.31m (1.0ft). Given these parameters, a steady-state thermal simulation was completed in SolidWorks® 2022. SolidWorks® utilizes the geometry and thermal conductivity of the components to calculate the temperature of a meshed surface at steady-state conditions. Measurement of material characteristics using a meshed surface is classified as finite element analysis (FEA) [72]. The simulation (Fig. 18) assumed an isothermal auger of 800°C (1472°F), a uniform room temperature of 25°C (77°F), and a free-convection heat loss coefficient of 20W/m^{2}K (3.52Btu/hrft^2°F) to generate the necessary thermal conductivity for the temperature to reach 70°C (158°F) [21].
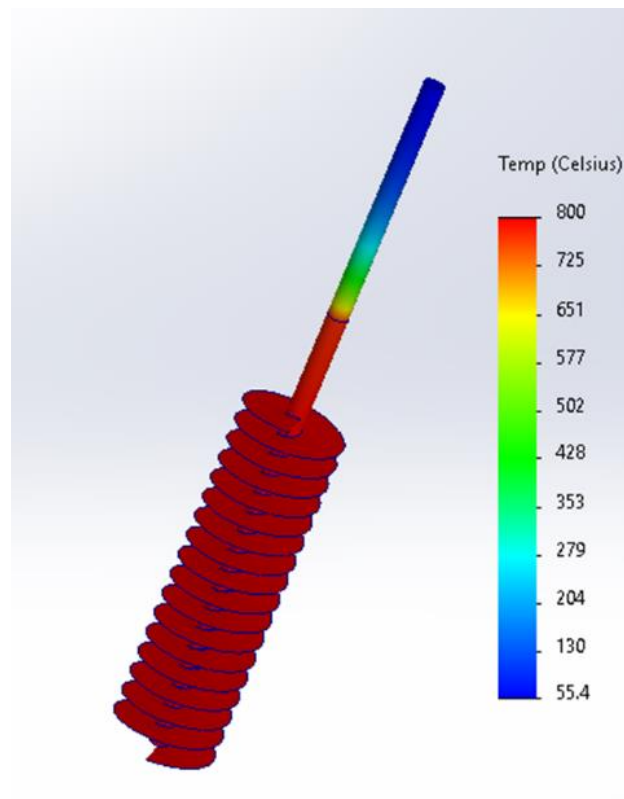
Figure 18: 3-D Model and Thermal Simulation (SolidWorks® 2022) of the graphite auger coupled to the insulating shaft to facilitate a temperature decrease from 800°C (1472°F) to 70°C (158°F).

The results of the simulation calculated the maximum thermal conductivity of the insulating shaft to be 2.5W/m^{2}K (0.44Btu/hrft^2°F) to decrease the temperature to 55.4°C (132°F), yielding a safety factor of 1.26. Given the low-thermal conductivity and elevated service temperature requirements, technical ceramics were explored. Normally, ceramics exhibit minimal strength under tensile and torsional loading. Due to the location between the component and motor, the ceramic was desired to have a shear strength greater than the graphite (>20.68MPa (>3000psi)) to eliminate twisting in the coupling. Any twisting in the insulating shaft would linearly magnify displacement down the length of the auger, crushing the graphite against the reactor vessel and leading to failure. The coefficient of thermal expansion of the insulator being greater than the graphite (5.90E-6°C^{-1} (3.28E-6°F^{-1})) was the final constraint of the insulating material. Otherwise, the larger amount of graphite expansion could potentially overstress the surrounding insulator and lead to fracturing. Astro Met, Inc. (Cincinnati, OH) recommended the utilization of yttrium-stabilized zirconia (Table 2), which was specifically designed for insulated shaft applications [73].

Table 2: Astro Met AMZIROX 86 YTZP material properties. Table adapted from [73].

AMZIROX 86 YTZP Material Properties and Characteristics			
Density	3.9g/cm^3	Max. Service Temperature	1093°C
Elastic Modulus	204GPa	Thermal Conductivity	2.1W/m^{2}K
Flexural Strength	1000MPa	Thermal Expansion	10.3E-6°C^{-1}
Compressive Strength	2500MPa	Poisson's Ratio	0.23
Tensile Strength	60MPa	Vickers Hardness	1290HV

The yttrium-stabilized zirconia (YTZP) developed by Astro Met satisfied all of the application criteria. A maximum service temperature of 1093°C (2000°F) ensures a thermal safety factor of 1.37. YTZP thermal conductivity of 2.1W/m^{2}K (0.37Btu/hrft^2°F) was also 16%

less than the system requirement, ensuring that the necessary temperature change would occur. The risk of failure due to uniform thermal expansion was also eliminated as the YTZP would expand 47% more than the internal graphite. Finally, the shear strength of YTZP was calculated to be 36MPa (5221psi) using the 60% of the tensile strength approximation [69]. The YTZP satisfied the requirement of increased shear strength compared to the graphite, with a safety factor of 1.74. Based upon the satisfaction of these criteria, the YTZP was chosen to be integrated into the system to provide insulation between the motor and graphite inductive susceptor. Vertical configuration of the rotating shaft allows for the motor, ceramic, and graphite to be attached with simple bolts and pins. The motor/ceramic connection was designed to be made from stainless steel and the ceramic/graphite connection was designed to be made from a sacrificial material. A sacrificial connection was necessary to mitigate binding and failure in the graphite auger. Step motors, by their configuration, are not able to be fitted with torque sensors. Ideally, a torque sensor would be fitted to the motor to provide a shutdown case for over-torque events to protect the component. Consequently, a sacrificial connection was designed to allow for free movement of the motor, independent of the auger in the event of binding. The pin itself was required to have low strength and fail in a brittle fashion. A common material that fits these criteria and handles the process temperatures is scored glass. Scored borosilicate glass has a fracture strength of 0.8MPa (116psi), which is 3.86% of the strength of the graphite auger [68].

The final design consideration for the material transport system was made for the fixtures on each end of the graphite auger. These fixtures were a crucial design feature to facilitate both sealing the rotating shaft under vacuum and holing the auger in position without the addition of friction. To ensure that the fixtures are frictionless, bearings were chosen. Bearings are

comprised of a rotating ring fixed to a shaft nested inside of a second ring that is fixed to a stationary plate. Motion of the inner ring and shaft is facilitated by rolling elements (spheres or cylinders) that are placed between the rings. Due to the presence of powders within the process, dust shields were required over the rolling elements to prevent seizing. The dust shields additionally facilitate vacuum sealing across the bearing. Most critically, the thermal expansion coefficient of the bearing was required to match the graphite ($5.90E-6°C^{-1}$ ($3.28E-6°F^{-1}$)). If the graphite expands faster, the bearing will be unable to rotate, and if the expansion is slower, the vacuum seal will be broken. With the high-service temperatures ($800°C$ ($1472°F$)), ceramics were the optimal class of materials for the bearing. Design engineers from Ortech Advanced Ceramics (Sacramento, CA) recommended silicon nitride full ceramic bearings. These bearings satisfy all of the decision criteria, with a thermal expansion of $5.76E-6°C^{-1}$ ($3.20E-6°F^{-1}$), within 2.5% of the graphite. With determination of these components, the material transport system design was completed.

4.1.4. Automation and Safety Systems

With the mechanical systems developed, the process design focused upon automation and safety considerations. Automation is an essential component of process design as it decreases the workload on the operator, ensures that the system is operated correctly, and facilitates the placement of safety interlocks to protect both the operator and the infrastructure. Additionally, automation infrastructure enables the recording of real-time process data. Collected process data can be integrated into a black box artificial intelligence (AI) system to facilitate machine learning for process optimization. The CVAP reactor was not designed with an AI system, but automation infrastructure was strategically designed to accommodate future integration. The central component of any automation system is the central processing unit (CPU). CPUs can be

integrated within computers or other devices to input, store, and output data in the form of

control signals. Previous research at Montana Technological University to develop the batch

pyrolysis furnace integrated a programmable logic controller (PLC) to facilitate process control.

PLC's utilize relay (ladder) logic programming to process input signals and output commands to

connected components or instrumentation (Fig. 19).
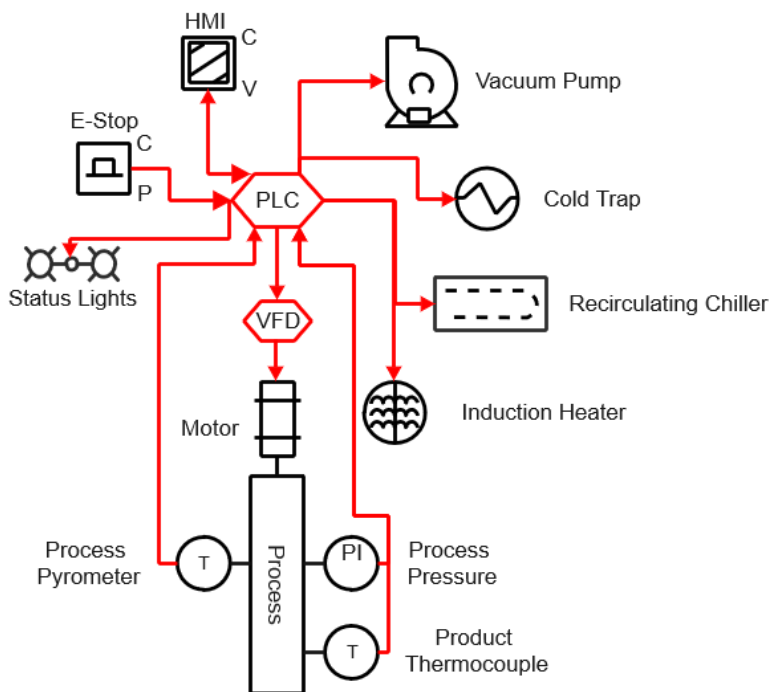
Figure 19: Automation and safety system PID depicting the flow paths of data and control signals (red).

Due to familiarity and past performance, the Allen-Bradley Micro800 Series PLC was

chosen for the system. Allen-Bradley is an industry leader in process automation and offers

open-source program software [74]. Additionally, Micro800 PLCs have a modular design,

allowing for customization to fulfill system requirements. To determine the optimal PLC model,

an approximation of the required input and output channels was made. Estimation of the signal

types (Table 3) and quantities was performed by inspecting the remote connections of the system

components.

Table 3: Automation system input and output requirements.

Channel Type	Connection Quantity
24VDC Power Supply	1
Human-Machine Interface (HMI)	1
Analog Input (AI)	1
Analog Output (AO)	1
Digital Input (DI)	4
Digital Output (DO)	4
Serial Module	3
Thermocouple Module	1

Using these requirements, Border States Electric (Missoula, MT) was contacted for a

recommendation, resulting in the selection of the Micro850 24-I/O PLC. This model was chosen

due to the requirement of three serial connections. On Micro850 PLCs, serial connections are

made using modules that attach to the front of the base deck. The 24-I/O model is sized to

accommodate three such modules. Digital connections are made to the base deck (of which there

are 24), with power, analog, and thermocouple connections made using expansion modules on

the sides of the base deck. With the exception of the serial connections, the PLC was designed

with numerous unused connection ports to facilitate future system expansions. To accommodate

operator inputs and process monitoring, a human machine interface (HMI) was included. The

HMI consists of a touch screen that enables the operator to read procedures, remotely control the

system, and view real-time process data. In accordance with ASTM B258-14, all system

components were connected to the PLC with 18-AWG solid copper wire [75]. To protect the

vacuum pump and induction coil, the cold trap and recirculating chiller were connected to a 24V solid-state relay to be energized during the entire length of the process. A variable frequency drive (VFD) was sourced from Automation Direct (Cumming, GA) to transfer control signals from the PLC to the step motor. The sensors integrated into the system: process pressure, process temperature, and product temperature were connected to modules on the PLC and the scaled data was output to the HMI control panel. Sensors also serve to provide logic conditions for the process automation. Process steps are determined by the pressure and temperature in the system. The system must be under vacuum before heating to prevent the graphite auger from sublimating. Furthermore, the system must be allowed to cool under vacuum to provide the same protection for the graphite and remove remaining process syngas.

A final addition to the automation system was the integration of several safety interlocks. The fume hood was equipped with two status lights, red and green, to inform the operator of the safety of opening the fume hood. This feature ensures that the reactor is not touched when under heat or vacuum. Two emergency shutdown buttons were also integrated into the system: on the HMI and fume hood. A digital button on the HMI is beneficial as the operator is encouraged to periodically check the displayed process data. In the event of power loss to the HMI, a physical button was also secured to the fume hood. To comply with NFPA 79, the button was wired normally-closed and fixed between 1.2m and 1.7m (4.0ft and 5.5ft) above ground level [76]. Beyond these safety features, a "what-if" analysis was conducted to ensure the safe shutdown of the system under foreseeable emergency conditions:

1. **Emergency shutdown button is engaged.**
   a. Induction heater and motor are de-energized. Vacuum pump, cold trap, and chiller run until the process temperature is less than 400°C (752°F) to protect the

graphite. Once all components are de-energized, the gas ballast bleeds ambient air into the system until equilibrium is reached.

2. **Total loss of system or PLC power.**

   a. All components are de-energized. The gas ballast in the vacuum pump bleeds ambient air into the system until equilibrium is reached. Reactor may be opened when power is restored and the pressure and temperature can be confirmed to be safe.

3. **Loss of power to the induction heater or motor.**

   a. Verification of the energized relay returns an error. Process automatically enters the emergency shutdown case.

4. **Loss of power to the vacuum pump, chiller, or cold trap.**

   a. Verification of the energized relay returns an error. Induction heater and motor are de-energized. The gas ballast in the vacuum pump will slowly bleed ambient air into the system until equilibrium is reached. Flow of air into the system will prevent condensation of syngas inside the pump.

5. **Loss of power to the emergency shutdown button.**

   a. Verification of the energized relay returns an error. Process automatically enters the emergency shutdown case.

6. **Loss of power to the HMI.**

   a. Manual emergency stop button may be pressed to engage the emergency shutdown case.

7. **Interruption of signal from any process sensor.**

    a. Sensor will return an error. Process automatically enters the normal shutdown case.

8. **Screw auger binds up inside the reactor.**

    a. A sacrificial scored glass pin snaps, allowing free rotation of the motor until the emergency shutdown button is pressed. The integrity of the auger is preserved and the pin is able to be replaced without deconstruction of the system.

9. **Process temperature exceeds the setpoint.**

    a. Engaged if the process temperature exceeds 25°C (77°F) above the setpoint. Process automatically enters the normal shutdown case.

10. **Process vacuum exceeds the setpoint.**

    a. Engaged if the process temperature exceeds 25°C (77°F) above the setpoint. Process automatically enters the normal shutdown case.

11. **Process vacuum is lost.**

    a. Engaged if the process pressure exceeds 50Torr (2.9psi). Process automatically enters the emergency shutdown case.

4.1.5. Reactor Vessels

The final design considerations for the CVAP reactor were to dimension the inlet hoppers, reactor tube, and collection bin. Production capacity requirements dictated the volume for each reactor section, but the geometry and material remained undefined. Quartz glass was previously selected for the reactor tube to accommodate the process temperature and inductive heating. Circular flanges were designed for each end of the tube to provide a sealing face to distribute the clamping force. The flanges mitigate the risk of crushing the quartz with the sealing clamps. In accordance with ASME Sec. VIII Div. 1, the allowable hoop stress on a

cylindrical pressure vessel must have a safety factor of 9.0 when compared to the material tensile strength [77]. Fused quartz glass has a tabulated design tensile strength of 48.3MPa (7000psi) [78]. Applying the required safety factor, the allowable hoop stress for the reactor tube was calculated to be 5.37MPa (778.9psi). Allen Scientific Glass (Erie, CO) was contacted to determine any fabrication constraints for the design. Fabricators stated that the minimum fabrication thickness for the component was 0.64cm (0.25in). Using this information, a FEA pressure simulation (Fig. 20) was conducted in SolidWorks® 2022 [72]. The component was dimensioned with a wall thickness of 0.64cm (0.25in). The properties of fused quartz were included and an external pressure of 760Torr (14.7psi) was applied to represent full vacuum at sea level.

Figure 20: 3-D Model and Pressure Simulation (SolidWorks® 2022) of the fused quartz reactor tube depicting a maximum hoop stress of 2.17MPa (314.7psi) under full vacuum conditions.

Results from the pressure simulation yielded a maximum hoop stress of 2.17MPa (314.7psi) under full vacuum conditions. The hoop stress safety factor in relation to the standard

was calculated to be 2.47. With the reactor tube fully defined, the material selection process

(Fig. 21) for the inlet hoppers and collection bin was performed.
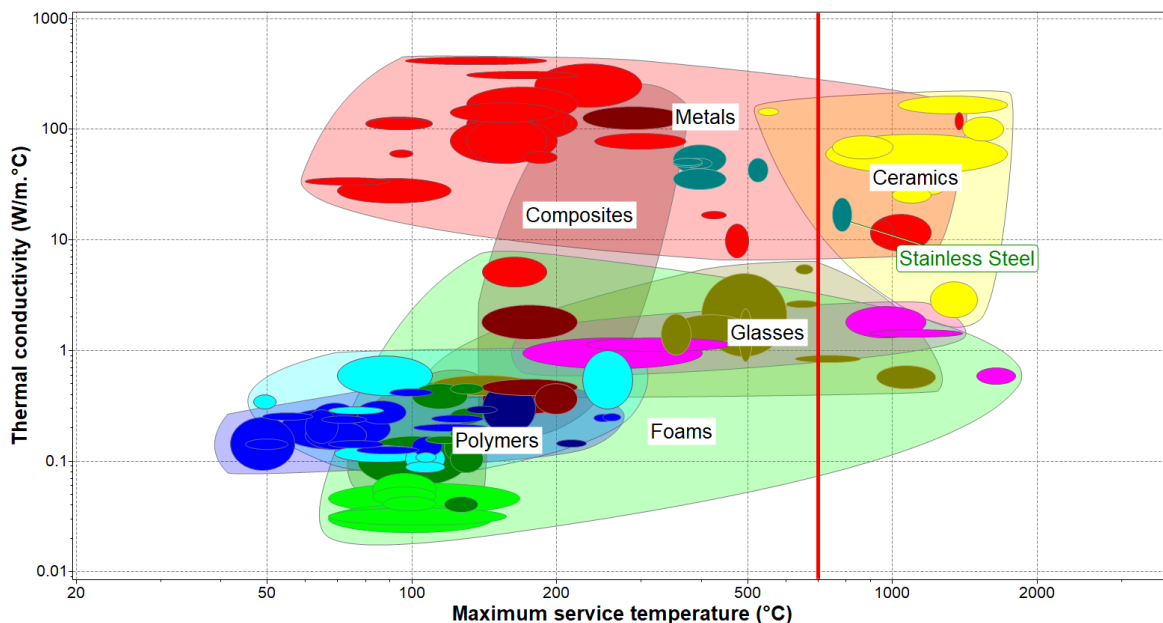
Figure 21: Material Selection Diagram (CES EduPack 2018) depicting thermal conductivity versus maximum service temperature to determine stainless steel for the inlet hopper and collection bin material. The temperature constraint of 800°C (1472°F) is represented by the vertical red line.

The material was required to have a high thermal conductivity to prevent the build-up of

heat outside of the induction zone, eliminating glasses and foams. Porous materials, ceramics

and foams, were rejected due to the sealing function of the components. Additionally, the

maximum service temperature was required to be greater than the process temperature of 800°C

(1472°F), eliminating polymers and composites. Finally, corrosion resistance was necessary due

to the presence of process syngas. The carbon dioxide-rich syngas, when combined with water

in the biomass forms carbonic acid upon heating. Carbonic acid corrodes carbon steels and low

alloys with an iron carbonate scale, which compromises the integrity over time. Thus, stainless

steels were determined to be the optimal material, and the determination of grade utilized cost as the governing factor (Table 4).

Table 4: 2022 cost ratios of common stainless-steel grades with respect to 316L. Table adapted from [79].

304L	RA309	RA310	316L	317L	RA321	RA330	410S
0.6	1.35	1.7	1.0	1.45	1.05	2.35	0.95

Given the stainless-steel cost ratios, grade 304L was chosen. The maximum service temperature of 304L is 870°C (1500°F), yielding a safety factor of 1.09 [80]. This small safety was not considered problematic as convective heat losses will substantially decrease the temperature where the components are located. 304L stainless steel was sourced from Hawe Steel Design (Butte, MT), who conducted a corrosion analysis in accordance with ASTM A262/14 and a chemical analysis in accordance with ASTM A751/20 (Table 5).

Table 5: 304L stainless-steel material properties. Table adapted from [80].

304L Material Properties and Characteristics			
Density	8.0g/cm^3	Max. Service Temperature	870°C
Elastic Modulus	196GPa	Thermal Conductivity	15.0W/m^{2}K
Ultimate Strength	595MPa	Thermal Expansion	17.0E-6°C^{-1}
Compressive Strength	260MPa	Poisson's Ratio	0.27
Yield Strength	207MPa	Vickers Hardness	159HV

The design of the inlet hoppers was chiefly determined by the feedstock volume and size constraints. The remaining space in the reactor fume hood constrained each inlet hopper to maximum dimensions of 53cm (21in) in height, 25.4cm (10in) in width, and 25.4cm (10in) in depth. To achieve the desired 0.025m^3 (0.885ft^3) volume, each inlet hopper was designed to this size and included a 45-degree bottom angle to facilitate free-feeding to the process. The angle of

repose, the minimum angle at which a powder will slide without assistance, was experimentally found to be 30-degrees for ground hemp using the ASTM D6393-08 standard procedure [81]. An additional 15-degrees was incorporated to accommodate less free-flowing feedstocks in future operations. The final design consideration to the inlet hoppers was the wall thickness. For cylindrical vacuum vessels, the wall thickness is determined by the allowable hoop stress. In the design of square and rectangular-sided vessels, the thickness is determined by the displacement of the faces under maximum pressure. To comply with ASME Sec. VIII Div. 1, a deflection of 1mm (0.039in) is allowed for every face length of 750mm (29.5in) [77]. Additionally, the inlet hoppers were designed to be fabricated from standard plates, which are produced in 25.4mm (0.125in) interval thicknesses. Given that the side lengths of the vessels were 254mm (10in), the deflection in the plates was required to be less than 0.34mm (0.013in). Using this information, FEA pressure simulations (Fig. 22) were conducted in SolidWorks® 2022 [72]. The component was dimensioned with wall thicknesses of 0.64cm (0.25in) and 0.96cm (0.375in). The properties of 304L stainless steel were included and an external pressure of 760Torr (14.7psi) was applied to represent full vacuum at sea level.
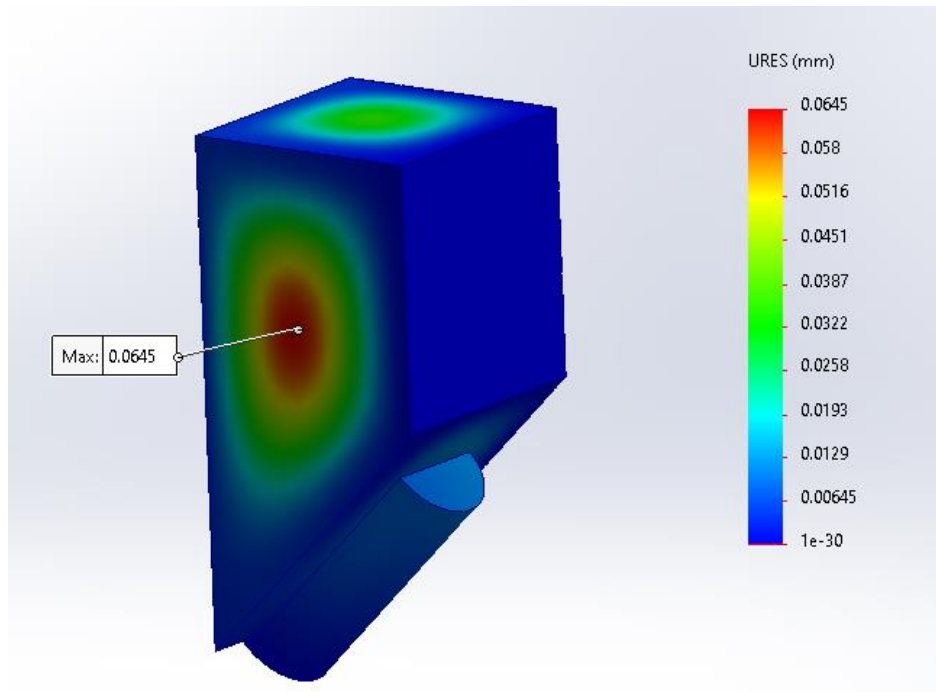
Figure 22: 3-D Model and Pressure Simulation (SolidWorks® 2022) of the 304L stainless steel 0.96cm (0.375in)-wall inlet hopper depicting a maximum resultant displacement of 0.0645mm (0.0025in) under full vacuum conditions.

Results from the pressure simulations yielded a deflection greater than 0.34mm (0.013in) for the 0.64cm (0.25in)-wall inlet hopper and a lesser deflection for the 0.96cm (0.375in)-wall inlet hopper. The maximum deflection of 0.0645mm (0.0025in) yields a safety factor of 5.27, facilitating compliance with the pressure vessel code.

The final vessel to be designed was the collection bin to allow for the easy removal of produced biochar. Similar to the inlet hoppers, the geometry of the collection bin was constrained by available space within the fume hood to maximum dimensions of 45.7cm (18in) in height, 50.8cm (20in) in width, and 50.8cm (20in) in depth. The collection bin was also required to hold volume larger than the $0.05m^3$ ($1.77ft^3$) of the inlet hoppers to facilitate the use of secondary containers and placement of access infrastructure. Given these constraints and the

goal of eliminating wasted space in the fume hood, the decision was made to utilize the full available dimensions. A rectangular geometry was chosen for the collection bin as well to facilitate ease of sealing access panels across a flat face. To comply with ASME Sec. VIII Div. 1, a side length of 457mm (18in) limits the deflection in the plates to be less than 0.67mm (0.026in) [77]. Using this information, FEA pressure simulations (Fig. 23) were conducted in SolidWorks® 2022 [72]. The component was dimensioned with wall thicknesses of 0.96cm (0.375in) and 1.27cm (0.5in). The properties of 304L stainless steel were included and an external pressure of 760Torr (14.7psi) was applied to represent full vacuum at sea level.
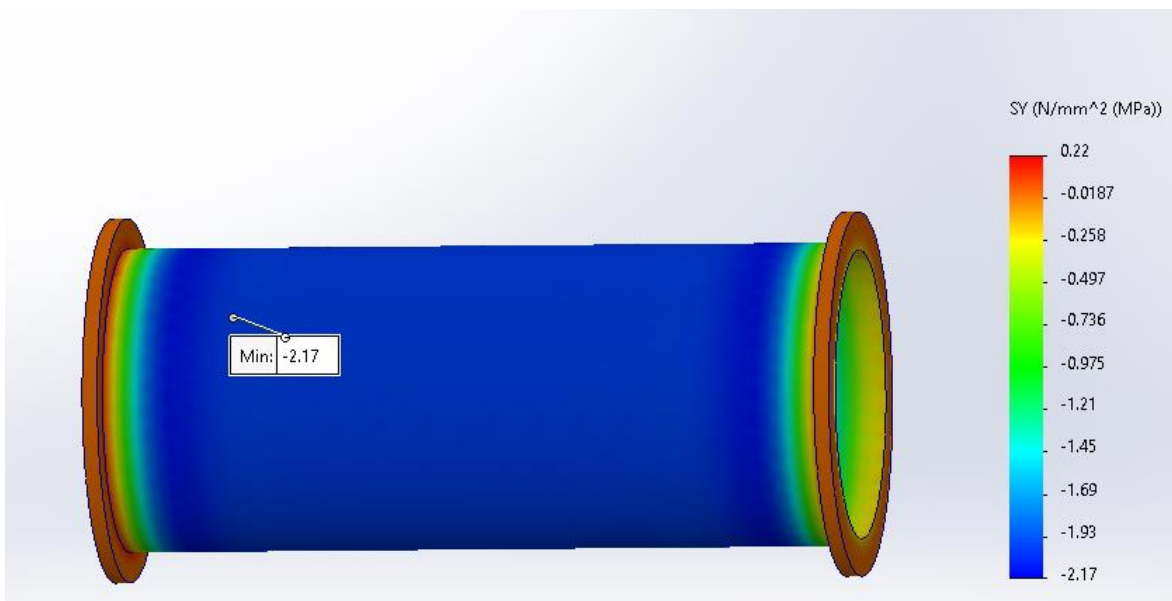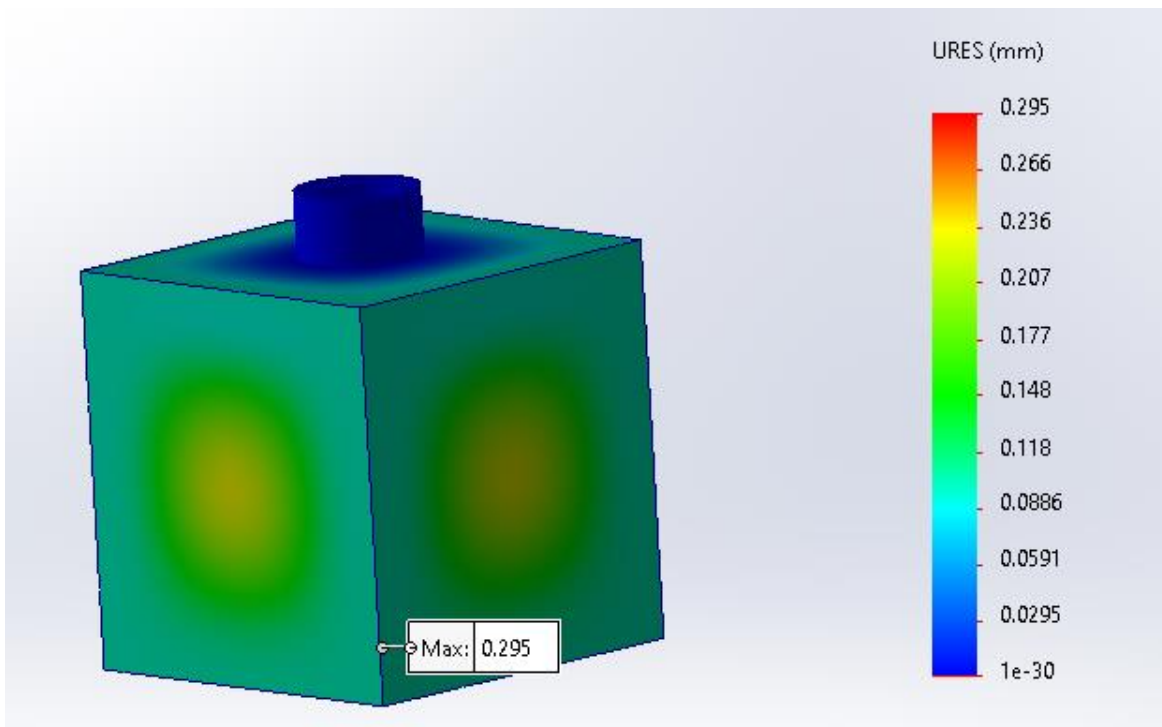

Figure 23: 3-D Model and Pressure Simulation (SolidWorks® 2022) of the 304L stainless steel 1.27cm (0.5in)-wall inlet hopper depicting a maximum resultant displacement of 0.295mm (0.012in) under full vacuum conditions.

Results from the 0.96cm (0.375in)-wall collection bin pressure simulation yielded a deflection of 0.62mm (0.024in) and a safety factor of approximately 1.0. Due to the on-site

fabrication of the system by uncertified personnel, this was deemed unacceptable. Additionally, deflection of any significance could damage the rest of the system as the collection bin is configured to support the reactor above. The maximum deflection of 0.295mm (0.012in) from the 1.27cm (0.5in)-wall collection bin pressure simulation yielded a safety factor of 2.27, facilitating compliance with the pressure vessel code.

With all system components fully defined and selected, a comprehensive model was compiled in SolidWorks® 2022 (Fig. 24) and a bill of materials was formulated (Appx. A). This model served as a detailed template for the fabrication and assembly of the CVAP reactor.
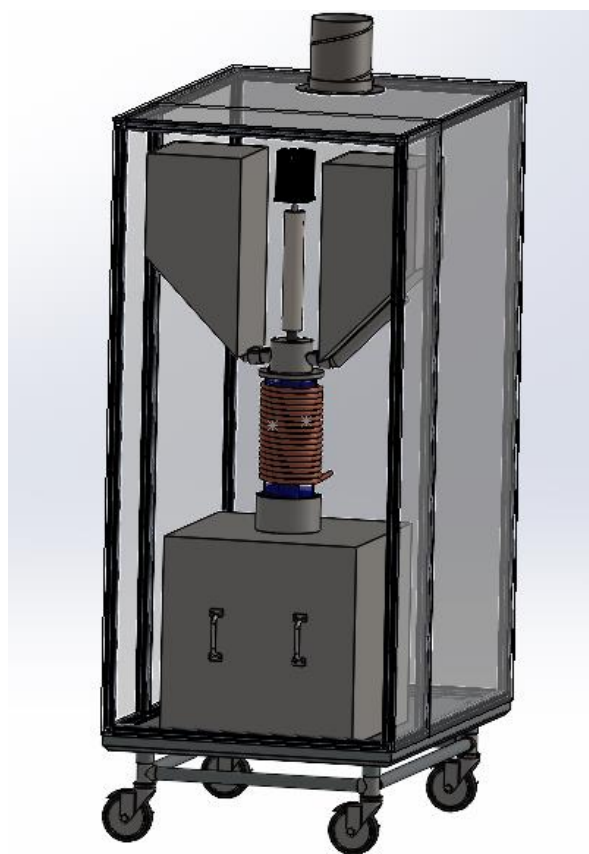
Figure 24: 3-D Model (SolidWorks® 2022) of the complete CVAP reactor depicting the pyrolysis reactor, processing equipment and portable fume hood.

4.2.   Fabrication

Fabrication of the CVAP reactor began with the inlet hoppers and collection bin. 304L stainless steel panels were dimensioned in a 2-D sketch in SolidWorks 2022 for cutting. Dimensions were oversized by 1.01cm (0.4in) to accommodate facing. Cutting was performed using a STV®CNC SparX™505 plasma table (Fig. 25) operating at 65V, with a cutting speed of 26in/min and cutting height of 0.06in [82].
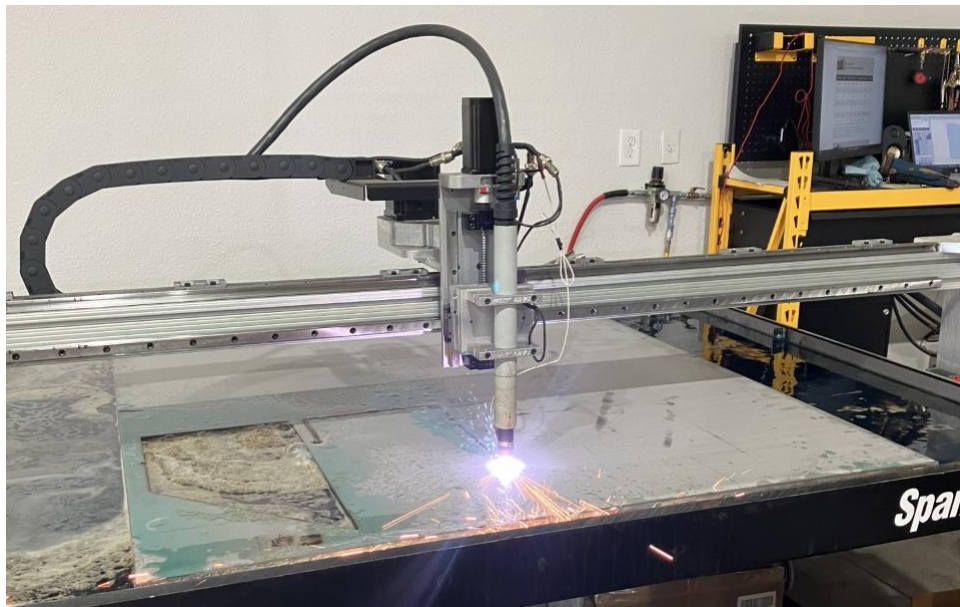
Figure 25: Plasma cutting inlet hopper components on STV®CNC SparX™505 plasma table.

After cutting, the panel sides were prepared for welding. To ensure optimal penetration on corner joints, half-open corner groove joints are recommended for plates heavier than 12-gauge [83]. The groove joints (Fig. 26) were designed with a 45-degree bevel through half of the thickness to align the corner, with the panel edges creating the weld groove.
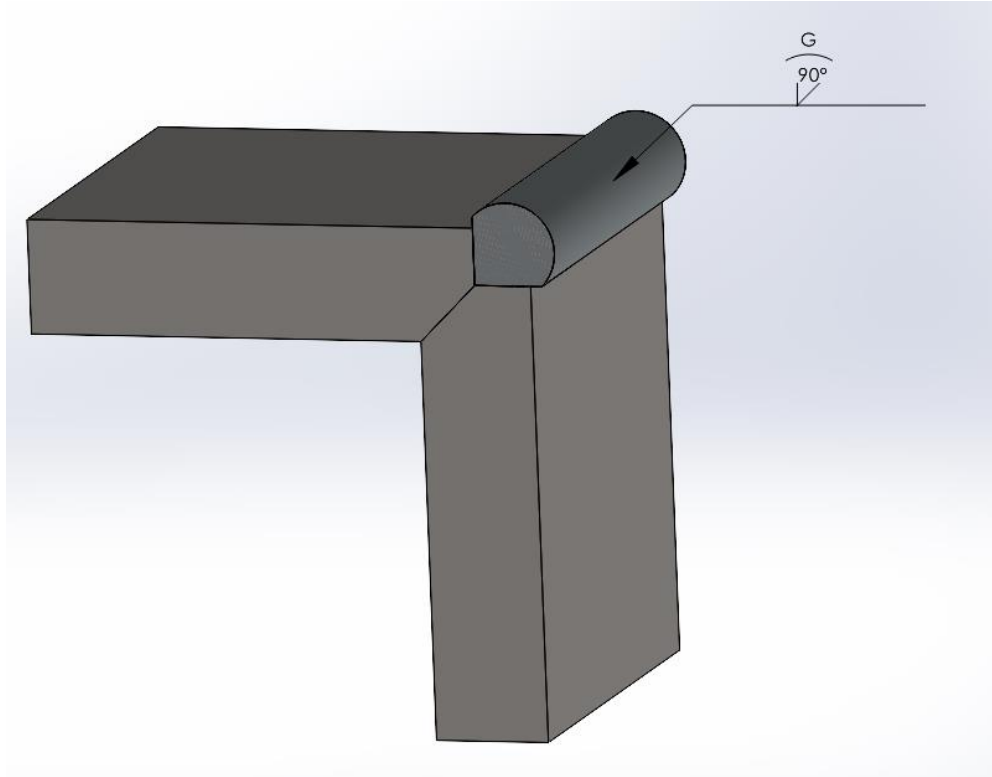
Figure 26: 3-D Model (SolidWorks 2022) of the half-open corner groove joint design depicting a 90-degree groove weld with convex profile grinding.

Utilizing half-open corner groove joint design, vacuum vessel standards do not require an additional interior weld, decreasing fabrication time and cost [83]. Additionally, AWS D1.1 details the structural welding codes for steels and recommends gas metal arc welding (GMAW) for welding half-open corner groove joints [84]. GMAW is accomplished by an electric arc formed between the metal and wire electrode inside an inter gas shielded region. AWS D1.1 specifies that the metal inert gas (MIG) welding subclassification of GMAW be employed for stainless steels [84]. During MIG welding, the wire electrode is mechanically fed through the welding gun at a constant rate, facilitating uniform penetration while the inert gas shield protects the weld pool from contamination. The inert shielding gas was selected based upon recommendations from industrial MIG welding experts. For all thicknesses of stainless steels, mixed shielding gas with 98% argon and 2% oxygen is desired to improve puddle fluidity,

coalescence, and bead contour [85]. During stainless steel welding, the selection of filler metal

grade is crucial to manage dilution affects to generate the desired ferrite to austenite ratio (F:A).

The F:A ratio offers a quantification of the strength and ductility of the weld. Extreme values of

either behavior will cause the weld to fail during service. AWS A4.2 specifies pre-approved

filler metals for common stainless steel base metals and provides a graphical method for

justification [86]. For 304L base metal, the standard recommends the use of 308L filler rod. The

WRC-1992 constitution diagram (Fig. 27) offers a graphical justification for acceptable

combinations of base and filler metals. Construction of this diagram involves the calculation of

the chromium and nickel equivalents present both metals, which serve as cartesian coordinates.

After plotting these points, the midpoint is taken and compared to the acceptable F:A range.
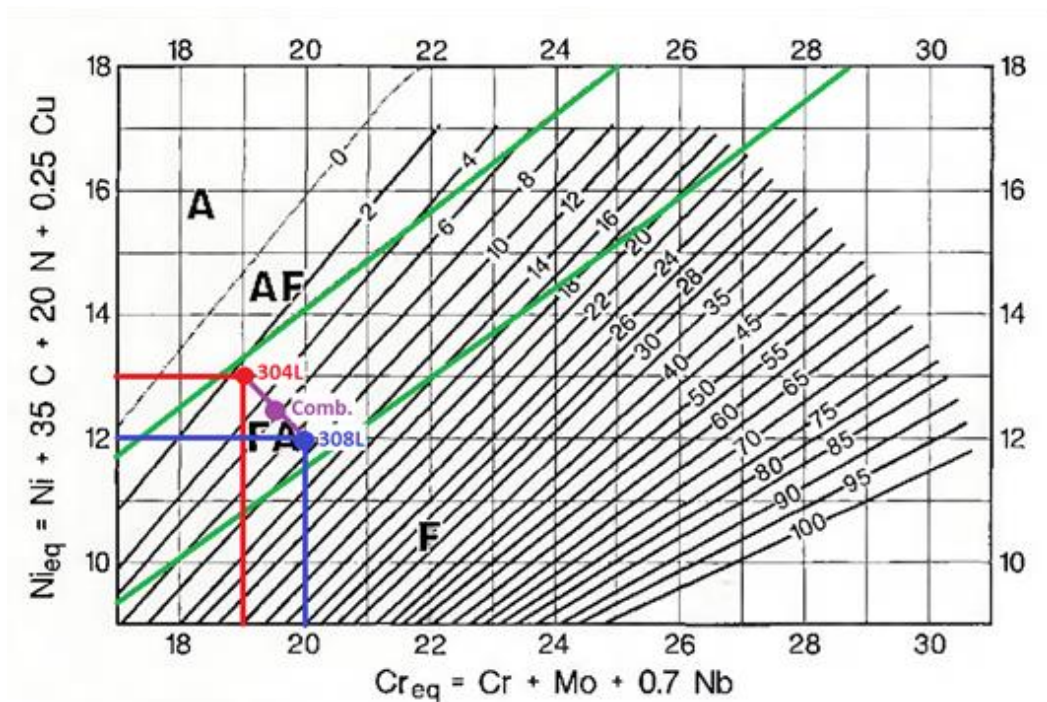
Figure 27: WRC-1992 constitution diagram for stainless-steel weld metals depicting the acceptable composition range in green, 304L composition in red, 308L composition in blue, and the resulting combination in purple to justify filler metal selection. Figure adapted from [86].

The graphical results from the WRC-1992 constitution diagram confirm the AWS A4.2 recommendation for the use of 308L filler wire with 304L base metal. With the filler metal and shielding gas determined, the remainder of welding parameters were defined (Table 6). The in-house Lincoln Electric MIG welder utilized a maximum filler wire size of 0.0889cm (0.035in). Given the plate thickness and depth of groove weld, thicker filler was desired to eliminate the need for multiple welding passes. Multiple-pass welding should be avoided if possible as it results in weaker, layered microstructures [87]. Sample welds were made with adjusted travel speeds and voltages until the penetration and weld morphology were satisfactory.

Table 6: Inlet hopper and collection bin MIG welding parameters.

Base	Filler	Wire Size	Shield	Travel Speed	Voltage	Position
304L	ER308L	0.035in	98%Ar/2%O_2	440ipm	24.8V	1F,2F

Fabrication of the inlet hoppers and collection bin was completed according to this procedure. After both vessels were constructed, the welds were ground into a convex profile flush with the corner plates. Grinding allowed for an improved aesthetic finish and created a clean surface for inspection. Additionally, all sealing edges were faced on a manual mill to ensure a level and uniform connection. In accordance with ASME Section V (inspection procedures) and ASME Section VIII (weld acceptance criteria), Welding Services Inc. (Butte, MT) was contracted to perform an inspection of all completed welds [88]. The inspection (Appx. B) consisted of three steps: negative pressure test, visual inspection, and dye penetrant test. The negative pressure test was performed by placing the vessel under vacuum, while monitoring the vacuum level with a digital gauge in accordance with ASTM E2930-13 [89]. Results from the test yielded a stable pressure over 10min. of 28.0Torr (0.037psi), yielding a safety factor of 5.36. A visual inspection was performed by the technician, examining welds for incomplete fusion, porosity, and cracking according to ASME Section V, Article 9 [88]. All

welds satisfactorily passed the visual inspection criteria. The final component of the inspection was the dye penetrant test conducted in accordance with ASME Section V, Article 6 [88]. The test involved solvent cleaning of the surface, application of penetrating dye (Fig. 28), removal of excess dye, and application of the developing agent.

Figure 28: Welding Services Inc. technician applying dye penetrant for weld crack and porosity inspection.

Upon application of the developing agent, the remaining dye is pulled to the surface in "bleeds", revealing porosity or cracking defects. Results from this inspection revealed one cracked weld, with the rest passing the inspection (Fig. 29)

Figure 29: Welded joints after completion of the dye penetrant test depicting an acceptable weld (right) and unacceptable weld with a root crack (left).

The root crack discovered during the inspection most likely resulted from surface contamination during welding. This conclusion was drawn due to the high-quality of the remaining welds, meaning that neither the designed procedure or overall execution were in error. During MIG welding copper contamination is common and results from the copper nozzle coming into contact with the molten weld pool. To mitigate the defect, the weld was removed and reapplied. The new weld was then subjected to visual and dye penetrant examinations to ensure complete removal.

With the inlet hoppers and collection bin completed, the flanged connections to the reactor tube were fabricated. Due to the custom nature of the system, these components were produced in-house. In total, two flanges with centering rings and two sealing ring flanges were fabricated. To ensure precise alignment of the sealing faces and bolt holes, the flanges were machined using a Haas TM Series CNC vertical mill (Fig. 30)
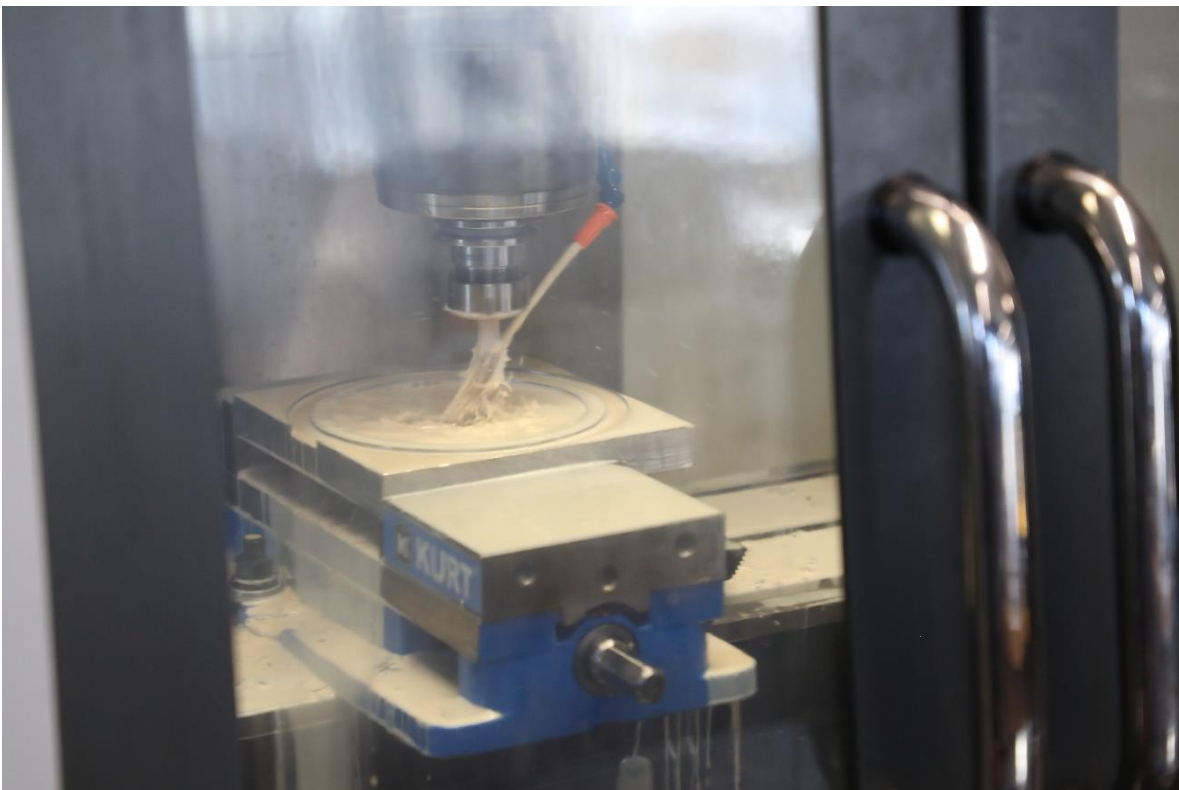
Figure 30: Machining stainless steel flanged connections with the Haas TM Series CNC vertical mill.

The final major component to be fabricated was the graphite screw auger. Several professional machinists were contacted, but were either unavailable or unwilling to accept the work due to the health hazards of graphite. Consequently, the screw auger was machined in-

house using available machinery. A precision machining instructor from Highland's College

(Butte, MT) was contracted to assist with the machining process. Due to the expense of graphite,

similarly-sized rounds were sourced to test the machining procedure. Delrin was recommended

due to the material exhibiting similar machining behavior to graphite. The machining process

was begun by turning the outer diameter and live ends on a manual lathe (Fig. 31).
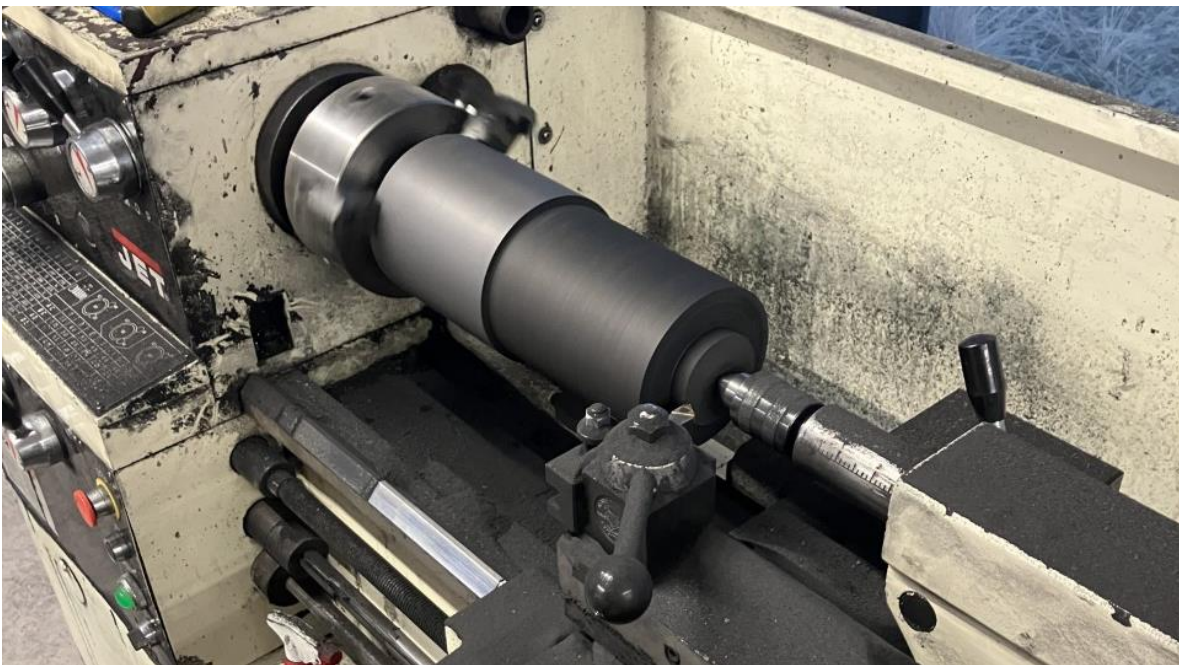
Figure 31: Turning the outer diameter and live ends on the manual lathe.

After turning in the manual lathe, the graphite was fixed into a Haas HPCL CNC lathe.

With the outer diameter machined manually, the CNC lathe was selected to machine the screw

flight. CNC machining was required to ensure a uniform pitch on the auger blades. G-code

(Appx. C) was generated using Mastercam and several iterations of Delrin were performed to

ensure the desired product. During the final iterations, it became apparent that utilization of a

stationary tool was not optimal. As the spiral cutting became deeper, tool pressure increased and

resulted in fracture of the component. To mitigate tool pressure, a lathe/mill (Fig. 32) was

designed. The stationary tool holder was replaced with a flat-nosed endmill bit on an electric

motor. The rotating cutting tool mitigated all tool pressure and facilitated a full depth of cut.

Figure 32: Machining the auger blades with the custom-built mill/lathe.

Delrin products from the mill/lathe were successful and the graphite was machined with

the same procedure. The resulting graphite auger required a post-machining sanding to achieve a

smooth surface finish.

With the screw auger completed, final assembly of the system was performed. A vented fume hood was constructed to remove any released process syngas from the laboratory. Furthermore, the panels on the fume hood mitigate the risk of harm to the operator in the event of a catastrophic implosion of the reactor. The fume hood was secured to a cart for future location changes and was connected to the in-house ventilation system. Assembly of the CVAP reactor system progressed from bottom to top. The collection bin, cold trap, chiller, and vacuum pump were placed in final positions and secured with locating brackets. All components were then plumbed together using readily available sanitary fittings, tubing, and hose clamps. The reactor tube and flanges were temporarily installed to vertically align the screw auger. Deviations from verticality in the auger could result in asymmetrical loading and failure of the component. The auger was vertically aligned inside of the reactor tube to ensure no contact with the walls of the vessel. Bearing mounts were then welded to the collection bin, fixing the auger in a vertical position. The inlet hoppers were fabricated and supported with extruded aluminum framing for positioning. Adjustable casters were installed to lower the inlet hoppers and create a sealed connection without loading the quartz reactor tube. Loading of the quartz tube could result in failure, compromising the structural integrity of the screw auger and overall system. Finally, the motor and insulating shafts were installed using dowel pin connections. Dowel pins were chosen due to ease of manufacturing and the presence of tensile loading on the vertical shaft. Installation of the motor completed the fabrication of the physical system components (Fig. 33).

Figure 33: CVAP reactor with completed assembly of the physical system components.

The sensing and automation components were installed after the physical system to ensure adequate spacing between heated surfaces and signal wiring. Wiring was secured unbundled and open-faced to facilitate future alterations and expansions. Additionally, terminal blocks were installed between the components and PLC. The blocks served to ground, isolate, and protect the automation circuits. Bussed terminal blocks were included to provide power to sensors from the PLC power module. All system wires were labeled with the origin and termination of the circuit for ease of modification and troubleshooting. System wiring was recorded in a wiring diagram (Appx. E). The process automation scheme (Appx. F) was constructed using Connected Components Workbench (CCW), the open-source software provided by Allen-Bradley. Logic code was developed for startup, operation, process monitoring, shutdown, and emergency procedures. The emergency procedures were developed using the previously presented "what-if" analysis threat cases.

4.3. Reactor Calibration

Calibration of the CVAP reactor began with sensing components using external verification. Output voltage from the process pressure gauge was converted into a readable pressure using an equation (Eqn. 4) provided by the manufacturer, where *P* is the pressure and *U* is the output voltage.

$$P[Torr] = (U - 1) * 93.75 \tag{4}$$

Sensor pressures were compared to an external instrument, and the rheostat was adjusted until the difference in measurement was less than 5%. To calibrate the IR temperature sensor, the emissivity of the quartz glass was loaded into the sensor memory. Graphite was heated to several temperatures between 300°C (572°F) and 800°C (1472°F). IR sensor measurements were compared to data from a handheld FLIR TG54 spot thermometer to ensure a difference of less than 5%. While testing the IR sensor, the sample K-Type thermocouple was allowed to rest on the graphite. Thermocouple data displayed on the PLC was compared to an identical thermocouple connected to a handheld meter and a less than 5% difference was verified over the temperature range. The step motor was calibrated over the predicted range of operating dwell times from 1min to 60min. Dwell times were input to the HMI and the motor was operated. Revolutions were timed with a manual stopwatch to ensure that the setpoint rotational speeds were achieved. The entirety of the automation logic was observed and debugged to ensure that desired operation was achieved. Finally, each case defined in the "what-if" analysis was replicated to ensure that the system responded accordingly.

4.4. Feedstock Preparation

Previous research at Montana Technological University selected industrial hemp (*cannabis sativa*) to be the feedstock for biochar production. The raw hemp was locally sourced

from Helena, MT and was harvested in 2019. Specifics were not given on the hemp outside of

male and female long stalk fiber variety plants. Hemp arrived pre-dried in large plastic

containers (Fig. 34).

Figure 34: As-delivered hemp feedstock material.

The as-delivered hemp was too large in length for feeding through the CVAP reactor.

Comminution (size reduction) was performed by feeding the hemp stalks through a Polymer

Systems® Plastic Shredder to create an acceptable particle size. Previous research at Montana

Technological University has determined that the plastic shredding procedure for hemp stalks is

adequate for feedstock pre-processing. The shredded feedstock (Fig. 35) was collected and

added to the batch furnace crucibles for production.

Figure 35: Shredded hemp biomass feedstock prepared for biochar production.

4.5.   Reactor Operation

Biochar was produced for the purposes of future reactor calibration and product characterization. The existing batch biochar reactor at Montana Technological University was operated to generate biochar utilized as the baseline of comparison for the CVAP reactor products. The batch biochar reactor was operated using previously developed automated and manual operating procedures. A standard operating procedure (Appx. G) was also generated for future use with the CVAP reactor. For production, 20.87g (0.74oz) of hemp feedstock was placed into quartz crucibles and pyrolysis was performed under specified conditions (Table 7).

Table 7: Batch biochar reactor operating parameters.

Peak Temperature	Heating Rate	Residence Time	Ar Flow Rate
450°C (842°F)	10°C (50°F)/min	60min	2.5Lpm (0.09cfm)

4.6. Chemical and Morphological Analysis

Chemical and morphological analyses were conducted to characterize biochar from the batch reactor to serve as a reference for future comparison with CVAP reactor products. The forthcoming analyses were conducted in triplicate, generating the minimum number of data points to achieve a standard deviation and ensure accuracy for analysis.

4.6.1. Thermogravimetric Analysis

Thermogravimetric analysis (TGA) was conducted using a TA Instruments Q500 TGA (Fig. 36). TGA offered quantification to the rate and amount of solid mass loss as a function of increasing temperature.

Figure 36: TA Instruments Q500 Thermogravimetric Analyzer. Figure as designed by [90].

TGA was performed to determine the maximum mass yield from specified pyrolysis conditions. Due to the high-surface area to mass ratio of the sample, the resulting maximized kinetics of the solid to gas conversion drove the pyrolysis reaction to completion. A comparison of the process yields on the basis of mass would reveal the presence of combustion (lower yield)

or incomplete pyrolysis (higher yield). The maximum mass yield was measured by replicating

reactor conditions within the TGA (Table 8).

Table 8: TGA maximum mass yield experimental parameters.

Peak Temperature	Heating Rate	Residence Time	Ar Flow Rate
450°C (842°F)	10°C (50°F)/min	60min	100mL (0.004cfm)/min

Ash content is the measure of the inorganic mass present in the biochar. The inorganic

mass, mainly comprised of mineral oxides, was measured in accordance with ASTM E1755-01

[91]. The procedure involved heating the hemp feedstock in air according to the ASTM standard

method (Fig. 37), with the final weight of the sample representing the ash content. Feedstock

ash content may affect adsorption behavior and should be characterized for application

experiments.
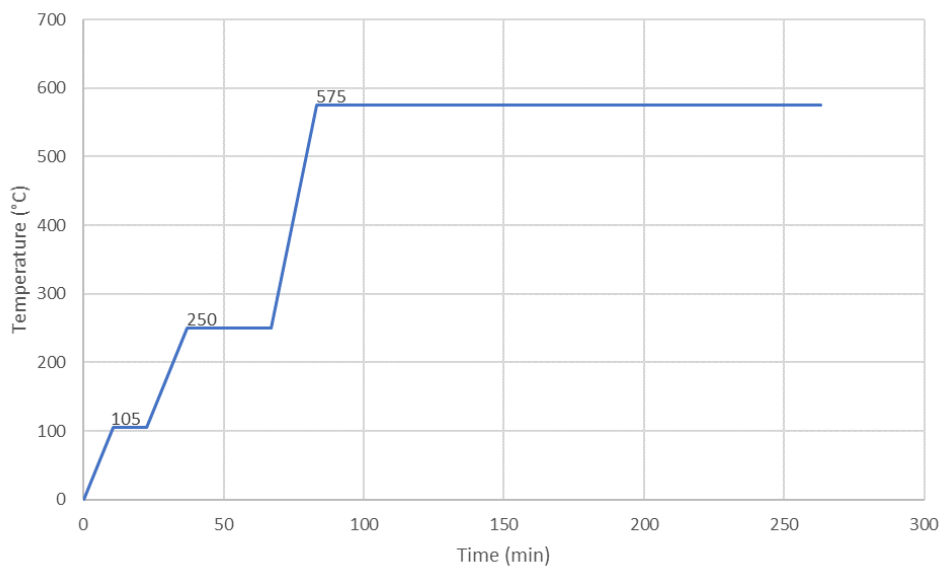
Figure 37: TGA determination of ash content in biomass heating profile. Figure adapted from [91].

4.6.2. Mass Spectroscopy

Mass spectroscopy (MS) was conducted using a Pfeiffer Vacuum ThermoStar™ GSD320 connected in series with a TA Instruments Q500 TGA (Fig. 38).
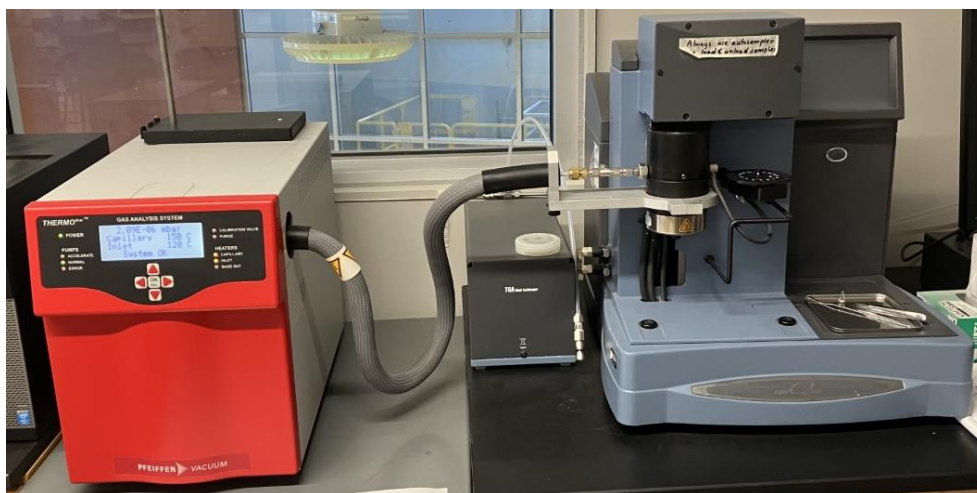
Figure 38: Mass spectroscopy experimental setup depicting a Pfeiffer Vacuum ThermoStar™ GSD320 MS (left) connected to the exhaust of a TA Instruments Q500 TGA (right).

Connection with the TGA was required to facilitate the formation of gas from the sample to be analyzed by the electron impact quadrupole MS. Biochar from the batch and CVAP reactors were examined by heating the samples in the TGA to 800°C (1472°F) with a heating rate of 5°C/min (41°F/min). The MS was calibrated to identify and quantify species in the evolved gas, specifically: water, nitrogen, carbon monoxide, methane, hydrogen, carbon dioxide, ethane, nitric oxide, propene, nitrogen dioxide, oxygen, oxygen-17, sulfur dioxide, and ammonia using bottled gases and stepwise dilution. The experiments were conducted with the Secondary Electron Multiplier (SEM) detector, a capillary temperature of 150°C (302°F), and an inlet temperature of 120°C (248°F) to prevent condensation. Results from these experiments may be used to determine the species, if applicable, that are not evolved due to incomplete pyrolysis.

4.6.3. Surface Area and Porosity

Surface area and porosity measurements were performed using the Brunauer–Emmett–Teller (BET) method with an Anton-Paar Nova 800 Physisorption Analyzer (Fig. 39).

Figure 39: Anton-Paar Nova 800 Physisorption Analyzer. Figure as designed by [92].

Produced biochar from the batch and CVAP reactors were collected and degassed. Degassing was performed at 240°C (464°F) for 240min under vacuum to remove residual species present on the surface due to contact with air. Surface area and porosity measurements were recorded during nitrogen and carbon dioxide adsorption experiments. Nitrogen adsorption was conducted at 77K (-321°F) in accordance with ASTM D6556 – 21 to measure meso and micropore diameters between >2nm (7.9E-8in) and 50nm (1.9E-6in) [93]. Carbon dioxide adsorption was conducted at 273K (32°F) in accordance with ISO 9277:2022 to measure micropore diameters less than 2nm (7.9E-8in) [94]. The specific surface area and pore size

distribution values may be compared to determine differences, if applicable, in process

conditions between both reactors, specifically temperature and heating rate.

4.6.4. Carbon-Hydrogen Ratio

The quantification of elemental composition, specifically the carbon to hydrogen ratio,

was conducted using a LECO Corp. CHN828 Elemental Analyzer. (Fig. 40).

Figure 40: LECO Corp. CHN828 Elemental Analyzer. Figure as designed by [95].

Measurement of carbon to hydrogen ratio was performed on products from the batch and

CVAP reactors according to ASTM D5373-21 [96]. Carbon to hydrogen ratios may be

compared to determine the uniformity of process temperature, if applicable, between the

reactors. Increased carbon in CVAP products would be indicative of higher process temperature,

while increased hydrogen would be indicative of a lower temperature.

4.6.5. X-Ray Diffraction

X-ray diffraction was conducted using a Bruker D2 PHASER Diffractometer (Fig. 41).
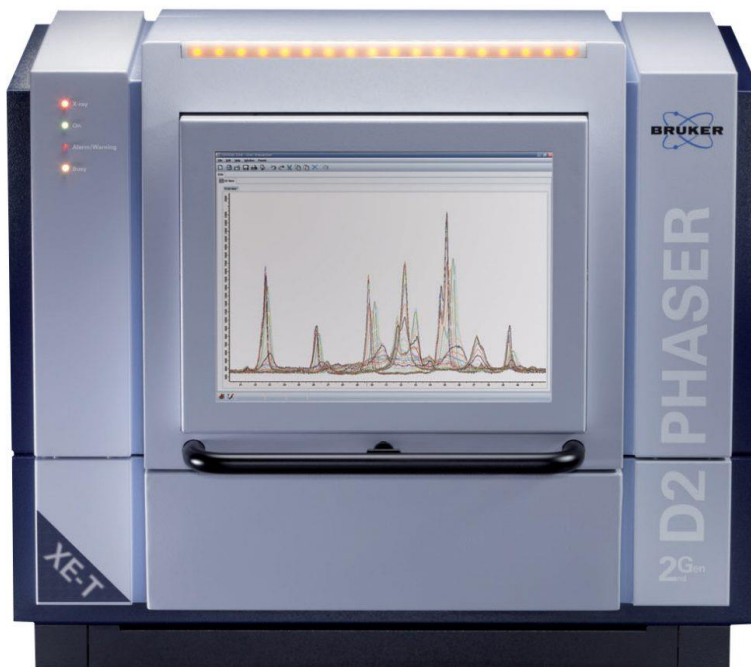
Figure 41: Bruker D2 PHASER X-Ray Diffractometer. Figure as designed by [97].

XRD measurements were conducted on biochar from the batch and CVAP reactors. The Coupled TwoTheta/Theta scan type was used to scan from 20° to 120° with a 0.01° step occurring every 0.19 seconds. The generated diffraction patterns may be compared to confirm the production of amorphous carbon structures within the biochar. The presence of crystalline structures would indicate either the retention of mineral oxides from the feedstock or the formation of graphitic structures due to undesired heating conditions. Identification of the mineral oxides may also indicate the compounds present in the ash obtained from the TGA experiments.

4.6.6. Raman Spectroscopy

Raman spectroscopy was conducted using a Renishaw inVia™ Raman Spectrometer (Fig. 42).

Figure 42: Renishaw inVia™ Raman Spectrometer. Figure as designed by [98].

Raman spectroscopy was utilized to quantify the sp^2 carbon structure and content of the biochar from the batch and CVAP reactors. Measurements were recorded with a 20x LWD objective and the 457nm (1.8E-5in) emission line from the argon laser at 3mW power in accordance with ASTM E131-10 [99]. Scans were taken between 500cm^{-1} (197in^{-1}) and 3500cm^{-1} (1378in^{-1}) with a 3-5sec. accumulation time to generate a desired signal to noise ratio. Ultimately, a comparison between the intensities of the D band and G band, if applicable, would provide a representation of the graphitization within the biochar resulting from differing process parameters, specifically heating rate.

4.6.7. Scanning Electron Microscopy

Scanning electron microscopy (SEM) was conducted using a TESCAN LYRA$_3$ FE-SEM (Fig. 43).
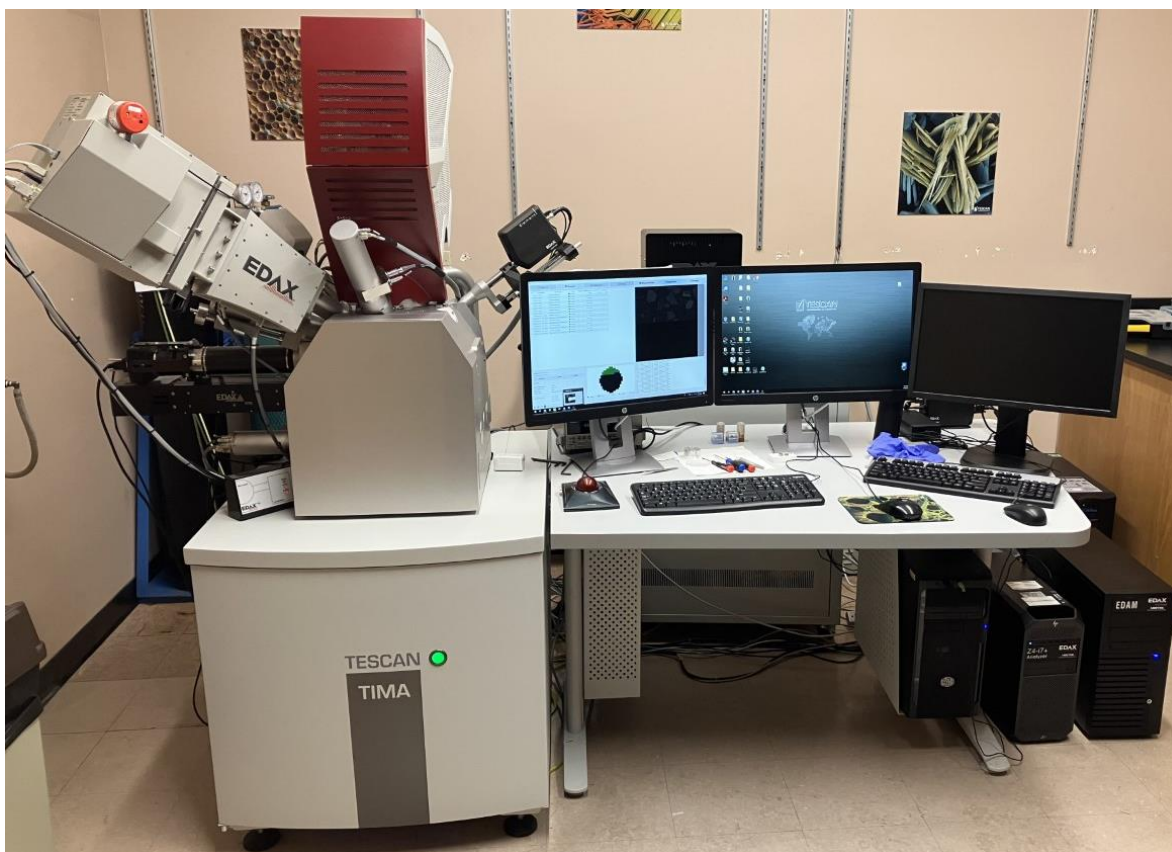
Figure 43: TESCAN LYRA$_3$ FE-SEM.

Samples from the batch and CVAP reactors were prepared for imaging by adhering to specific stands and sputter coated with gold to improve conductivity for imaging in accordance with ASTM B488-18 [100]. The improved conductivity mitigated charge accumulation on the surface and generated higher image quality. Backscatter images were recorded for the batch reactor products to provide visual representations of the structural characteristics of the biochar.

5. Results

5.1. Thermogravimetric Analysis

Weight change data from TGA experimentation of raw hemp feedstock in an inert

atmosphere was recorded as a function of temperature (Fig. 44).
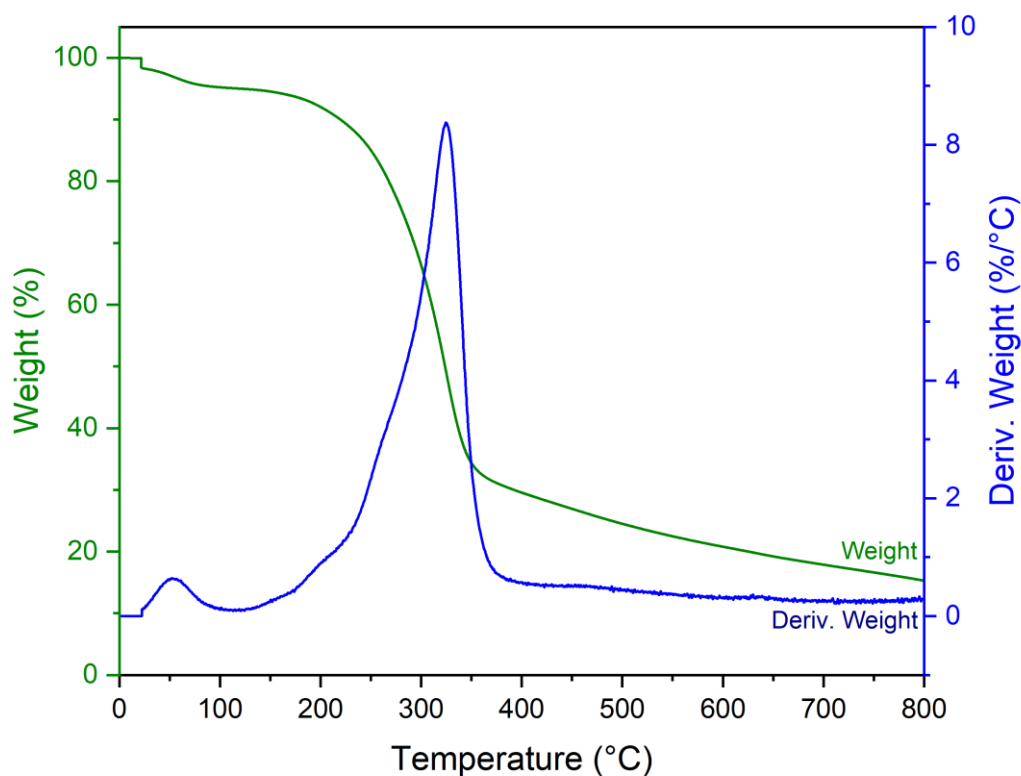
Figure 44: TGA plot (Origin 2023) of raw hemp under inert conditions depicting weight loss (green) and derivative weight loss (blue) as a function of temperature to determine ideal mass yield of 27% at 450°C.

Weight loss, represented with the left axis in green, depicts three distinguishable

decomposition regions. These regions are better represented by the derivative of weight loss, in

the right blue axis. A small magnitude decomposition occurs between 50°C (122°F) and 100°C

(212°F) and represents the loss of moisture and surface contaminants deposited from contact

with the atmosphere. The bulk decompositions of the sample occur between 200°C (392°F) and

350°C (662°F), within the established pyrolysis temperature range. Data furthermore reveals an

expected mass yield of 27% for hemp biochar processed at 450°C (842°F).

Weight change data from TGA experimentation of raw hemp feedstock in an oxidizing

atmosphere was recorded as a function of temperature (Fig. 45).
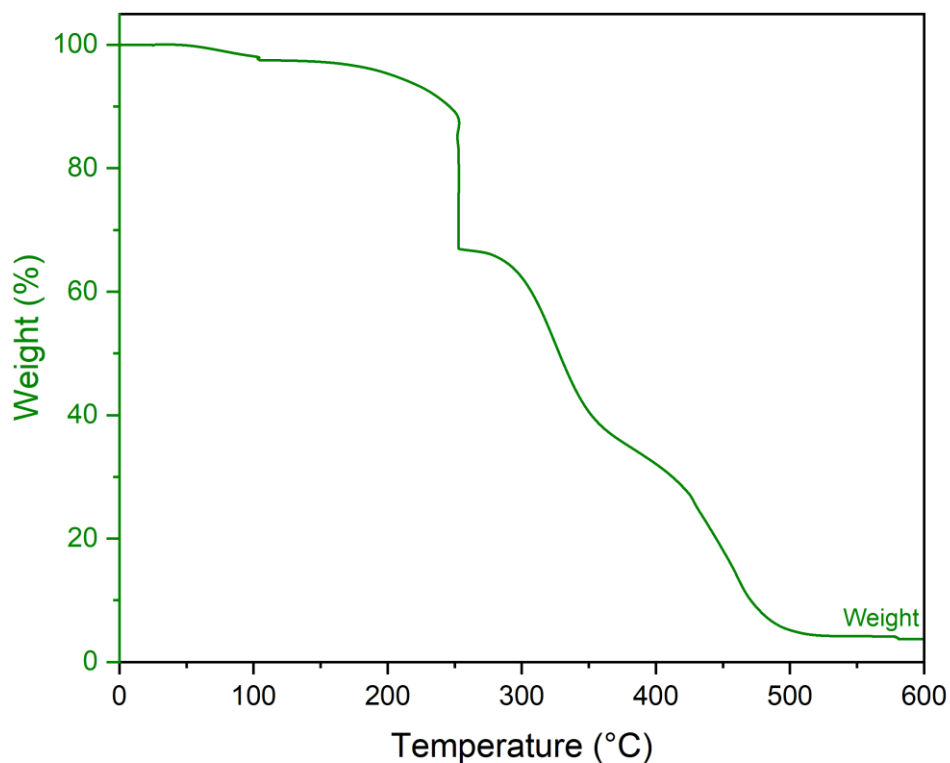
Figure 45: TGA plot (Origin 2023) of raw hemp under oxidizing conditions depicting the weight loss (green) as a function of temperature to determine a feedstock ash content of 3.85%.

The resulting mass from the experiment, 3.85%, represents the ash content present in the

biomass.

5.2. Mass Spectroscopy

Ion currents generated in the secondary electron multiplier by each decomposed species with respect to the sampling time were recorded (Fig. 46). The experimental temperature was displayed on a second axis for reference.
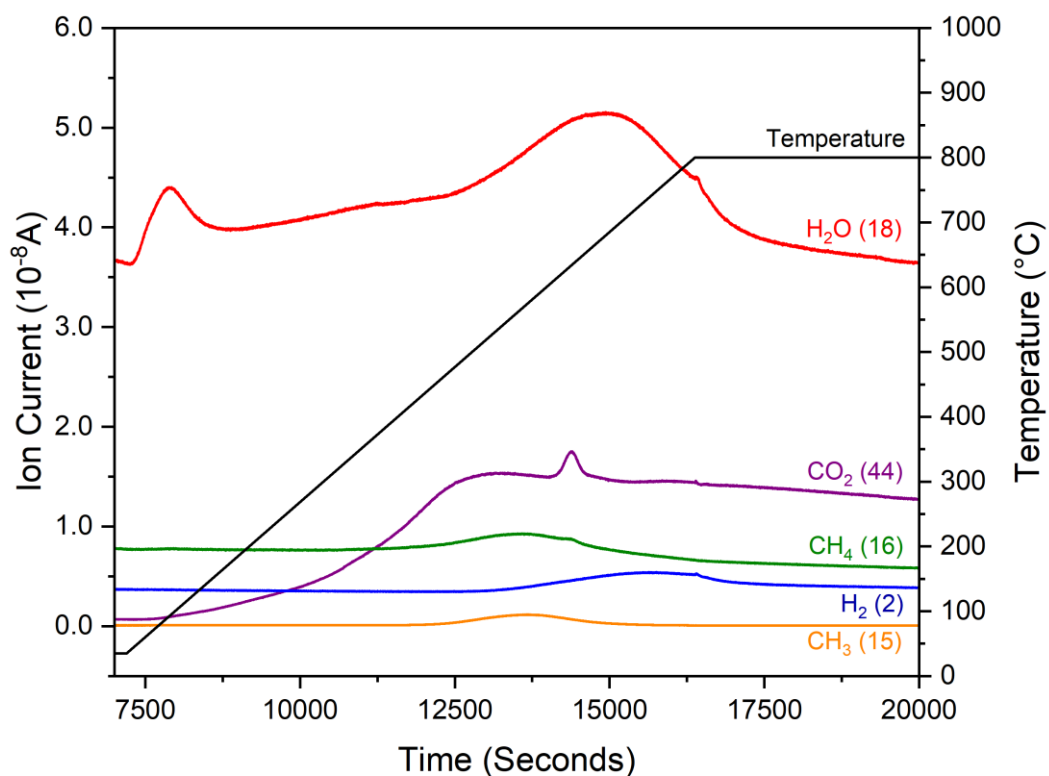
Figure 46: TGA-MS plot (Origin 2023) of batch reactor biochar depicting simultaneous profiles of decomposed gases overlayed with the experimental thermal profile.

Deviations from the baseline represent the magnitude and temperature of each decomposition. Water (H_2O) was shown to constitute two decompositions, at approximately 100°C (212°F) and 700°C (1292°F). The carbon dioxide (CO_2) signal depicted two decompositions as well. The first decomposition occurred at 450°C (842°F) and decreased in

magnitude for the remainder of the experiment. A second decomposition occurred simultaneously at 640°C (1184°F). Additional species were found to decompose: methane (CH_4) at 560°C (1040°F), diatomic hydrogen (H_2) at 725°C (1337°F), and a metastable methyl radical (CH_3) at 560°C (1040°F), possibly formed by the splitting of a heavier hydrocarbon.

5.3. Surface Area and Porosity

BET surface area and porosity measurements using nitrogen and carbon dioxide adsorption were recorded (Table 9) for the three samples analyzed.

Table 9: Batch reactor biochar surface area and porosity adsorption measurements.

Sample	N_2 Adsorption (m^2/g)	Fitting Error (%)	CO_2 Adsorption (m^2/g)	Fitting Error (%)
1	6	7.68	342	0.20
2	7	7.43	354	2.50
3	8	3.75	366	3.52
Std. Dev.	0.9	-----	12.0	-----
Average	6.9	-----	354.0	-----

Nitrogen adsorption experiments yielded an average BET surface area of 6.9m^2/g. The BET method was adapted during carbon dioxide adsorption to determine the surface area of ultra-micro pores. Cryogenic nitrogen is unable to measure this surface area due to diffusional barriers. A custom analysis method was formulated based upon published research, yielding an average surface area of 354.0m^2/g [101].

5.4. Carbon-Hydrogen Ratio

Percentages of carbon, hydrogen, and nitrogen present in the biochar were recorded

(Table 10) for the three samples analyzed.

Table 10: Batch reactor biochar elemental compositions.

Sample	Carbon (%)	Hydrogen (%)	H/C	Nitrogen (%)
1	67.60	2.93	0.0434	1.32
2	68.20	2.93	0.0429	1.28
3	67.50	2.95	0.0437	1.26
Std. Dev. (%)	0.40	0.01	0.0004	0.03
Average (%)	67.77	2.94	0.0433	1.29

The average elemental compositions were: 67.78% carbon, 2.94% hydrogen, and 1.29%

nitrogen. Subtracting the sums of each species and ash content from 100%, the remaining solid

material corresponding to oxygen was estimated to be 24%. Additionally, the average H/C and

O/C ratios were calculated to be 0.0433 and 0.356, respectively. Standard deviations of the

samples were within specifications set by the instrument.

5.5. X-Ray Diffraction

Intensity data collected from the two-theta XRD experiment was recorded and plotted with a 12-point fast Fourier transform (FFT) smoothing function for clarity (Fig. 47).
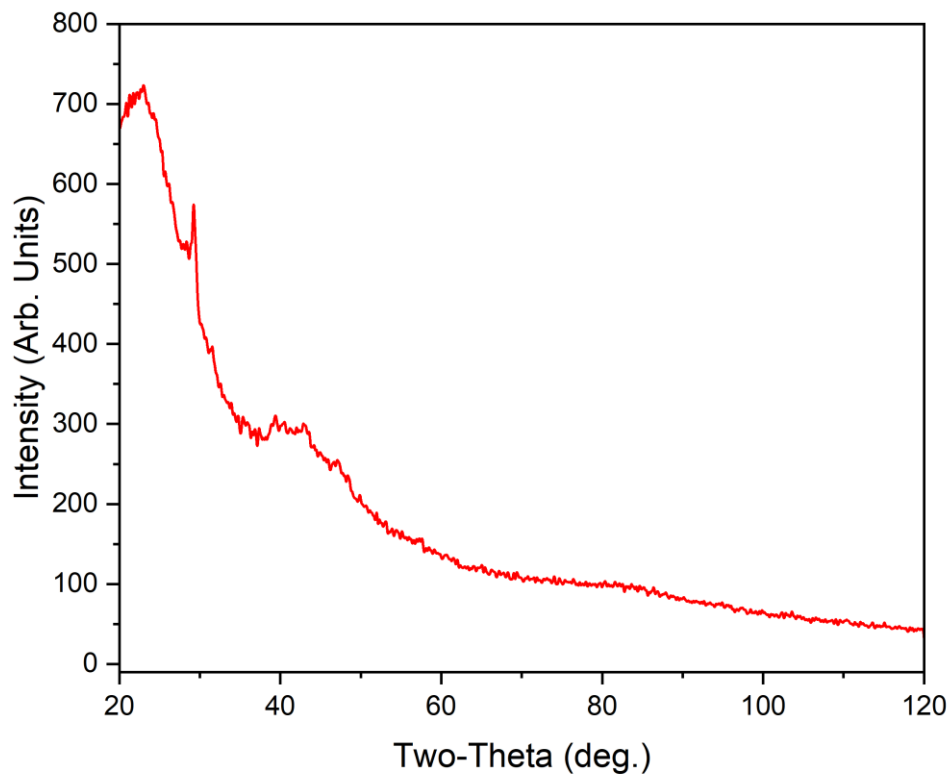
Figure 47: XRD plot (Origin 2023) of batch reactor biochar with 12-point FFT smoothing, depicting amorphous structures and a low magnitude peak at 29.2°.

The diffractogram depicts largely amorphous structures, with a low intensity peak occurring at 29.2°. Additionally, several very low magnitude peaks may appear between 40° and 50°, but were not distinct enough to be definitively distinguished from signal noise.

5.6. Raman Spectroscopy

Intensity data collected from the Raman spectroscopy experiments were recorded and plotted (Fig. 48) for the three samples analyzed.
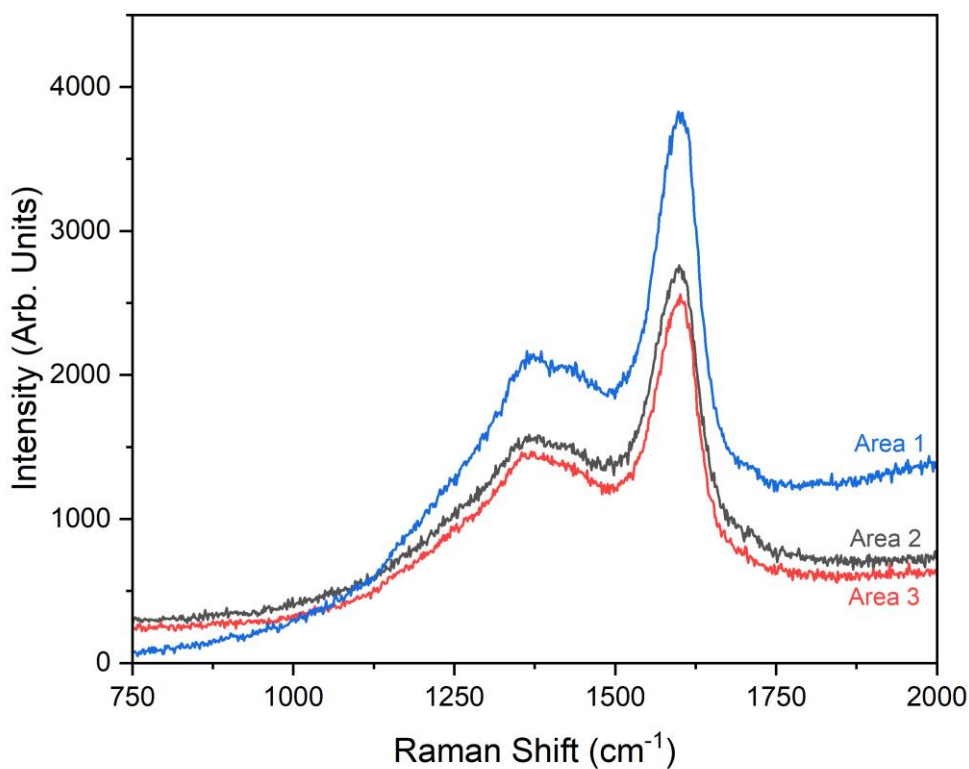
Figure 48: Raman shift plot (Origin 2023) of batch reactor biochar depicting the D band at 1365cm^{-1} and the G band at 1598cm^{-1}.

Raman spectra depicts the two bands occurring at the same wavenumber for the three samples. The D band was located at 1365cm^{-1} and the G band at 1598cm^{-1}. Scans were not continued past 2000cm^{-1} due to an absence of discernible bands.

5.7. Scanning Electron Microscopy

SEM backscatter images (Fig. 49) were captured to serve as a visible representation of the physical characteristics of biochar from the batch pyrolysis reactor.
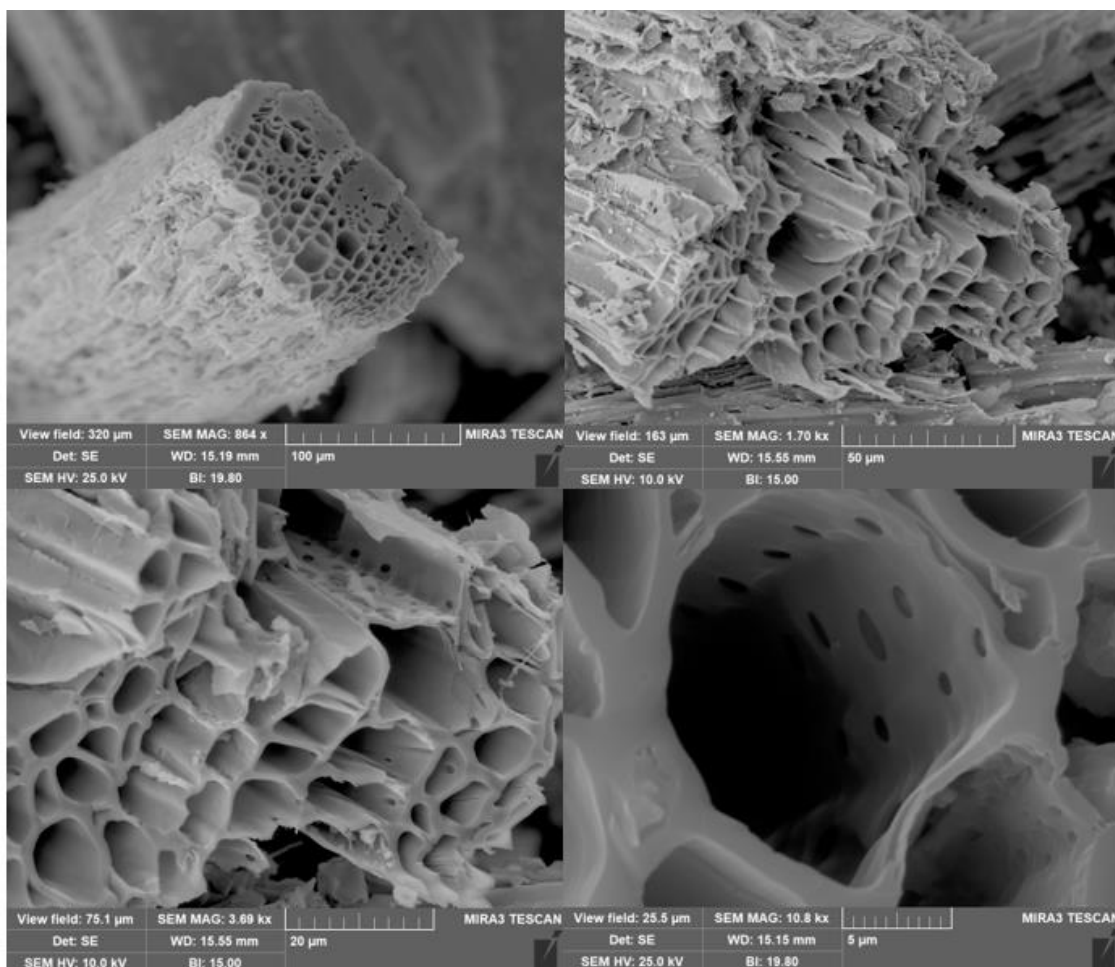
Figure 49: SEM backscatter images of batch biochar depicting retained lignocellulosic structures.

The SEM images were taken at the same sample location with view fields decreasing from 100μm to 5μm. Images show that the honeycomb lignocellulosic structures are retained through pyrolysis. Furthermore, porosity is present on the interior faces of these structures. These pores, formed during pyrolysis, increase the surface area of the solid and create additional sites for adsorption.

6. Discussion

The objective of this study was to develop a novel continuous pyrolysis reactor for mobile delivery. Additionally, this study examined the feasibility of producing scientific biochar in prototype-scale reactors. First, the development of the CVAP reactor will be discussed and compared to the batch reactor. Then, a detailed physicochemical characterization of the batch reactor biochar will be completed to serve as a baseline of comparison for the CVAP reactor products. Finally, an economic analysis will be performed to discuss the monetary feasibility of large-scale scientific biochar production.

6.1. CVAP Reactor Development

The development of the CVAP reactor improved upon the existing batch reactor in several categories. Most significantly, daily production was increased by a factor of 83. Production on the kilogram/pound scale allows for small commercial applications in addition to the laboratory. Potential commercial applications include off-grid biochar production for contaminated soil and water remediation. While larger capacity systems are possible to develop, the size and weight of the CVAP reactor is ideal for deployment with and ATV or small vehicle in areas where large infrastructure is difficult to construct. One such area is the abandoned Elkhorn Mine site in Southwestern Montana [102]. Tailings rich in heavy metals have leached into the groundwater and streams, presenting a health hazard to humans and wildlife in the surrounding areas. The remote location of the site and lack of existing infrastructure creates the need for mobile units to produce remediation materials. Contaminated and remote sites similar to the Elkhorn Mine exist throughout the mountain west, establishing a need for mobile reactors such as the CVAP for remediation. The increase in production also allows for a higher volume of experiments to be performed in the laboratory. In the CHAR laboratory at Montana

Technological University, the limiting step in research is the production of biochar. Utilization

of the CVAP reactor adequately addresses the production needs of the laboratory.

Aside from the production benefits, the CVAP reactor was developed with several

improvements. The design of the syngas handling system facilitates the collection of pure liquid

byproducts for future research projects. Collection of these products is currently not performed

by the batch reactor. The condensation of the byproducts further benefits by strategically

condensing the liquids in easily removable glass traps. While the batch reactor requires

complete disassembly to remove condensed liquids, the traps in the CVAP reactor require the

removal of two, easily accessible fittings. Increases in the syngas plumbing diameter from the

batch reactor serves to mitigate risks of clogging and decreases the gas velocity when entering

the glass traps. Decrease in velocity allows for more time for heat transfer to occur and more

complete condensation. The new syngas handling system was also designed to be modular to

allow for easy removal or modifications for future research. Reactor geometries were also

designed for ease of changing sample. In the batch reactor, several flanged connections require

removal for loading of the furnace. The CVAP reactor is equipped with three doors that are

removed with simple over-center latches. A final usability feature is the digital interface to guide

the operator through production. The HMI is a touch screen display that presents the operating

steps, prompts the user to enter setpoints, and allows for in-situ process monitoring. When

operating the batch furnace, several valves, setpoints, and power switches are required to

manipulated on a timer. The process automation of the CVAP reactor requires three setpoints to

be entered by the user and a single button to be pressed to operate the system. This improvement

allows the operator to load and start the CVAP reactor in around 10 min. A final benefit to the

automation scheme is the added safety considerations. The batch reactor is equipped with an

emergency shutdown button, but not all equipment is able to respond to the command. On the CVAP reactor, depressing the emergency button is able to shut down every component, mitigating the need for the operator to reach inside the polycarbonate enclosure to stop the process. Overall, the CVAP reactor significantly improves upon the batch reactor in capacity, usability, and safety.

6.2.   Biochar Characterization

A physicochemical characterization of the biochar produced from the batch reactor was performed to generate a reference for comparison with the CVAP reactor products. Thermal degradation behavior was examined using thermogravimetric analysis and mass spectroscopy. TGA data (Fig. 44) illustrates distinct mass loss regions, represented by changes in the slope of the derivative weight curve. An initial mass loss occurs at 100°C (212°F), representing the decomposition of surface moisture. The magnitude of this decomposition validates the omission of specific drying procedures for the biomass. While high-moisture content biomass is still suitable for pyrolysis, residual water increases the energy required during the reaction. The mass loss due to moisture of approximately 5% falls below the recommended limit of 10% [103]. Increase in temperature beyond 100°C (212°F) causes a decrease in hemicellulose and cellulose content, then a slow decomposition of lignin [104]. The next mass loss region, occurring between 200°C (392°F) and 240°C (464°F) corresponds to the decomposition of hemicellulose (Eqn. 5), which is confirmed in existing literature [105].

$$(C_5H_{10}O_5)_n + Heat \ \rightarrow \ humins \tag{5}$$
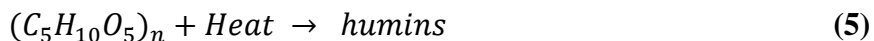
Maximum mass loss in the hemp feedstock, resulting from the decomposition of cellulose (Eqn. 6), occurs between 240°C (464°F) and 350°C (662°F), furthermore confirming literature [105].

$$(C_6H_{10}O_5)_n + Heat \rightarrow humins \tag{6}$$
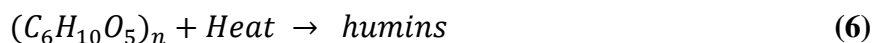
The final insight from TGA experimentation of the feedstock under inert conditions is the ideal mass yield at a given pyrolysis temperature. Small sample size in the TGA allows for mass yield data from the experiment to be viewed as ideal. Data from the plot indicates that the expected mass yield for pyrolysis at 450°C (842°F) is 27%. Pyrolysis experiments conducted with the batch reactor operating at the same conditions as the TGA result in mass yields averaging 30%. The 3% mass difference is within an accepted range given the measurement precision available to consider similar reaction completeness. TGA experimentation of the hemp feedstock under oxidizing atmospheric conditions (Fig. 45) yielded an ash composition of 3.85%. Ash content in biomass results from the presence of inorganic macronutrients and micronutrients absorbed during growth [106]. Quantification of the ash content is integral, as the level of inorganics is variable based on the specific growth environment. Furthermore, inorganic molecules may have impacts on the adsorption behavior of the biochar, depending upon the application [107]. While not included in the scope of this study, additional testing, such as inductively coupled plasma optical emission spectroscopy (ICP-OES) or energy dispersive X-ray spectroscopy (EDXS), should be performed to characterize the inorganics present. The removal of inorganics before may also be performed before pyrolysis using an acid wash on the feedstock.

Thermogravimetric analysis with mass spectroscopy (TGA-MS) experiments were performed to determine the completion of the pyrolysis reaction and approximate the surface chemistry of the biochar. TGA-MS records the decomposition of gas species as a function of temperature. The temperature of these decomposition allows for an approximation of the surface chemistry. Surface chemistry is integral to the adsorption capacity and selectivity of the biochar [108]. Additionally, chemical surface treatments such as activation are dependent upon the

available functional groups. TGA-MS spectra (Fig. 46) indicates that the batch reactor indeed reaches the 450°C (842°F) setpoint as no high-magnitude peaks occur prior to the process temperature. The first water (18) decomposition occurs at 100°C (212°F), corresponding to absorbed water molecules from the atmosphere. Changes in the DTA curve at this temperature and the known boiling point of water further support this. Gradually increasing magnitudes of the water (18) signal between 300°C (572°F) and 500°C (932°F) are attributed to decompositions of complex organic molecules and acids such as carboxylic groups [109]. The final water (18) peak at 700°C (1292°F) indicates the formation and loss of molecules due to a strong deoxygenation process [110]. During this decomposition, more stable oxygen and hydrogen containing groups, such as phenols are lost [111]. The first increase in magnitude for carbon dioxide (44) occurs gradually between 100°C (212°F) and 400°C (752°F), representing the decomposition of organics and surface functionalities to carbon dioxide [110]. Beyond 400°C (752°F), the formation of carbon dioxide decreases, corresponding to the loss of oxygen in the biochar as a function of temperature. At 640°C (1188°F), a distinct carbon dioxide peak is observed, corresponding to the decomposition range for lactone groups [112]. Additional species: methane, hydrogen, and methyl radical groups show small, localized decompositions, but the small magnitudes compared to other species limit the need for further analysis.

Brunauer-Emmett-Teller (BET) theory was applied to determine the surface area and porosity characteristics of the biochar. The surface area and porosity are related to numerous biochar properties, such as the adsorption capacity and selectivity. During adsorption, macropores are responsible for the diffusion of substances, mesopores behave as mass transfer channels, and micropores provide the trapping space [113]. The surface area and diameter of pores serve as an indication of the pyrolysis conditions [114]. Nitrogen adsorption at 77K results

(Table 9) yield an average surface area of 6.9m^2/g. Carbon dioxide adsorption at 273K results

(Table 10) yield an average microporous surface area of 354m^2/g. The BET data supports

previously published experimental results [114]. The greater carbon dioxide surface area

compared to nitrogen indicates a slow and uniform release of volatile compounds due to the slow

heating rate of 10°C/min. Increased heating rates accelerate the release of byproducts,

generating larger pores. Furthermore, the small pore diameters are indicative of low process

temperatures. Biochar produced at temperatures below 600°C (1112°F) retain significant surface

functional groups, preventing the formation of larger pore sizes [114]. During future

comparisons with CVAP reactor biochar, the continuous nature of the system is postulated to

produce biochar with: higher nitrogen adsorption surface area, lower carbon dioxide adsorption

surface area, and overall larger pore diameters.

An elemental analysis was conducted on the biochar to determine the percentages of

carbon, hydrogen, and nitrogen present after pyrolysis. Experimental results (Table 11) yield

average compositions of 68% carbon, 3% hydrogen, and 1% nitrogen, confirming previously

published literature [115]. The H/C ratio was also calculated to be 0.0433, representing the

degree of carbonization [116]. Low H/C ratios in biochar result from significant thermal

alteration during pyrolysis due to the greater loss of hydrogen and nitrogen, relative to carbon.

The greater degree of carbonization also indicates an affinity towards aromaticity, which

suggests that this biochar is ideal for non-aqueous applications [115]. By subtracting the values

of carbon, hydrogen, nitrogen, and ash content from 100%, the oxygen content was

approximated to be 24%, resulting in an O/C ratio of 0.356. Comparing these values to those

published in literature, the batch reactor biochar contained relatively low oxygen content [115].

The oxygen content and O/C ratio are indicative of the hydrophilic nature of the surface as they

represent the presence of polar-group content derived from carbohydrates. Low O/C ratio indicates that the batch reactor biochar may not be as suitable for aqueous applications. However, further research may explore the optimization of parameters to increase the O/C ratio to increase the hydrophilicity.

X-ray diffraction was performed to determine the crystalline structure and graphitization of the biochar. The diffractogram (Fig. 47) depicts broad peaks throughout the scan, representing predominately amorphous structures in the solid, with a distinct, sharp peak at $2\theta = 29.2°$. According to the JCPDS pattern 96–901–6706, strong orientation along the (104) plane is consistent with the presence of calcite (Hexagonal) [117]. Calcite, an inorganic compound, was most likely retained from the raw hemp feedstock and resulted from the growth environment. Further confirmation of the presence of inorganics in the biochar is given by the TGA ash content (Fig. 45) and previous studies [118]. Additional low-magnitude peaks are possibly present between $2\theta = 40°$ and $2\theta = 50°$. However, these peaks were only discernible after 12-point FFT smoothing was performed, indicating the possibility of retained noise in the signal. Given previously published data, these peaks may correspond to trace amounts of carbonates (potassium, magnesium, etc.), but additional compositional analyses should be performed to confirm [115].

Raman spectroscopy was performed on the biochar to identify the alterations to the carbon structure. Raman spectra (Fig. 48) depict the presence of two bands at $1365cm^{-1}$ and $1598cm^{-1}$, confirming published literature [119]. The defect (D) band, occurring at $1365cm^{-1}$, is related to the defects associated with the breaking of the hexagonal symmetry of the carbon atoms in the graphene sheets [119]. The graphite (G) band, occurring at $1598cm^{-1}$, is related to the presence of organized sp2 domains [120]. Relationships between the intensities of the D and

G bands provide an estimate of the crystallite size and number of defects in the biochar [121]. Additional peaks may also be seen for highly disordered materials [122]. Absence of these peaks in the biochar analyzed indicates that the solid contains less disordered structures. Furthermore, a comparison between the intensities of the bands indicates that the ordered carbon clusters in the feedstock grew and a majority formed graphite-like disordered structures, instead of being retained. Future analyses with the CVAP reactor biochar will be able to correlate the relative band intensities to the process temperature. Increased process temperatures will decrease the difference in magnitude between the bands, identifying an inconsistency during the operation [123].

6.3. Economic Analysis

The final analysis was conducted to determine the economic feasibility of scaling up the production quantity of scientific biochar. Several assumptions were made to perform the analysis. First, the power consumptions of each system were difficult to quantify, so it was assumed that each system component operated with the maximum rated power. Next, biochar was assumed to be processed at 450°C (842°F) with a residence time of one hour. With these operating conditions, the batch reactor produces 12g (0.53oz) of biochar and the CVAP reactor produces 1kg(2.2lb) during an eight-hour workday. The batch reactor also operates under an inert atmosphere of argon. The 2023 price of industrial-grade argon sourced from General Distributing (Butte, MT) was $130 per tank, which produces 48g (1.7oz) of biochar [124]. A value of $0.12/kWh of electricity was also assumed from the 2023 standard commercial rates, given by NorthWestern Energy (Butte, MT) [125]. Total fixed cost for the batch reactor was calculated to be $27,000 from previous research documentation at Montana Technological University and variable costs of inert gas and electricity were calculated to be $2,741/kg of

biochar. Total fixed cost for the CVAP reactor was calculated to be $56,000 (Appx. A) and the variable cost of electricity was calculated to be $12/kg of biochar. The fixed and variable costs were used to generate linear equations for each reactor to determine the operational breakthrough point of the CVAP reactor (Fig. 50).
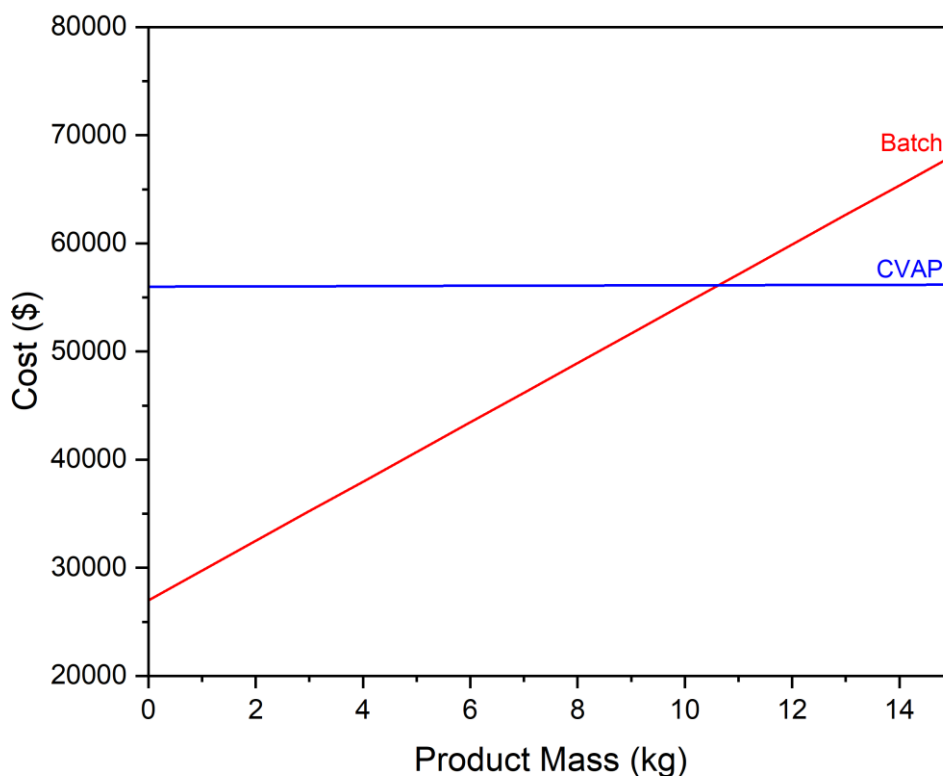
Figure 50: Cost analysis plot (Origin 2023) of the total cost of biochar production via the batch and CVAP reactors, depicting the break-even mass of 10.5kg (23.1lb).

Graphing the total costs of the systems shows that that the CVAP reactor requires nearly double the initial capital investment. The economic advantage of the CVAP reactor is shown with the variable costs. Variable costs of operating the batch reactor are much higher due to the use of the inert purge gas. The total cost of the batch reactor becomes uneconomical after 10.5kg

(23.1lb) of biochar are produced, or 10.5 days of operation. While the batch reactor may be suitable for small lab-scale production, biochar demand on the kilogram/pound basis can be best served by a system sized similarly to the CVAP reactor. Additionally, this analysis neglected the cost of paying an operator to produce the biochar. The increased capacity of the CVAP reactor causes biochar to be produced in less time, which results in fewer billable hours from an operator. Overall, the development and deployment of the CVAP reactor is economically justified when compared to the batch reactor.

7. Conclusions

The CVAP reactor was designed and fabricated to increase the production capacity of scientific biochar, decrease reliance on consumables, and facilitate mobile delivery. Biochar was produced at 450°C (842°F) with a 60-minute residence time from dried and shredded hemp stalks using the batch reactor. The produced biochar was characterized using thermogravimetric analysis, mass spectroscopy, surface area and porosity, carbon-hydrogen ratio, x-ray diffraction, Raman spectroscopy, and scanning electron microscopy analysis tools. The characterization results were analyzed to provide a reference for future comparison with CVAP reactor products. The following conclusions were formulated:

- Initial testing of the CVAP reactor automation scheme indicates a substantial decrease in workload for the operator. The CVAP reactor requires three user inputs and one button to be pressed at the same time, while the batch reactor requires several actions over 30min.

- Syngas handling system upgrades, glass cold traps and increased tubing diameters, allow for liquid byproduct recovery and decreased frequency of preventative maintenance.

- Automation and safety infrastructure including status lights, PLC, and polycarbonate enclosure increase the safety of the operator. Depression of the emergency stop buttons place all components into a safe configuration. This feature was not available for all system components in the batch reactor.

- The geometry of the CVAP reactor facilitates more ease of loading and unloading of samples with minimal disassembly of the infrastructure compared to the batch reactor.

- Utilization of induction for heating decreases the time required for the process temperature to be reached, facilitating the production of more biochar during a standard work day.

- Placement of the inductive susceptor inside of the reactor tube increases the heating efficiency of the process and eliminates the convective losses present in the externally-heated batch reactor.

- Raw hemp feedstock currently utilized for biochar production contains an ash content of less than 5%, matching literature. Additionally, ash contents below this threshold produce more efficient biochar for adsorption.

- The batch reactor produces a high quality of biochar. Mass yields in the reactor at 450°C (842°F) less than 5% different than the theoretical value from TGA experimentation. Furthermore, other characterization methods yielded results confirming literature including large microporosity and high carbon content.

- There exists a significant economic benefit to operating the CVAP reactor. The CVAP reactor decreases the per kilogram variable production cost by a factor of 21. The cost break-through point for the CVAP reactor occurs after 10.5kg (23.1lb) of biochar are produced.

- The rate of daily production is increased by a factor of 83, resulting in more biochar for experimental or application usage. An increased production rate further adds to the economic benefit, as operator wages to produce large quantities of biochar are reduced.

8. Recommendations

- Due to production delays with the induction heating system, the CVAP reactor was able to be fully completed. The following tasks should be performed to complete the reactor:
  - o Install the induction heating system according to the provided wiring schematic (Appx. E).
  - o Ensure that the raw feedstock residence times reflect the setpoint using dyed tracer particles and hand timing.
  - o Apply phenolic graphite adhesive to the auger segments and fire to cure.
- Perform the characterization experiments outlined in Section 4.6 on the products from the CVAP reactor. Compare the analysis results and adjust the operational settings in the CVAP reactor accordingly.
  - o Additionally, the ash content from the hemp feedstock should be characterized using inductively coupled plasma optical emission spectroscopy (ICP-OES) or energy dispersive X-ray spectroscopy (EDXS).
- Design post-processing infrastructure to convert pyrolysis waste streams into usable products.
- Initial design and economic analyses indicate both time and cost savings for bulk biochar production. Explore reactor designs to further increase the production capacity.

9. References

[1] Jeguirim, M., Limousy, L. (2019). Char production technology. In Char and carbon materials derived from biomass: Production, characterization and applications (pp. 39–68). Elsevier.

[2] History. Biochar Now. (2019, December 17). Retrieved January 18, 2023, from https://biocharnow.com/history/.

[3] Saukko, P. J., Siegel, J. A., & Houck, M. M. (Eds.). (2013). Identification and Comparison. In Encyclopedia of Forensic Sciences (2nd ed., Vol. 2, pp. 129–137). Academic Press.

[4] Tan, S., et al. (2023). Utilization of current pyrolysis technology to convert biomass and manure waste into biochar for soil remediation: A Review. *Science of The Total Environment*, *864*, 1–13. https://doi.org/10.1016/j.scitotenv.2022.160990.

[5] Yan, S., Chen, H., Zhu, H., Lin, Z., Wu, G., Gao, W., Zhang, H., Hu, X., Zhang, J., Zhang, S., Zhang, S., & Wu, Y. (2023). Enhanced adsorption of bio-oil on activated biochar in slurry fuels and the adsorption selectivity. *Fuel*, *338*, 127224. https://doi.org/10.1016/j.fuel.2022.127224.

[6] National Academies of Sciences, Engineering, and Medicine 2022. New Directions for Chemical Engineering. Washington, DC: The National Academies Press. https://doi.org/10.17226/26342.

[7] Yoder, J., Galinato, S., Granatstein, D., & Garcia-Pérez, M. (2011). Economic tradeoff between biochar and bio-oil production via pyrolysis. *Biomass and Bioenergy*, *35*(5), 1851–1862. https://doi.org/10.1016/j.biombioe.2011.01.026.

[8] Yaashikaa, P. R., Kumar, P. S., Varjani, S., & Saravanan, A. (2020). A critical review on the biochar production techniques, characterization, stability and applications for circular bioeconomy. *Biotechnology Reports*, *28*. https://doi.org/10.1016/j.btre.2020.e00570

[9] Cremers, M., et al. (2015). *Status overview of torrefaction technologies*. IEA Bioenergy.

[10] Binder, M., et al. (2018). *Hydrogen from biomass gasification*. IEA Bioenergy.

[11] Poulin, B. (2018). *Biomass Gasification*. Aries Clean Energy.

[12] Taherzadeh, M. J., Bolton, K., Wong, J. P., & Pandey, A. (2019). Gasification Technologies and Their Energy Potentials. In *Sustainable resource recovery and zero waste approaches* (pp. 139–206). essay, Elsevier.

[13] Lewandowski, Witold & Ryms, Michał & Kosakowski, Wojciech. (2020). Thermal Biomass Conversion: A Review. Processes. 8. 516. 10.3390/pr8050516.

[14] Nasrollahzadeh, M. (2021). Lignin chemistry and valorization. In *Biopolymer-based metal nanoparticle chemistry for sustainable applications* (Vol. 1, pp. 145–183). essay, Elsevier.

[15] Yoganandham, S., Sathyamoorthy, G., & Renuka, R. (2020). Emerging extraction techniques: Hydrothermal processing. In *Sustainable seaweed technologies: Cultivation, biorefinery and applications* (pp. 191–205). essay, ELSEVIER.

[16] USDA Agricultural Research Service. (2021, September 10). *What is Pyrolysis?* Biomass Pyrolysis Research. Retrieved January 30, 2023, from https://www.ars.usda.gov/northeast-area/wyndmoor-pa/eastern-regional-research-center/docs/biomass-pyrolysis-research-1/what-is-pyrolysis/.

[17] Zafar, S. (2009, February 1). *Biomass pyrolysis*. AltEnergyMag. Retrieved January 30, 2023, from https://www.altenergymag.com/article/2009/02/biomass-pyrolysis/502/

[18] Clifford, C. (2020). 5.1 Biomass Pyrolysis | *EGEE 439: Alternative Fuels from Biomass Sources*. Retrieved January 30, 2023, from https://www.e-education.psu.edu/egee439/node/537.

[19] Suib, S. L. (2013). Chapter 8 - An Introduction to Pyrolysis and Catalytic Pyrolysis: Versatile Techniques for Biomass Conversion. In *New and future developments in catalysis catalytic biomass conversion* (pp. 173–208). essay, Elsevier.

[20] Yadav, K., & Jagadevan, S. (2020). Influence of Process Parameters on Synthesis of Biochar by Pyrolysis of Biomass: An Alternative Source of Energy. *Recent Advances in Pyrolysis*. doi: 10.5772/intechopen.88204.

[21] Zhang, J., Liu, J., & Liu, R. (2015). Effects of pyrolysis temperature and heating time on biochar obtained from the pyrolysis of straw and lignosulfonate. *Bioresource Technology*, *176*, 288–291. https://doi.org/10.1016/j.biortech.2014.11.011.

[22] Lienhard, J. H., & Lienhard, J. H. (2020). *A Heat Transfer Textbook* (5th ed.). Dover Publications.

[23] Wang, Z., et al. (2019). Effects of residence time on characteristics of biochars prepared via co-pyrolysis of sewage sludge and cotton stalks. *Journal of Analytical and Applied Pyrolysis*, *142*, 104659. https://doi.org/10.1016/j.jaap.2019.104659.

[24] Salehi, E., Abedi, J., & Harding, T. (2009). Bio-oil from Sawdust: Pyrolysis of Sawdust in a Fixed-Bed System. *Energy & Fuels*, *23*(7), 3767–3772. https://doi.org/10.1021/ef900112b.

[25] Kan, T., Strezov, V., & Evans, T. J. (2016). Lignocellulosic biomass pyrolysis: A review of product properties and effects of pyrolysis parameters. *Renewable and Sustainable Energy Reviews*, *57*, 1126–1140. https://doi.org/10.1016/j.rser.2015.12.185.

[26] Mohan, D., Pittman, C. U., & Steele, P. H. (2006). Pyrolysis of wood/biomass for bio-oil: A critical review. *Energy & Fuels*, *20*(3), 848–889. https://doi.org/10.1021/ef0502397

[27] Tomczyk, A., Sokołowska, Z., & Boguta, P. (2020). Biochar physicochemical properties: Pyrolysis temperature and feedstock kind effects. *Reviews in Environmental Science and Bio/Technology*, *19*(1), 191–215. https://doi.org/10.1007/s11157-020-09523-3.

[28] Kloss, S., Zehetner, F., Dellantonio, A., Hamid, R., Ottner, F., Liedtke, V., Schwanninger, M., Gerzabek, M. H., & Soja, G. (2012). Characterization of slow pyrolysis biochars: Effects of feedstocks and pyrolysis temperature on biochar properties. *Journal of Environmental Quality*, *41*(4), 990–1000. https://doi.org/10.2134/jeq2011.0070.

[29] Shariff, A., Aziz, N. S. M., Saleh, N. M., & Ruzali, N. S. I. (2016). The effect of feedstock type and slow pyrolysis temperature on biochar yield from coconut wastes. *International Journal of Chemical and Molecular Engineering*, *10*(12), 1410-1414.

[30] Ahmad, M., Lee, S. S., Dou, X., Mohan, D., Sung, J. K., Yang, J. E., & Ok, Y. S. (2012). Effects of pyrolysis temperature on soybean stover-and peanut shell-derived biochar properties and TCE adsorption in water. *Bioresource technology*, *118*, 536-544.

[31] Ambaye, T.G., Vaccari, M., van Hullebusch, E.D. *et al.* (2021). Mechanisms and adsorption capacities of biochar for the removal of organic and inorganic pollutants from industrial wastewater. *Int. J. Environ. Sci. Technol.* 18, 3273–3294. https://doi.org/10.1007/s13762-020-03060-w.

[32] Praveen, S., Jegan, J., Bhagavathi Pushpa, T., Gokulan, R., & Bulgariu, L. (2022). Biochar for removal of dyes in contaminated water: An overview. *Biochar*, *4*(1). https://doi.org/10.1007/s42773-022-00131-8.

[33] Oliveira, F. R., Patel, A. K., Jaisi, D. P., Adhikari, S., Lu, H., & Khanal, S. K. (2017). Environmental application of biochar: Current status and Perspectives. *Bioresource Technology*, *246*, 110–122. https://doi.org/10.1016/j.biortech.2017.08.122.

[34] Kumar, A., Kumar, A., Sharma, G., Naushad, M., Stadler, F. J., Ghfar, A. A., ... & Saini, R. V. (2017). Sustainable nano-hybrids of magnetic biochar supported g-C3N4/FeVO4 for solar powered degradation of noxious pollutants-Synergism of adsorption, photocatalysis & photo-ozonation. *Journal of Cleaner Production*, *165*, 431-451.

[35] Wang, S., Gao, B., Zimmerman, A. R., Li, Y., Ma, L., Harris, W. G., & Migliaccio, K. W. (2015). Removal of arsenic by magnetic biochar prepared from pinewood and natural hematite. *Bioresource technology*, *175*, 391-395.

[36] Qiu, Y., Zheng, Z., Zhou, Z., & Sheng, G. D. (2009). Effectiveness and mechanisms of dye adsorption on a straw-based biochar. *Bioresource technology*, *100*(21), 5348-5351.

[37] Rizwan, M., Ali, S., Qayyum, M. F., Ibrahim, M., Zia-ur-Rehman, M., Abbas, T., & Ok, Y. S. (2016). Mechanisms of biochar-mediated alleviation of toxicity of trace elements in plants: a critical review. *Environmental Science and Pollution Research*, *23*, 2230-2248.

[38] El-Shafey, E. I. (2010). Removal of Zn (II) and Hg (II) from aqueous solution on a carbonaceous sorbent chemically prepared from rice husk. *Journal of hazardous materials*, *175*(1-3), 319-327.

[39] Trakal, L., Veselská, V., Šafařík, I., Vítková, M., Číhalová, S., & Komárek, M. (2016). Lead and cadmium sorption mechanisms on magnetically modified biochars. *Bioresource technology*, *203*, 318-324.

[40] Puga, A. P., Abreu, C., Melo, L. C. A., & Beesley, L. (2015). Biochar application to a contaminated soil reduces the availability and plant uptake of zinc, lead and cadmium. *Journal of environmental management*, *159*, 86-93.

[41] Mohan, D., & Pittman Jr, C. U. (2007). Arsenic removal from water/wastewater using adsorbents—a critical review. *Journal of hazardous materials*, *142*(1-2), 1-53.

[42] Cao, X., Ma, L., Gao, B., & Harris, W. (2009). Dairy-manure derived biochar effectively sorbs lead and atrazine. *Environmental science & technology*, *43*(9), 3285-3291.

[43] Zhang, X., Wang, H., He, L., Lu, K., Sarmah, A., Li, J., ... & Huang, H. (2013). Using biochar for remediation of soils contaminated with heavy metals and organic pollutants. *Environmental Science and Pollution Research*, *20*, 8472-8483.

[44] Keiluweit, M., Nico, P. S., Johnson, M. G., & Kleber, M. (2010). Dynamic molecular structure of plant biomass-derived black carbon (biochar). *Environmental science & technology*, *44*(4), 1247-1253.

[45] Kasozi, G. N., Zimmerman, A. R., Nkedi-Kizza, P., & Gao, B. (2010). Catechol and humic acid sorption onto a range of laboratory-produced black carbons (biochars). *Environmental science & technology*, *44*(16), 6189-6195.

[46] Inyang, M., Gao, B., Zimmerman, A., Zhang, M., & Chen, H. (2014). Synthesis, characterization, and dye sorption ability of carbon nanotube–biochar nanocomposites. *Chemical Engineering Journal*, *236*, 39-46.

[47] Spokas, K. A. (2010). Review of the stability of biochar in soils: predictability of O: C molar ratios. *Carbon management*, *1*(2), 289-303.

[48] Sun, Y., Gao, B., Yao, Y., Fang, J., Zhang, M., Zhou, Y., ... & Yang, L. (2014). Effects of feedstock type, production method, and pyrolysis temperature on biochar and hydrochar properties. *Chemical engineering journal*, *240*, 574-578.

[49] Chen, B., Chen, Z., & Lv, S. (2011). A novel magnetic biochar efficiently sorbs organic pollutants and phosphate. *Bioresource technology*, *102*(2), 716-723.

[50] Panwar, N.L., Pawar, A. & Salvi, B.L. (2019). Comprehensive review on production and utilization of biochar. *SN Appl. Sci.* **1**, 168. https://doi.org/10.1007/s42452-019-0172-6.

[51] Jelinek H (1989) Pyrolysis system. U.S. Patent No. 4,840,129. 20 Jun. 1989.

https://www.google.com/patents/US4840129. Accessed 18 Feb. 2023.

[52] Roberts, K. G., Gloy, B. A., Joseph, S., Scott, N. R., & Lehmann, J. (2010). Life cycle

assessment of biochar systems: estimating the energetic, economic, and climate change

potential. *Environmental science & technology*, *44*(2), 827-833.

[53] Babler, M. U., Phounglamcheik, A., Amovic, M., Ljunggren, R., & Engvall, K. (2017).

Modeling and pilot plant runs of slow biomass pyrolysis in a rotary kiln. *Applied energy*,

207, 123-133.

[54] Ogawa, M., Okimori, Y., & Takahashi, F. (2006). Carbon sequestration by carbonization of

biomass and forestation: three case studies. *Mitigation and adaptation strategies for global

change*, *11*, 429-444.

[55] Schimmelpfennig, S., & Glaser, B. (2012). One step forward toward characterization: some

important material properties to distinguish biochars. *Journal of environmental quality*,

41(4), 1001-1013.

[56] Agirre, I., Griessacher, T., Rösler, G., & Antrekowitsch, J. (2013). Production of charcoal as

an alternative reducing agent from agricultural residues using a semi-continuous semi-pilot

scale pyrolysis screw reactor. *Fuel Processing Technology*, *106*, 114–121.

https://doi.org/10.1016/j.fuproc.2012.07.010.

[57] Giles, H. F., Wagner, J. R., & Mount, E. M. (2014). 33 - Feed Systems. In *Extrusion: The

definitive processing guide and handbook* (2nd ed., pp. 377–397). essay, William Andrew is

an imprint of Elsevier.

[58] Agirre, I., Griessacher, T., Rösler, G., & Antrekowitsch, J. (2013). Production of charcoal as an alternative reducing agent from agricultural residues using a semi-continuous semi-pilot scale pyrolysis screw reactor. *Fuel Processing Technology*, *106*, 114-121.

[59] Ferreira, S. D., Manera, C., Silvestre, W. P., Pauletti, G. F., Altafini, C. R., & Godinho, M. (2019). Use of biochar produced from elephant grass by pyrolysis in a screw reactor as a soil amendment. *Waste and Biomass Valorization*, *10*, 3089-3100.

[60] *Coherent: Global leader in materials, networking, and lasers*. Coherent Inc. (2023). Retrieved February 1, 2023, from https://www.coherent.com/.

[61] Zinn, S., & Semiatin, S. L. (1997). *Elements of induction heating: Design, control, and applications*. ASM International.

[62] Industrial Quick Search. (2023). *Industrial Quick Search*. Graphite Machining. Retrieved April 13, 2023, from https://www.iqsdirectory.com/articles/graphite-machining.html.

[63] Handbook, D. F. (1993). Material Science. *Volume*, *2*, 72.

[64] Gulbransen, E. A., Andrew, K. F., & Brassart, F. A. (1963). The oxidation of graphite at temperatures of 600 to 1500 C and at pressures of 2 to 76 torr of oxygen. *Journal of the Electrochemical Society*, *110*(6), 476.

[65] Muffin Group. (2020, March 25). *Cold traps main page*. KGW. Retrieved March 5, 2023, from https://kgw-isotherm.com/cold-traps-main-page/.

[66] Flexicon Corporation. (n.d.). *Bulk Handling Equipment & Systems*. Hemp. Retrieved March 5, 2023, from https://www.flexicon.com/Materials-Handled/Hemp.html

[67] Strollo, B. S. (n.d.). *AR-12 - molded EDM graphite*. Ohio Carbon Blank. Retrieved March 5, 2023, from

https://www.ohiocarbonblank.com/index.php?file=graphitematerial_detail&url=ar-12.

[68] *Calculating Yield & tensile strength*. Portland Bolt - Anchor Bolt and Construction Fastener

Manufacturer. (2023, January 27). Retrieved March 5, 2023, from

https://www.portlandbolt.com/technical/faqs/calculating-strength/.

[69] *Allowable shear stress per ASME B31.3 302.3.1(b)*. Engineering forums for professionals.

(2011, November 21). Retrieved March 7, 2023, from https://www.eng-

tips.com/viewthread.cfm?qid=311040.

[70] Jones, David D. and Kocher, Michael F. (1995), *Auger design for uniform unloading of

granular material*, Biological Systems Engineering: Papers and Publications. 148.

[71] PowderProcess.net. (n.d.). *Screw conveyor design calculations step by step*. Screw conveyor

design calculation - an Engineering Guide. Retrieved March 7, 2023, from

https://powderprocess.net/Equipments%20html/Screw_Conveyor_Design.html.

[72] Dassault Systems. (2023). *Types of heat transfer analysis*. SOLIDWORKS Help. Retrieved

April 13, 2023, from https://help.solidworks.com/2019/english/SolidWorks/cworks/c_Types_

of_Heat_Transfer_Analysis.htm.

[73] Gorman, F. (n.d.). *Advanced Ceramic Solutions for the 21st Century*. Advanced Ceramic

Solutions. Retrieved March 7, 2023, from https://www.astromet.com/.

[74] *Smart Manufacturing Industrial Automation*. Rockwell Automation. (n.d.). Retrieved March

17, 2023, from https://www.rockwellautomation.com/en-us.html.

[75] American Society for Testing and Materials. (2018, October 12). *Standard Specification for

Standard Nominal Diameters and Cross-Sectional Areas of AWG Sizes of Solid Round Wires

Used as Electrical Conductors*. ASTM Compass. Retrieved March 17, 2023, from

https://compass.astm.org/document/?contentCode=ASTM%7CB0258-14%7Cen-US.

[76] NFPA. (2021). *NFPA 79: Electrical Standard for Industrial Machinery*. National Fire

Protection Agency. Retrieved March 17, 2023, from https://www.nfpa.org/codes-and-

standards/all-codes-and-standards/list-of-codes-and-standards/detail?code=79.

[77] ASME. (2019). *BPVC Section VIII-Division 1-rules for construction of pressure vessels*.

American Society of Mechanical Engineers. Retrieved March 18, 2023, from

https://www.asme.org/codes-standards/find-codes-standards/bpvc-viii-1-bpvc-section-viii-

rules-construction-pressure-vessels-division-1.

[78] Technical Glass Products. (2023). *Properties of fused quartz*. Technical Glass Products.

Retrieved March 18, 2023, from https://technicalglass.com/technical_properties/.

[79] TubingChina. (2022). *Stainless steel relative cost data*. Zhejiang Guanyu Stainless Steel

Tube Co., Ltd. Retrieved March 18, 2023, from https://tubingchina.com/Stainless-Steel-

Relative-Cost-Data.htm.

[80] Geise, S. (2023). *304 stainless steel properties*. Kloeckner Metals Corporation. Retrieved

March 18, 2023, from https://www.kloecknermetals.com/blog/304-stainless-steel-vs-316/.

[81] ASTM Compass. (2014, November 17). *Standard Test Method for Bulk Solids

Characterization by Carr Indices*. American Society for Testing and Materials. Retrieved

March 18, 2023, from https://compass.astm.org/document/?contentCode=ASTM%7CD6393-

08%7Cen-US&proxycl=https%3A%2F%2Fsecure.astm.org&fromLogin=true.

[82] *STV® Parameters for Hypertherm 65®*. STV® CNC Plasma Tables. (2023). Retrieved

February 5, 2023, from https://stvcnc.com/stvparameters65/.

[83] Jones, D. (2022, March 13). *Guide to welding joint types and parts*. WelditU. Retrieved

March 21, 2023, from https://welditu.com/welding/tips/welding-joints-welds/.

[84] AWS. (2000). *AWS D1.1: Sturctural Welding Code*. American Welding Society. Retrieved

March 22, 2023, from https://law.resource.org/pub/us/cfr/ibr/003/aws.d1.1.2000.pdf.

[85] Baker's Gas & Welding Supplies, Inc. (2023). *Guide to MIG Shielding Gas*.

Baker'sGas.com. Retrieved March 22, 2023, from https://bakersgas.com/pages/guide-to-mig-

shielding-gas.

[86] Kotecki, D. J., & Siewert, T. A. (1992, February). *WRC-1992 constitution diagram for

Stainless Steel Weld Metals*. American Welding Society. Retrieved March 22, 2023, from

http://files.aws.org/wj/supplement/WJ_1992_05_s171.pdf.

[87] J.F. Lancaster. (1999). *6 - Fusion welding processes and their thermal effects*. Metallurgy of

Welding (Sixth Edition). Woodhead Publishing. Pages 128-168.

https://doi.org/10.1533/9781845694869.128.

[88] ASME. (2019). *BPVC Section VIII-nondestructive examination*. American Society of

Mechanical Engineers. Retrieved March 22, 2023, from https://www.asme.org/codes-

standards/find-codes-standards/bpvc-v-bpvc-section-v-nondestructive-

examination/2021/print-book.

[89] American Society for Testing and Materials. (2021). *Standard Practice for Pressure Decay

Leak Test Method*. ASTM Compass. Retrieved March 22, 2023, from

https://compass.astm.org/document/?contentCode=ASTM%7CE2930-13R21%7Cen-US.

[90] TA Instruments. (n.d.). *Thermogravimetric Analysis*. TA Instruments. Retrieved April 1,

2023, from https://www.tainstruments.com/pdf/TGA%20Brochure.pdf.

[91] American Society for Testing and Materials. (2020). *Standard Test Method for

Ash in Biomass*. ASTM Compass. Retrieved March 31, 2023, from

https://compass.astm.org/document/?contentCode=ASTM%7CE1755-01R20%7Cen-US.

[92] Anton Paar GmbH. (2023). *Surface area and pore analyzers: Nova*. Anton Paar. Retrieved April 1, 2023, from https://www.anton-paar.com/us-en/products/details/nova/?prd=33871.

[93] American Society for Testing and Materials. (2021). *Standard Test Method for Carbon Black—Total and External Surface Area by Nitrogen Adsorption*. ASTM Compass. Retrieved March 31, 2023, from https://compass.astm.org/document/?contentCode=ASTM%7CD6556-21%7Cen-US.

[94] International Organization for Standardization. (2022). *Determination of the specific surface area of solids by gas adsorption — BET method*. ISO. Retrieved March 31, 2023, https://www.iso.org/standard/71014.html.

[95] LECO Corporation. (2021). *828Series Elemental Analyzers*. Retrieved April 1, 2023, from https://www.leco.com/product/828-series.

[96] American Society for Testing and Materials. (2021). *Standard Test Methods for Determination of Carbon, Hydrogen and Nitrogen in Analysis Samples of Coal and Carbon in Analysis Samples of Coal and Coke*. ASTM Compass. Retrieved March 31, 2023, from https://compass.astm.org/document/?contentCode=ASTM%7CD5373-21%7Cen-US.

[97] Bruker. *D2 PHASER*. Bruker. (2023). Retrieved April 1, 2023, from https://www.bruker.com/en/products-and-solutions/diffractometers-and-scattering-systems/x-ray-diffractometers/d2-phaser.html?s_kwcid=AL%2114677%213%21161309137635%21p%21%21g%21%21bruker+diffractometer&sc_cid=SEMB&campaign=PHASER_NA%28XRD%29&source=google&medium=cpc&keyword=bruker+diffractometer&device=c&gclid=EAIaIQobChMIwbeL1M6J_gIVohx9Ch0KRg_HEAAYASAAEgI0kfD_BwE.

[98] Renishaw, PLC. (2023). *inVia Raman Microscope*. Renishaw. Retrieved April 1, 2023, from https://www.renishaw.com/en/invia-confocal-raman-microscope--6260.

[99] American Society for Testing and Materials. (2015). *Standard Terminology Relating to Molecular Spectroscopy*. ASTM Compass. Retrieved March 31, 2023, from https://compass.astm.org/document/?contentCode=ASTM%7CE0131-10%7Cen-US.

[100] American Society for Testing and Materials. (2018). *Standard Specification for Electrodeposited Coatings of Gold for Engineering Uses*. Retrieved March 31, 2023, from https://compass.astm.org/document/?contentCode=ASTM%7CB0488-18%7Cen-US.

[101] Kim, K. C., Yoon, T. U., & Bae, Y. S. (2016). Applicability of using CO2 adsorption isotherms to determine BET surface areas of microporous materials. *Microporous and Mesoporous Materials*, *224*, 294-301.

[102] Kamp, T. (2022). SURFACE WATER/GROUNDWATER INTERACTIONS AND HYDROGEOCHEMICAL CHARACTERIZATION OF THE ELKHORNHYDROGEOCHEMICAL CHARACTERIZATION OF THE ELKHORN MINE AND MILL, BEAVERHEAD COUNTY, MONTANAMINE AND MILL, BEAVERHEAD COUNTY, MT. [Master's Thesis, Montana Technological University]. Digital Commons @ Montana Tech. https://digitalcommons.mtech.edu/cgi/viewcontent.cgi?article=1285&context=grad_rsch.

[103] Wang, X., Chen, H., Luo, K., Shao, J., & Yang, H. (2007). The influence of microwave drying on biomass pyrolysis. *Energy & Fuels*, *22*(1), 67–74. https://doi.org/10.1021/ef700300m.

[104] Raveendran, K., Ganesh, A., Khilar, K.C.: Pyrolysis characteristics of biomass and biomass components. Fuel **75**, 987–998 (1996). https://doi.org/10.1016/0016-2361(96)00030-0.

[105] Yang, H., Yan, R., Chen, H., Lee, D.H., Zheng, C.: Characteristics of hemicellulose, cellulose and lignin pyrolysis. Fuel **86**, 1781–1788 (2007). https://doi.org/10.1016/j.fuel.2006.12.013.

[106] Angelini, L., Tavarini, S.B.C., Beni, C.: Variation in mineral composition in three different plant organs of five fibre hemp (*Cannabis sativa* L.) cultivars. Agrochimica **58**, 1–18 (2014).

[107] Marrot, L., Candelier, K., Valette, J. *et al.* Valorization of Hemp Stalk Waste Through Thermochemical Conversion for Energy and Electrical Applications. *Waste Biomass Valor* **13**, 2267–2285 (2022). https://doi.org/10.1007/s12649-021-01640-6.

[108] Md. Samrat Alam, Daniel S. Alessi, Chapter 4 - Modeling the Surface Chemistry of Biochars, Biochar from Biomass and Waste, Elsevier, 2019, Pages 59-72, ISBN 9780128117293, https://doi.org/10.1016/B978-0-12-811729-3.00004-2.

[109] Asai, M., Ohba, T., Iwanaga, T., Kanoh, H., Endo, M., Campos-Delgado, J., ... & Kaneko, K. (2011). Marked adsorption irreversibility of graphitic nanoribbons for CO2 and H2O. *Journal of the American Chemical Society*, *133*(38), 14880-14883.

[110] Fernanda Gomes de Mendonça, Igor Tadeu da Cunha, Ricardo Reis Soares, Juliana Cristina Tristão, Rochel Montero Lago, Tuning the surface properties of biochar by thermal treatment, Bioresource Technology, Volume 246, 2017, Pages 28-33, ISSN 0960-8524, https://doi.org/10.1016/j.biortech.2017.07.099.

[111] Ando, T., Fujimoto, Y., & Morisaki, S. (1991). Analysis of differential scanning calorimetric data for reactive chemicals. *Journal of Hazardous Materials*, *28*(3), 251-280.

[112] Zielke, U., Hüttinger, K. J., & Hoffman, W. P. (1996). Surface-oxidized carbon fibers: I. Surface structure and chemistry. *Carbon*, *34*(8), 983-998.

[113] Chen, Y., Zhang, X., Chen, W., Yang, H., & Chen, H. (2017). The structure evolution of biochar from biomass pyrolysis and its correlation with gas pollutant adsorption performance. *Bioresource technology*, *246*, 101-109.

[114] Muzyka, R., Misztal, E., Hrabak, J., Banks, S. W., & Sajdak, M. (2023). Various biomass pyrolysis conditions influence the porosity and pore size distribution of biochar. *Energy*, *263*, 126128.

[115] Boraah, N., Chakma, S., & Kaushal, P. (2023). Optimum features of wood-based biochars: A characterization study. *Journal of Environmental Chemical Engineering*, *11*(3), 109976.

[116] Jiang, S., Nguyen, T. A., Rudolph, V., Yang, H., Zhang, D., Ok, Y. S., & Huang, L. (2017). Characterization of hard-and softwood biochars pyrolyzed at high temperature. *Environmental geochemistry and health*, *39*, 403-415.

[117] International Center for Diffraction Data. (2022, August 1). *JCPDS Pattern 96–901–6706*. ICDD.https://www.icdd.com/?gclid=Cj0KCQjwnMWkBhDLARIsAHBOftrkoj8fXQQBDF XcQGfW2FjFmc2-OfGFyRrT5apvOuGyBUsBm6GNCWUaAs4FEALw_wcB.

[118] Kumar, A., Singh, E., Khapre, A., Bordoloi, N., & Kumar, S. (2020). Sorption of volatile organic compounds on non-activated biochar. *Bioresource Technology*, *297*, 122469.

[119] Sousa, D. V. D., Guimarães, L. M., Felix, J. F., Ker, J. C., Schaefer, C. E. R., & Rodet, M. J. (2020). Dynamic of the structural alteration of biochar in ancient Anthrosol over a long timescale by Raman spectroscopy. *PloS one*, *15*(3), e0229447.

[120] Wang, Y., Alsmeyer, D. C., & McCreery, R. L. (1990). Raman spectroscopy of carbon materials: structural basis of observed spectra. *Chemistry of Materials*, *2*(5), 557-563.

[121] Ferrari, A. C. (2007). Raman spectroscopy of graphene and graphite: Disorder, electron–phonon coupling, doping and nonadiabatic effects. *Solid state communications*, *143*(1-2), 47-57.

[122] Hammes, K., Smernik, R. J., Skjemstad, J. O., & Schmidt, M. W. (2008). Characterisation and evaluation of reference materials for black carbon analysis using elemental composition, colour, BET surface area and 13C NMR spectroscopy. *Applied Geochemistry*, *23*(8), 2113-2122.

[123] Wu, F., Chen, L., Hu, P., Zhou, X., Zhou, H., Wang, D., ... & Mi, B. (2022). Comparison of properties, adsorption performance and mechanisms to Cd (II) on lignin-derived biochars under different pyrolysis temperatures by microwave heating. *Environmental Technology & Innovation*, *25*, 102196.

[124] *Industrial Gases*. General Distributing Company. (2023, January 31). https://gendco.com/.

[125] *General Service 1 Rates*. NorthWestern Energy. (2023). https://rates.northwesternenergy.com/GSPrimaryNonDemandrates.aspx?_ga=2.169277857.1474406325.1686063443-975318453.1677103998.

10.   Appendix A: Bill of Materials

Quantity	Price	Total	Description
1	442.78	442.78	24" x 60" x 9" 1600 lb Capacity Dunnage Rack
1	90.00	90.00	0.09" Aluminum Sheet
1	60.57	60.57	Crush-Resistant Spiral Duct (5ft)
2	37.15	74.30	Trade Size 6 90 Degree Elbow for Spiral Duct
1	10.69	10.69	Steel Duct Flange
4	172.08	688.32	Custom Cut 1/8" Polycarbonate
9	48.76	438.84	T-Slotted Framing (10ft)
50	6.11	305.50	T-Slot Corner Brace
3	19.39	58.17	Rail-to-Rail Hinge for 1" High Rail, Black
1	37.51	37.51	Silver Aluminum Slide Bolt Latch
1	10.96	10.96	Sure-Grip Pull Handle, 4-11/16" Long for 1" High Rail
1	55.64	55.64	Swinging Vane Airflow Meter
125	0.71	88.75	1/4"-20 Drop-in Hammer Nut with Button Head
2	17.76	35.52	Stem Mount Caster for 1.5" High Single Rail
1	4.32	4.32	2" Width, 1' Length Piano Hinge
1	32.90	32.90	Push-On Rubber Seal with Wiper
1	1404.00	1404.00	3/8"x4'x4' Stainless Steel Plate
1	3818.00	3818.00	1/2"x4'x8' Stainless Steel Plate
1	35.34	35.34	1/4" OD Stainless Steel Rod
30	1.29	38.70	Steel Corner Bracket
1	56.90	56.90	1"x1"x1' Stainless Steel Bar
1	77.72	77.72	KF25 Sanitary Fitting
1	69.35	69.35	KF16 Sanitary Fitting
1	19.69	19.69	3/8" ID Copper Washers
1	5.17	5.17	3/8"-24 Hex Nut
8	14.24	113.92	High-Temperature Silicone Adhesive Gasket
1	35.84	35.84	DuPont High Vacuum Grease
1	131.25	131.25	1" OD High Vacuum Exhaust Hose
1	71.38	71.38	Quick-Clamp KF25 90° Stainless Steel Elbow
2	43.04	86.08	KF25 Ring with Screen
1	91.54	91.54	High-Temperature Quartz Wool
2	102.27	204.54	KF25-1/2"NPT Reducing Fitting
2	36.60	73.20	1/2"OD PVDF Plastic Tubing
2	10.52	21.04	5/8" Hose Clamp
1	3190.00	3190.00	SH Cold Trap Bath -40°C
4	6.50	26.00	KF25 Ring
1	4.50	4.50	KF16 Ring
6	7.00	42.00	KF25 Tri-Clamp
1	6.00	6.00	KF16 Tri-Clamp
1	257.00	257.00	KF25 Vacuum Inlet Filter
1	1728.00	1728.00	CMR 362 KF16 Vacuum Sensor
1	6281.30	6281.30	HiScroll 12 Vacuum Pump
1	164.99	164.99	VEVOR Industrial Chiller

1	109.99	109.99	Corrosion Inhibitor
1	23000.00	23000.00	Inductive Heating System
1	35.00	35.00	K-Type Thermocouple
3	9.63	28.89	1/4"-20 Hex Screw
2	127.50	255.00	8"x8"x1" Stainless Steel Plate
1	649.77	649.77	Stainless Steel Pipe Size 4
1	223.31	223.31	Stainless Steel Pipe Size 6
1	1705.00	1705.00	Quartz Tube
1	2722.00	2722.00	AR-12 Graphite Round Stock
2	156.00	312.00	R16 Full Ceramic Bearings (1.000″ X 2.000″ X 0.500″)
20	7.60	152.00	Screw-on Draw Latch
5	1.66	8.30	Screw-on Spring Clamp
1	482.00	482.00	STP-MTRACH-42202 Motor
1	103.00	103.00	STP-DRV-6575 VFD
1	1200.00	1200.00	YTZP Ceramic Shaft
1	23.60	23.60	3/8"-24 Stainless Steel Threaded Rod
1	5.79	5.79	3' Ethernet Cable
2	28.11	56.22	15' Multi-Outlet Extension Cord
1	16.97	16.97	9' Power Cord Pigtail
2	18.49	36.98	13mm Panel Light
1	61.34	61.34	Pull Reset Emergency Stop Button
1	3600.00	3600.00	PLC Modules and HMI
2	12.13	24.26	18AWG Solid Core Wire
1	17.99	17.99	Heat Shrink Wire Labels
50	1.17	58.50	Phoenix Contact Terminal Block
2	5.48	10.96	Phoenix Contact Terminal Block Jumper
10	1.71	17.10	Phoenix Contact Terminal Block Label
1	980.00	980.00	Optris CTlaser 3ML
Total			$56,384.19

11. Appendix B: Welding Inspection Documentation

Non-Destructive Examination - Fabrication - Heat Treatment
Welding/NDE Consulting - Welding and NDE Training/Testing

Kerry O'Leary - Owner/Operator
CWI/ASNT NDT Level III

PO Box 4362, Butte, MT 59702
kerry@weldingservicesmt.com
(406)490-0966

PIPING AND VESSEL INSPECTION REPORT FORM

Project:	Bottom Bin Vessel
Location:	Butte, MT
Brief Summary:	Visual and dye penetrant testing of a square tank.

Governing Codes		Date(s)	Trip #	Inspections Performed	
ASME Section I		03/06/23;	1,2	Continuous Visual Ins.	
ASME Section V	x	03/13/23		Periodic Visual Inspection	x
ASME Section VIII	x			Ultrasonic Testing	
ASME Section IX				Magnetic Particle Testing	
ASME B31.1				Dye Penetrant Testing	x
ASME B31.3				Other:	
ASME BPE					

Items Requiring Formal Non-Conformance Report (Attached if Needed)

Yes		If Yes, Description:	
No	x		

Inspector	Stamps and Certifications	
Kerry O'Leary	Kerry P O'Leary CWI 07080081 QC1 EXP. 8/1/2022	Kerry P O'Leary ASNT NDT Level III Expiration 8/25 Cert. # 192837
	Kerry P O'Leary API 510 #40788 API 570 #42039 Expiration 7/31/23	

1. DYE PENETRANT TESTING FORM

WS-PT-RF-2-1	WS-ASME-PT-5-0	N/A	03/06/23; 03/13/23
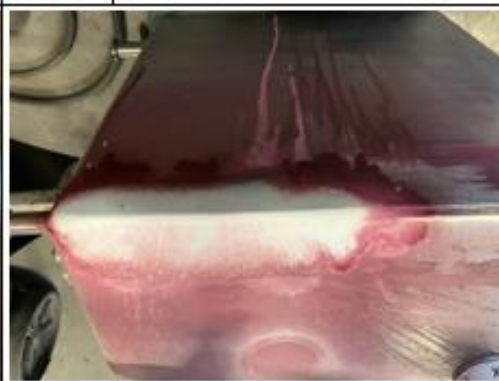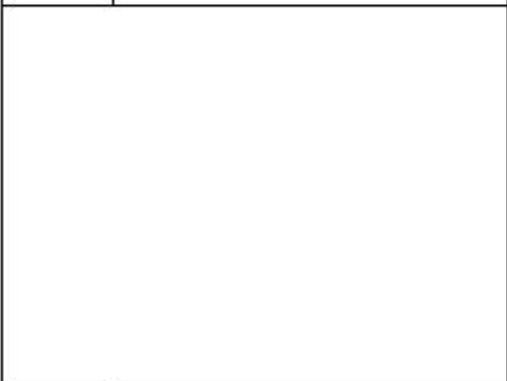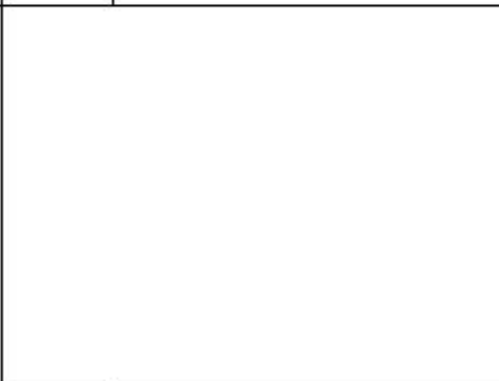
Client	Montana Tech	Specification	ASME Section V
Purchase Order	N/A	Acceptance Criteria	ASME Section VIII
Drawing Number	BottomBin, Welding	NDE Procedure	WS-ASME-PT-5-0

Examination Information				
Material Type	Stainless Steel	Surface Condition	Polished	
Lighting Use	Ambient, Flashlight	Illuminance greater than 100 Foot Candles?		Yes
Temperature Indicating Device Serial No.	Room Tstat	Material Temperature between 50F-125F?		Yes
Material Temperature between 40F-50F?	No	Double Penetrant Dwell Time if Material is 40F-50F		

Penetrant System Type			Visible Dye			Penetrant System Brand		Dynaflux	
Batch Nos.	C	19226	P	12102A	D	18295C	Cleaner	C-NF	Dwell	1 min
Penetrant		P-HF	Dwell		5-10 mins	Developer	D-NF	Dwell	10-30 mins

Results			
Part ID	Details/Location	Accept/Reject	Date
Bottom Left	No relevant indications noted.	Accept	03/06/23
Bottom Right	No relevant indications noted.	Accept	03/06/23
Bottom Back	No relevant indications noted.	Accept	03/06/23
Top Left	No relevant indications noted.	Accept	03/06/23
Top Right	No relevant indications noted.	Accept	03/06/23
Top Back	No relevant indications noted.	Accept	03/06/23
Left Back	No relevant indications noted.	Accept	03/06/23
Right Back	2x 1/16" IF + 1.5" crack within 4" of the seam intersection with the top back.	Reject	03/06/23
Top Door	No relevant indications noted.	Accept	03/06/23
Bottom Door	No relevant indications noted.	Accept	03/06/23
Left Door	No relevant indications noted.	Accept	03/06/23
Right Door	No relevant indications noted.	Accept	03/06/23
Flange Joint	Multiple areas of overlap IF throughout circumference. Repair 1: no relevant indications remain.	Accept after repairs	03/06/23; 03/13/23
Right Back	Repair 1: 3x 1/16" IF + 1" crack within 6" of the seam intersection with the top back. Repair 2: No rel. indications.	Accept after repairs	03/13/23; 03/24/23

Examiner / Level	Kerry O'Leary ASNT Level III	*(signature)*	Date	03/06/23; 03/13/23

Figure 1 Initial weld cracking.	Figure 2 Crack repair attempt #1.
Figure 3 Crack repair attempt #2.	Figure 4 Crack repair attempt #3.
Figure 5	Figure 6

12.   Appendix C: Graphite Auger G-Code

Graphite round was fixed into the 2.54cm (1in) spindle collet and live-end connector for turning. The part references were manually set by touching the tool to the 11.7cm (4.6in) outer diameter (x-face) and right end (z-face) of the part. Completion of the program generated a 5.1cm (2in) pitch spiral cut with a 0.95cm (0.375in) thickness. The auger blades were thinned by increasing the cut length by 0.76cm (0.300in) and increasing the tool z-wear by 0.76cm (0.300in). The finished product is presented below with the necessary g-code subsequent.

O0001

(2 INCH AUGER)

(DATE=DD-MM-YY - 23-03-23 TIME=HH:MM - 11:31)

(MCX FILE - C:\USERS\DOUBL\DOCUMENTS\MY MCAM2018\PARTS\AUGER5LATHE.MCAM)

(NC FILE - C:\USERS\DOUBL\DOCUMENTS\MY MCAM2018\LATHE\NC\T.nc)

(MATERIAL - STEEL INCH - 1030 - 200 BHN)

G20

(TOOL - 1 OFFSET - 1)

(OD CUTOFF RIGHT INSERT - NONE)

T101

G97 S25 M03

G0 G54 X4.615 Z1.05 M8

X4.611

G99 G32 Z-10.35 F2.

G0 X4.615

Z1.05

X4.607

G32 Z-10.35 F2.

G0 X4.615

Z1.05

X4.603

G32 Z-10.35 F2.

G0 X4.615

Z1.05

X4.599

G32 Z-10.35 F2.

G0 X4.615

Z1.05

X4.595

G32 Z-10.35 F2.

G0 X4.615

Z1.05

X4.591

G32 Z-10.35 F2.

G0 X4.615

Z1.05

X4.587

G32 Z-10.35 F2.

G0 X4.615

Z1.05

X4.583

G32 Z-10.35 F2.

G0 X4.615

Z1.05

X4.579

G32 Z-10.35 F2.

G0 X4.615

Z1.05

X4.575

G32 Z-10.35 F2.

G0 X4.615

Z1.05

X4.5709

G32 Z-10.35 F2.

G0 X4.615

Z1.05

X4.5669

G32 Z-10.35 F2.

G0 X4.615

Z1.05

X4.5629

G32 Z-10.35 F2.

G0 X4.615

Z1.05

X4.5589

G32 Z-10.35 F2.

G0 X4.615

Z1.05

X4.5549

G32 Z-10.35 F2.

G0 X4.615

Z1.05

X4.5509

G32 Z-10.35 F2.

G0 X4.615

Z1.05

X4.5469

G32 Z-10.35 F2.

G0 X4.615

Z1.05

X4.5429

G32 Z-10.35 F2.

G0 X4.615

Z1.05

X4.5389

G32 Z-10.35 F2.

G0 X4.615

Z1.05

X4.5349

G32 Z-10.35 F2.

G0 X4.615

Z1.05

X4.5309

G32 Z-10.35 F2.

G0 X4.615

Z1.05

X4.5269

G32 Z-10.35 F2.

G0 X4.615

Z1.05

X4.5229

G32 Z-10.35 F2.

G0 X4.615

Z1.05

X4.5189

G32 Z-10.35 F2.

G0 X4.615

Z1.05

X4.5149

G32 Z-10.35 F2.

G0 X4.615

Z1.05

X4.5109

G32 Z-10.35 F2.

G0 X4.615

Z1.05

X4.5069

G32 Z-10.35 F2.

G0 X4.615

Z1.05

X4.5029

G32 Z-10.35 F2.

G0 X4.615

Z1.05

X4.4989

G32 Z-10.35 F2.

G0 X4.615

Z1.05

X4.4949

G32 Z-10.35 F2.

G0 X4.615

Z1.05

X4.4909

G32 Z-10.35 F2.

G0 X4.615

Z1.05

X4.4869

G32 Z-10.35 F2.

G0 X4.615

Z1.05

X4.4828

G32 Z-10.35 F2.

G0 X4.615

Z1.05

X4.4788

G32 Z-10.35 F2.

G0 X4.615

Z1.05

X4.4748

G32 Z-10.35 F2.

G0 X4.615

Z1.05

X4.4708

G32 Z-10.35 F2.

G0 X4.615

Z1.05

X4.4668

G32 Z-10.35 F2.

G0 X4.615

Z1.05

X4.4628

G32 Z-10.35 F2.

G0 X4.615

Z1.05

X4.4588

G32 Z-10.35 F2.

G0 X4.615

Z1.05

X4.4548

G32 Z-10.35 F2.

G0 X4.615

Z1.05

X4.4508

G32 Z-10.35 F2.

G0 X4.615

Z1.05

X4.4468

G32 Z-10.35 F2.

G0 X4.615

Z1.05

X4.4428

G32 Z-10.35 F2.

G0 X4.615

Z1.05

X4.4388

G32 Z-10.35 F2.

G0 X4.615

Z1.05

X4.4348

G32 Z-10.35 F2.

G0 X4.615

Z1.05

X4.4308

G32 Z-10.35 F2.

G0 X4.615

Z1.05

X4.4268

G32 Z-10.35 F2.

G0 X4.615

Z1.05

X4.4228

G32 Z-10.35 F2.

G0 X4.615

Z1.05

X4.4188

G32 Z-10.35 F2.

G0 X4.615

Z1.05

X4.4148

G32 Z-10.35 F2.

G0 X4.615

Z1.05

X4.4108

G32 Z-10.35 F2.

G0 X4.615

Z1.05

X4.4068

G32 Z-10.35 F2.

G0 X4.615

Z1.05

X4.4028

G32 Z-10.35 F2.

G0 X4.615

Z1.05

X4.3988

G32 Z-10.35 F2.

G0 X4.615

Z1.05

X4.3947

G32 Z-10.35 F2.

G0 X4.615

Z1.05

X4.3907

G32 Z-10.35 F2.

G0 X4.615

Z1.05

X4.3867

G32 Z-10.35 F2.

G0 X4.615

Z1.05

X4.3827

G32 Z-10.35 F2.

G0 X4.615

Z1.05

X4.3787

G32 Z-10.35 F2.

G0 X4.615

Z1.05

X4.3747

G32 Z-10.35 F2.

G0 X4.615

Z1.05

X4.3707

G32 Z-10.35 F2.

G0 X4.615

Z1.05

X4.3667

G32 Z-10.35 F2.

G0 X4.615

Z1.05

X4.3627

G32 Z-10.35 F2.

G0 X4.615

Z1.05

X4.3587

G32 Z-10.35 F2.

G0 X4.615

Z1.05

X4.3547

G32 Z-10.35 F2.

G0 X4.615

Z1.05

X4.3507

G32 Z-10.35 F2.

G0 X4.615

Z1.05

X4.3467

G32 Z-10.35 F2.

G0 X4.615

Z1.05

X4.3427

G32 Z-10.35 F2.

G0 X4.615

Z1.05

X4.3387

G32 Z-10.35 F2.

G0 X4.615

Z1.05

X4.3347

G32 Z-10.35 F2.

G0 X4.615

Z1.05

X4.3307

G32 Z-10.35 F2.

G0 X4.615

Z1.05

X4.3267

G32 Z-10.35 F2.

G0 X4.615

Z1.05

X4.3227

G32 Z-10.35 F2.

G0 X4.615

Z1.05

X4.3187

G32 Z-10.35 F2.

G0 X4.615

Z1.05

X4.3147

G32 Z-10.35 F2.

G0 X4.615

Z1.05

X4.3107

G32 Z-10.35 F2.

G0 X4.615

Z1.05

X4.3066

G32 Z-10.35 F2.

G0 X4.615

Z1.05

X4.3026

G32 Z-10.35 F2.

G0 X4.615

Z1.05

X4.2986

G32 Z-10.35 F2.

G0 X4.615

Z1.05

X4.2946

G32 Z-10.35 F2.

G0 X4.615

Z1.05

X4.2906

G32 Z-10.35 F2.

G0 X4.615

Z1.05

X4.2866

G32 Z-10.35 F2.

G0 X4.615

Z1.05

X4.2826

G32 Z-10.35 F2.

G0 X4.615

Z1.05

X4.2786

G32 Z-10.35 F2.

G0 X4.615

Z1.05

X4.2746

G32 Z-10.35 F2.

G0 X4.615

Z1.05

X4.2706

G32 Z-10.35 F2.

G0 X4.615

Z1.05

X4.2666

G32 Z-10.35 F2.

G0 X4.615

Z1.05

X4.2626

G32 Z-10.35 F2.

G0 X4.615

Z1.05

X4.2586

G32 Z-10.35 F2.

G0 X4.615

Z1.05

X4.2546

G32 Z-10.35 F2.

G0 X4.615

Z1.05

X4.2506

G32 Z-10.35 F2.

G0 X4.615

Z1.05

X4.2466

G32 Z-10.35 F2.

G0 X4.615

Z1.05

X4.2426

G32 Z-10.35 F2.

G0 X4.615

Z1.05

X4.2386

G32 Z-10.35 F2.

G0 X4.615

Z1.05

X4.2346

G32 Z-10.35 F2.

G0 X4.615

Z1.05

X4.2306

G32 Z-10.35 F2.

G0 X4.615

Z1.05

X4.2266

G32 Z-10.35 F2.

G0 X4.615

Z1.05

X4.2225

G32 Z-10.35 F2.

G0 X4.615

Z1.05

X4.2185

G32 Z-10.35 F2.

G0 X4.615

Z1.05

X4.2145

G32 Z-10.35 F2.

G0 X4.615

Z1.05

X4.2105

G32 Z-10.35 F2.

G0 X4.615

Z1.05

X4.2065

G32 Z-10.35 F2.

G0 X4.615

Z1.05

X4.2025

G32 Z-10.35 F2.

G0 X4.615

Z1.05

X4.1985

G32 Z-10.35 F2.

G0 X4.615

Z1.05

X4.1945

G32 Z-10.35 F2.

G0 X4.615

Z1.05

X4.1905

G32 Z-10.35 F2.

G0 X4.615

Z1.05

X4.1865

G32 Z-10.35 F2.

G0 X4.615

Z1.05

X4.1825

G32 Z-10.35 F2.

G0 X4.615

Z1.05

X4.1785

G32 Z-10.35 F2.

G0 X4.615

Z1.05

X4.1745

G32 Z-10.35 F2.

G0 X4.615

Z1.05

X4.1705

G32 Z-10.35 F2.

G0 X4.615

Z1.05

X4.1665

G32 Z-10.35 F2.

G0 X4.615

Z1.05

X4.1625

G32 Z-10.35 F2.

G0 X4.615

Z1.05

X4.1585

G32 Z-10.35 F2.

G0 X4.615

Z1.05

X4.1545

G32 Z-10.35 F2.

G0 X4.615

Z1.05

X4.1505

G32 Z-10.35 F2.

G0 X4.615

Z1.05

X4.1465

G32 Z-10.35 F2.

G0 X4.615

Z1.05

X4.1425

G32 Z-10.35 F2.

G0 X4.615

Z1.05

X4.1385

G32 Z-10.35 F2.

G0 X4.615

Z1.05

X4.1344

G32 Z-10.35 F2.

G0 X4.615

Z1.05

X4.1304

G32 Z-10.35 F2.

G0 X4.615

Z1.05

X4.1264

G32 Z-10.35 F2.

G0 X4.615

Z1.05

X4.1224

G32 Z-10.35 F2.

G0 X4.615

Z1.05

X4.1184

G32 Z-10.35 F2.

G0 X4.615

Z1.05

X4.1144

G32 Z-10.35 F2.

G0 X4.615

Z1.05

X4.1104

G32 Z-10.35 F2.

G0 X4.615

Z1.05

X4.1064

G32 Z-10.35 F2.

G0 X4.615

Z1.05

X4.1024

G32 Z-10.35 F2.

G0 X4.615

Z1.05

X4.0984

G32 Z-10.35 F2.

G0 X4.615

Z1.05

X4.0944

G32 Z-10.35 F2.

G0 X4.615

Z1.05

X4.0904

G32 Z-10.35 F2.

G0 X4.615

Z1.05

X4.0864

G32 Z-10.35 F2.

G0 X4.615

Z1.05

X4.0824

G32 Z-10.35 F2.

G0 X4.615

Z1.05

X4.0784

G32 Z-10.35 F2.

G0 X4.615

Z1.05

X4.0744

G32 Z-10.35 F2.

G0 X4.615

Z1.05

X4.0704

G32 Z-10.35 F2.

G0 X4.615

Z1.05

X4.0664

G32 Z-10.35 F2.

G0 X4.615

Z1.05

X4.0624

G32 Z-10.35 F2.

G0 X4.615

Z1.05

X4.0584

G32 Z-10.35 F2.

G0 X4.615

Z1.05

X4.0544

G32 Z-10.35 F2.

G0 X4.615

Z1.05

X4.0504

G32 Z-10.35 F2.

G0 X4.615

Z1.05

X4.0463

G32 Z-10.35 F2.

G0 X4.615

Z1.05

X4.0423

G32 Z-10.35 F2.

G0 X4.615

Z1.05

X4.0383

G32 Z-10.35 F2.

G0 X4.615

Z1.05

X4.0343

G32 Z-10.35 F2.

G0 X4.615

Z1.05

X4.0303

G32 Z-10.35 F2.

G0 X4.615

Z1.05

X4.0263

G32 Z-10.35 F2.

G0 X4.615

Z1.05

X4.0223

G32 Z-10.35 F2.

G0 X4.615

Z1.05

X4.0183

G32 Z-10.35 F2.

G0 X4.615

Z1.05

X4.0143

G32 Z-10.35 F2.

G0 X4.615

Z1.05

X4.0103

G32 Z-10.35 F2.

G0 X4.615

Z1.05

X4.0063

G32 Z-10.35 F2.

G0 X4.615

Z1.05

X4.0023

G32 Z-10.35 F2.

G0 X4.615

Z1.05

X3.9983

G32 Z-10.35 F2.

G0 X4.615

Z1.05

X3.9943

G32 Z-10.35 F2.

G0 X4.615

Z1.05

X3.9903

G32 Z-10.35 F2.

G0 X4.615

Z1.05

X3.9863

G32 Z-10.35 F2.

G0 X4.615

Z1.05

X3.9823

G32 Z-10.35 F2.

G0 X4.615

Z1.05

X3.9783

G32 Z-10.35 F2.

G0 X4.615

Z1.05

X3.9743

G32 Z-10.35 F2.

G0 X4.615

Z1.05

X3.9703

G32 Z-10.35 F2.

G0 X4.615

Z1.05

X3.9663

G32 Z-10.35 F2.

G0 X4.615

Z1.05

X3.9623

G32 Z-10.35 F2.

G0 X4.615

Z1.05

X3.9582

G32 Z-10.35 F2.

G0 X4.615

Z1.05

X3.9542

G32 Z-10.35 F2.

G0 X4.615

Z1.05

X3.9502

G32 Z-10.35 F2.

G0 X4.615

Z1.05

X3.9462

G32 Z-10.35 F2.

G0 X4.615

Z1.05

X3.9422

G32 Z-10.35 F2.

G0 X4.615

Z1.05

X3.9382

G32 Z-10.35 F2.

G0 X4.615

Z1.05

X3.9342

G32 Z-10.35 F2.

G0 X4.615

Z1.05

X3.9302

G32 Z-10.35 F2.

G0 X4.615

Z1.05

X3.9262

G32 Z-10.35 F2.

G0 X4.615

Z1.05

X3.9222

G32 Z-10.35 F2.

G0 X4.615

Z1.05

X3.9182

G32 Z-10.35 F2.

G0 X4.615

Z1.05

X3.9142

G32 Z-10.35 F2.

G0 X4.615

Z1.05

X3.9102

G32 Z-10.35 F2.

G0 X4.615

Z1.05

X3.9062

G32 Z-10.35 F2.

G0 X4.615

Z1.05

X3.9022

G32 Z-10.35 F2.

G0 X4.615

Z1.05

X3.8982

G32 Z-10.35 F2.

G0 X4.615

Z1.05

X3.8942

G32 Z-10.35 F2.

G0 X4.615

Z1.05

X3.8902

G32 Z-10.35 F2.

G0 X4.615

Z1.05

X3.8862

G32 Z-10.35 F2.

G0 X4.615

Z1.05

X3.8822

G32 Z-10.35 F2.

G0 X4.615

Z1.05

X3.8782

G32 Z-10.35 F2.

G0 X4.615

Z1.05

X3.8742

G32 Z-10.35 F2.

G0 X4.615

Z1.05

X3.8701

G32 Z-10.35 F2.

G0 X4.615

Z1.05

X3.8661

G32 Z-10.35 F2.

G0 X4.615

Z1.05

X3.8621

G32 Z-10.35 F2.

G0 X4.615

Z1.05

X3.8581

G32 Z-10.35 F2.

G0 X4.615

Z1.05

X3.8541

G32 Z-10.35 F2.

G0 X4.615

Z1.05

X3.8501

G32 Z-10.35 F2.

G0 X4.615

Z1.05

X3.8461

G32 Z-10.35 F2.

G0 X4.615

Z1.05

X3.8421

G32 Z-10.35 F2.

G0 X4.615

Z1.05

X3.8381

G32 Z-10.35 F2.

G0 X4.615

Z1.05

X3.8341

G32 Z-10.35 F2.

G0 X4.615

Z1.05

X3.8301

G32 Z-10.35 F2.

G0 X4.615

Z1.05

X3.8261

G32 Z-10.35 F2.

G0 X4.615

Z1.05

X3.8221

G32 Z-10.35 F2.

G0 X4.615

Z1.05

X3.8181

G32 Z-10.35 F2.

G0 X4.615

Z1.05

X3.8141

G32 Z-10.35 F2.

G0 X4.615

Z1.05

X3.8101

G32 Z-10.35 F2.

G0 X4.615

Z1.05

X3.8061

G32 Z-10.35 F2.

G0 X4.615

Z1.05

X3.8021

G32 Z-10.35 F2.

G0 X4.615

Z1.05

X3.7981

G32 Z-10.35 F2.

G0 X4.615

Z1.05

X3.7941

G32 Z-10.35 F2.

G0 X4.615

Z1.05

X3.7901

G32 Z-10.35 F2.

G0 X4.615

Z1.05

X3.786

G32 Z-10.35 F2.

G0 X4.615

Z1.05

X3.782

G32 Z-10.35 F2.

G0 X4.615

Z1.05

X3.778

G32 Z-10.35 F2.

G0 X4.615

Z1.05

X3.774

G32 Z-10.35 F2.

G0 X4.615

Z1.05

X3.77

G32 Z-10.35 F2.

G0 X4.615

Z1.05

X3.766

G32 Z-10.35 F2.

G0 X4.615

Z1.05

X3.762

G32 Z-10.35 F2.

G0 X4.615

Z1.05

X3.758

G32 Z-10.35 F2.

G0 X4.615

Z1.05

X3.754

G32 Z-10.35 F2.

G0 X4.615

Z1.05

X3.75

G32 Z-10.35 F2.

G0 X4.615

Z1.05

X3.746

G32 Z-10.35 F2.

G0 X4.615

Z1.05

X3.742

G32 Z-10.35 F2.

G0 X4.615

Z1.05

X3.738

G32 Z-10.35 F2.

G0 X4.615

Z1.05

X3.734

G32 Z-10.35 F2.

G0 X4.615

Z1.05

X3.73

G32 Z-10.35 F2.

G0 X4.615

Z1.05

X3.726

G32 Z-10.35 F2.

G0 X4.615

Z1.05

X3.722

G32 Z-10.35 F2.

G0 X4.615

Z1.05

X3.718

G32 Z-10.35 F2.

G0 X4.615

Z1.05

X3.714

G32 Z-10.35 F2.

G0 X4.615

Z1.05

X3.71

G32 Z-10.35 F2.

G0 X4.615

Z1.05

X3.706

G32 Z-10.35 F2.

G0 X4.615

Z1.05

X3.702

G32 Z-10.35 F2.

G0 X4.615

Z1.05

X3.6979

G32 Z-10.35 F2.

G0 X4.615

Z1.05

X3.6939

G32 Z-10.35 F2.

G0 X4.615

Z1.05

X3.6899

G32 Z-10.35 F2.

G0 X4.615

Z1.05

X3.6859

G32 Z-10.35 F2.

G0 X4.615

Z1.05

X3.6819

G32 Z-10.35 F2.

G0 X4.615

Z1.05

X3.6779

G32 Z-10.35 F2.

G0 X4.615

Z1.05

X3.6739

G32 Z-10.35 F2.

G0 X4.615

Z1.05

X3.6699

G32 Z-10.35 F2.

G0 X4.615

Z1.05

X3.6659

G32 Z-10.35 F2.

G0 X4.615

Z1.05

X3.6619

G32 Z-10.35 F2.

G0 X4.615

Z1.05

X3.6579

G32 Z-10.35 F2.

G0 X4.615

Z1.05

X3.6539

G32 Z-10.35 F2.

G0 X4.615

Z1.05

X3.6499

G32 Z-10.35 F2.

G0 X4.615

Z1.05

X3.6459

G32 Z-10.35 F2.

G0 X4.615

Z1.05

X3.6419

G32 Z-10.35 F2.

G0 X4.615

Z1.05

X3.6379

G32 Z-10.35 F2.

G0 X4.615

Z1.05

X3.6339

G32 Z-10.35 F2.

G0 X4.615

Z1.05

X3.6299

G32 Z-10.35 F2.

G0 X4.615

Z1.05

X3.6259

G32 Z-10.35 F2.

G0 X4.615

Z1.05

X3.6219

G32 Z-10.35 F2.

G0 X4.615

Z1.05

X3.6179

G32 Z-10.35 F2.

G0 X4.615

Z1.05

X3.6139

G32 Z-10.35 F2.

G0 X4.615

Z1.05

X3.6098

G32 Z-10.35 F2.

G0 X4.615

Z1.05

X3.6058

G32 Z-10.35 F2.

G0 X4.615

Z1.05

X3.6018

G32 Z-10.35 F2.

G0 X4.615

Z1.05

X3.5978

G32 Z-10.35 F2.

G0 X4.615

Z1.05

X3.5938

G32 Z-10.35 F2.

G0 X4.615

Z1.05

X3.5898

G32 Z-10.35 F2.

G0 X4.615

Z1.05

X3.5858

G32 Z-10.35 F2.

G0 X4.615

Z1.05

X3.5818

G32 Z-10.35 F2.

G0 X4.615

Z1.05

X3.5778

G32 Z-10.35 F2.

G0 X4.615

Z1.05

X3.5738

G32 Z-10.35 F2.

G0 X4.615

Z1.05

X3.5698

G32 Z-10.35 F2.

G0 X4.615

Z1.05

X3.5658

G32 Z-10.35 F2.

G0 X4.615

Z1.05

X3.5618

G32 Z-10.35 F2.

G0 X4.615

Z1.05

X3.5578

G32 Z-10.35 F2.

G0 X4.615

Z1.05

X3.5538

G32 Z-10.35 F2.

G0 X4.615

Z1.05

X3.5498

G32 Z-10.35 F2.

G0 X4.615

Z1.05

X3.5458

G32 Z-10.35 F2.

G0 X4.615

Z1.05

X3.5418

G32 Z-10.35 F2.

G0 X4.615

Z1.05

X3.5378

G32 Z-10.35 F2.

G0 X4.615

Z1.05

X3.5338

G32 Z-10.35 F2.

G0 X4.615

Z1.05

X3.5298

G32 Z-10.35 F2.

G0 X4.615

Z1.05

X3.5258

G32 Z-10.35 F2.

G0 X4.615

Z1.05

X3.5217

G32 Z-10.35 F2.

G0 X4.615

Z1.05

X3.5177

G32 Z-10.35 F2.

G0 X4.615

Z1.05

X3.5137

G32 Z-10.35 F2.

G0 X4.615

Z1.05

X3.5097

G32 Z-10.35 F2.

G0 X4.615

Z1.05

X3.5057

G32 Z-10.35 F2.

G0 X4.615

Z1.05

X3.5017

G32 Z-10.35 F2.

G0 X4.615

Z1.05

X3.4977

G32 Z-10.35 F2.

G0 X4.615

Z1.05

X3.4937

G32 Z-10.35 F2.

G0 X4.615

Z1.05

X3.4897

G32 Z-10.35 F2.

G0 X4.615

Z1.05

X3.4857

G32 Z-10.35 F2.

G0 X4.615

Z1.05

X3.4817

G32 Z-10.35 F2.

G0 X4.615

Z1.05

X3.4777

G32 Z-10.35 F2.

G0 X4.615

Z1.05

X3.4737

G32 Z-10.35 F2.

G0 X4.615

Z1.05

X3.4697

G32 Z-10.35 F2.

G0 X4.615

Z1.05

X3.4657

G32 Z-10.35 F2.

G0 X4.615

Z1.05

X3.4617

G32 Z-10.35 F2.

G0 X4.615

Z1.05

X3.4577

G32 Z-10.35 F2.

G0 X4.615

Z1.05

X3.4537

G32 Z-10.35 F2.

G0 X4.615

Z1.05

X3.4497

G32 Z-10.35 F2.

G0 X4.615

Z1.05

X3.4457

G32 Z-10.35 F2.

G0 X4.615

Z1.05

X3.4417

G32 Z-10.35 F2.

G0 X4.615

Z1.05

X3.4376

G32 Z-10.35 F2.

G0 X4.615

Z1.05

X3.4336

G32 Z-10.35 F2.

G0 X4.615

Z1.05

X3.4296

G32 Z-10.35 F2.

G0 X4.615

Z1.05

X3.4256

G32 Z-10.35 F2.

G0 X4.615

Z1.05

X3.4216

G32 Z-10.35 F2.

G0 X4.615

Z1.05

X3.4176

G32 Z-10.35 F2.

G0 X4.615

Z1.05

X3.4136

G32 Z-10.35 F2.

G0 X4.615

Z1.05

X3.4096

G32 Z-10.35 F2.

G0 X4.615

Z1.05

X3.4056

G32 Z-10.35 F2.

G0 X4.615

Z1.05

X3.4016

G32 Z-10.35 F2.

G0 X4.615

Z1.05

X3.3976

G32 Z-10.35 F2.

G0 X4.615

Z1.05

X3.3936

G32 Z-10.35 F2.

G0 X4.615

Z1.05

X3.3896

G32 Z-10.35 F2.

G0 X4.615

Z1.05

X3.3856

G32 Z-10.35 F2.

G0 X4.615

Z1.05

X3.3816

G32 Z-10.35 F2.

G0 X4.615

Z1.05

X3.3776

G32 Z-10.35 F2.

G0 X4.615

Z1.05

X3.3736

G32 Z-10.35 F2.

G0 X4.615

Z1.05

X3.3696

G32 Z-10.35 F2.

G0 X4.615

Z1.05

X3.3656

G32 Z-10.35 F2.

G0 X4.615

Z1.05

X3.3616

G32 Z-10.35 F2.

G0 X4.615

Z1.05

X3.3576

G32 Z-10.35 F2.

G0 X4.615

Z1.05

X3.3536

G32 Z-10.35 F2.

G0 X4.615

Z1.05

X3.3495

G32 Z-10.35 F2.

G0 X4.615

Z1.05

X3.3455

G32 Z-10.35 F2.

G0 X4.615

Z1.05

X3.3415

G32 Z-10.35 F2.

G0 X4.615

Z1.05

X3.3375

G32 Z-10.35 F2.

G0 X4.615

Z1.05

X3.3335

G32 Z-10.35 F2.

G0 X4.615

Z1.05

X3.3295

G32 Z-10.35 F2.

G0 X4.615

Z1.05

X3.3255

G32 Z-10.35 F2.

G0 X4.615

Z1.05

X3.3215

G32 Z-10.35 F2.

G0 X4.615

Z1.05

X3.3175

G32 Z-10.35 F2.

G0 X4.615

Z1.05

X3.3135

G32 Z-10.35 F2.

G0 X4.615

Z1.05

X3.3095

G32 Z-10.35 F2.

G0 X4.615

Z1.05

X3.3055

G32 Z-10.35 F2.

G0 X4.615

Z1.05

X3.3015

G32 Z-10.35 F2.

G0 X4.615

Z1.05

X3.2975

G32 Z-10.35 F2.

G0 X4.615

Z1.05

X3.2935

G32 Z-10.35 F2.

G0 X4.615

Z1.05

X3.2895

G32 Z-10.35 F2.

G0 X4.615

Z1.05

X3.2855

G32 Z-10.35 F2.

G0 X4.615

Z1.05

X3.2815

G32 Z-10.35 F2.

G0 X4.615

Z1.05

X3.2775

G32 Z-10.35 F2.

G0 X4.615

Z1.05

X3.2735

G32 Z-10.35 F2.

G0 X4.615

Z1.05

X3.2695

G32 Z-10.35 F2.

G0 X4.615

Z1.05

X3.2655

G32 Z-10.35 F2.

G0 X4.615

Z1.05

X3.2614

G32 Z-10.35 F2.

G0 X4.615

Z1.05

X3.2574

G32 Z-10.35 F2.

G0 X4.615

Z1.05

X3.2534

G32 Z-10.35 F2.

G0 X4.615

Z1.05

X3.2494

G32 Z-10.35 F2.

G0 X4.615

Z1.05

X3.2454

G32 Z-10.35 F2.

G0 X4.615

Z1.05

X3.2414

G32 Z-10.35 F2.

G0 X4.615

Z1.05

X3.2374

G32 Z-10.35 F2.

G0 X4.615

Z1.05

X3.2334

G32 Z-10.35 F2.

G0 X4.615

Z1.05

X3.2294

G32 Z-10.35 F2.

G0 X4.615

Z1.05

X3.2254

G32 Z-10.35 F2.

G0 X4.615

Z1.05

X3.2214

G32 Z-10.35 F2.

G0 X4.615

Z1.05

X3.2174

G32 Z-10.35 F2.

G0 X4.615

Z1.05

X3.2134

G32 Z-10.35 F2.

G0 X4.615

Z1.05

X3.2094

G32 Z-10.35 F2.

G0 X4.615

Z1.05

X3.2054

G32 Z-10.35 F2.

G0 X4.615

Z1.05

X3.2014

G32 Z-10.35 F2.

G0 X4.615

Z1.05

X3.1974

G32 Z-10.35 F2.

G0 X4.615

Z1.05

X3.1934

G32 Z-10.35 F2.

G0 X4.615

Z1.05

X3.1894

G32 Z-10.35 F2.

G0 X4.615

Z1.05

X3.1854

G32 Z-10.35 F2.

G0 X4.615

Z1.05

X3.1814

G32 Z-10.35 F2.

G0 X4.615

Z1.05

X3.1774

G32 Z-10.35 F2.

G0 X4.615

Z1.05

X3.1733

G32 Z-10.35 F2.

G0 X4.615

Z1.05

X3.1693

G32 Z-10.35 F2.

G0 X4.615

Z1.05

X3.1653

G32 Z-10.35 F2.

G0 X4.615

Z1.05

X3.1613

G32 Z-10.35 F2.

G0 X4.615

Z1.05

X3.1573

G32 Z-10.35 F2.

G0 X4.615

Z1.05

X3.1533

G32 Z-10.35 F2.

G0 X4.615

Z1.05

X3.1493

G32 Z-10.35 F2.

G0 X4.615

Z1.05

X3.1453

G32 Z-10.35 F2.

G0 X4.615

Z1.05

X3.1413

G32 Z-10.35 F2.

G0 X4.615

Z1.05

X3.1373

G32 Z-10.35 F2.

G0 X4.615

Z1.05

X3.1333

G32 Z-10.35 F2.

G0 X4.615

Z1.05

X3.1293

G32 Z-10.35 F2.

G0 X4.615

Z1.05

X3.1253

G32 Z-10.35 F2.

G0 X4.615

Z1.05

X3.1213

G32 Z-10.35 F2.

G0 X4.615

Z1.05

X3.1173

G32 Z-10.35 F2.

G0 X4.615

Z1.05

X3.1133

G32 Z-10.35 F2.

G0 X4.615

Z1.05

X3.1093

G32 Z-10.35 F2.

G0 X4.615

Z1.05

X3.1053

G32 Z-10.35 F2.

G0 X4.615

Z1.05

X3.1013

G32 Z-10.35 F2.

G0 X4.615

Z1.05

X3.0973

G32 Z-10.35 F2.

G0 X4.615

Z1.05

X3.0933

G32 Z-10.35 F2.

G0 X4.615

Z1.05

X3.0892

G32 Z-10.35 F2.

G0 X4.615

Z1.05

X3.0852

G32 Z-10.35 F2.

G0 X4.615

Z1.05

X3.0812

G32 Z-10.35 F2.

G0 X4.615

Z1.05

X3.0772

G32 Z-10.35 F2.

G0 X4.615

Z1.05

X3.0732

G32 Z-10.35 F2.

G0 X4.615

Z1.05

X3.0692

G32 Z-10.35 F2.

G0 X4.615

Z1.05

X3.0652

G32 Z-10.35 F2.

G0 X4.615

Z1.05

X3.0612

G32 Z-10.35 F2.

G0 X4.615

Z1.05

X3.0572

G32 Z-10.35 F2.

G0 X4.615

Z1.05

X3.0532

G32 Z-10.35 F2.

G0 X4.615

Z1.05

X3.0492

G32 Z-10.35 F2.

G0 X4.615

Z1.05

X3.0452

G32 Z-10.35 F2.

G0 X4.615

Z1.05

X3.0412

G32 Z-10.35 F2.

G0 X4.615

Z1.05

X3.0372

G32 Z-10.35 F2.

G0 X4.615

Z1.05

X3.0332

G32 Z-10.35 F2.

G0 X4.615

Z1.05

X3.0292

G32 Z-10.35 F2.

G0 X4.615

Z1.05

X3.0252

G32 Z-10.35 F2.

G0 X4.615

Z1.05

X3.0212

G32 Z-10.35 F2.

G0 X4.615

Z1.05

X3.0172

G32 Z-10.35 F2.

G0 X4.615

Z1.05

X3.0132

G32 Z-10.35 F2.

G0 X4.615

Z1.05

X3.0092

G32 Z-10.35 F2.

G0 X4.615

Z1.05

X3.0052

G32 Z-10.35 F2.

G0 X4.615

Z1.05

X3.0011

G32 Z-10.35 F2.

G0 X4.615

Z1.05

X2.9971

G32 Z-10.35 F2.

G0 X4.615

Z1.05

X2.9931

G32 Z-10.35 F2.

G0 X4.615

Z1.05

X2.9891

G32 Z-10.35 F2.

G0 X4.615

Z1.05

X2.9851

G32 Z-10.35 F2.

G0 X4.615

Z1.05

X2.9811

G32 Z-10.35 F2.

G0 X4.615

Z1.05

X2.9771

G32 Z-10.35 F2.

G0 X4.615

Z1.05

X2.9731

G32 Z-10.35 F2.

G0 X4.615

Z1.05

X2.9691

G32 Z-10.35 F2.

G0 X4.615

Z1.05

X2.9651

G32 Z-10.35 F2.

G0 X4.615

Z1.05

X2.9611

G32 Z-10.35 F2.

G0 X4.615

Z1.05

X2.9571

G32 Z-10.35 F2.

G0 X4.615

Z1.05

X2.9531

G32 Z-10.35 F2.

G0 X4.615

Z1.05

X2.9491

G32 Z-10.35 F2.

G0 X4.615

Z1.05

X2.9451

G32 Z-10.35 F2.

G0 X4.615

Z1.05

X2.9411

G32 Z-10.35 F2.

G0 X4.615

Z1.05

X2.9371

G32 Z-10.35 F2.

G0 X4.615

Z1.05

X2.9331

G32 Z-10.35 F2.

G0 X4.615

Z1.05

X2.9291

G32 Z-10.35 F2.

G0 X4.615

Z1.05

X2.9251

G32 Z-10.35 F2.

G0 X4.615

Z1.05

X2.9211

G32 Z-10.35 F2.

G0 X4.615

Z1.05

X2.9171

G32 Z-10.35 F2.

G0 X4.615

Z1.05

X2.913

G32 Z-10.35 F2.

G0 X4.615

Z1.05

X2.909

G32 Z-10.35 F2.

G0 X4.615

Z1.05

X2.905

G32 Z-10.35 F2.

G0 X4.615

Z1.05

X2.901

G32 Z-10.35 F2.

G0 X4.615

Z1.05

X2.897	X2.861	X2.8249
G32 Z-10.35 F2.	G32 Z-10.35 F2.	G32 Z-10.35 F2.
G0 X4.615	G0 X4.615	G0 X4.615
Z1.05	Z1.05	Z1.05
X2.893	X2.857	X2.8209
G32 Z-10.35 F2.	G32 Z-10.35 F2.	G32 Z-10.35 F2.
G0 X4.615	G0 X4.615	G0 X4.615
Z1.05	Z1.05	Z1.05
X2.889	X2.853	X2.8169
G32 Z-10.35 F2.	G32 Z-10.35 F2.	G32 Z-10.35 F2.
G0 X4.615	G0 X4.615	G0 X4.615
Z1.05	Z1.05	Z1.05
X2.885	X2.849	X2.8129
G32 Z-10.35 F2.	G32 Z-10.35 F2.	G32 Z-10.35 F2.
G0 X4.615	G0 X4.615	G0 X4.615
Z1.05	Z1.05	Z1.05
X2.881	X2.845	X2.8089
G32 Z-10.35 F2.	G32 Z-10.35 F2.	G32 Z-10.35 F2.
G0 X4.615	G0 X4.615	G0 X4.615
Z1.05	Z1.05	Z1.05
X2.877	X2.841	X2.8049
G32 Z-10.35 F2.	G32 Z-10.35 F2.	G32 Z-10.35 F2.
G0 X4.615	G0 X4.615	G0 X4.615
Z1.05	Z1.05	Z1.05
X2.873	X2.837	X2.8009
G32 Z-10.35 F2.	G32 Z-10.35 F2.	G32 Z-10.35 F2.
G0 X4.615	G0 X4.615	G0 X4.615
Z1.05	Z1.05	Z1.05
X2.869	X2.833	X2.7969
G32 Z-10.35 F2.	G32 Z-10.35 F2.	G32 Z-10.35 F2.
G0 X4.615	G0 X4.615	G0 X4.615
Z1.05	Z1.05	Z1.05
X2.865	X2.829	X2.7929
G32 Z-10.35 F2.	G32 Z-10.35 F2.	G32 Z-10.35 F2.
G0 X4.615	G0 X4.615	G0 X4.615
Z1.05	Z1.05	Z1.05

X2.7889

G32 Z-10.35 F2.

G0 X4.615

Z1.05

X2.7849

G32 Z-10.35 F2.

G0 X4.615

Z1.05

X2.7809

G32 Z-10.35 F2.

G0 X4.615

Z1.05

X2.7769

G32 Z-10.35 F2.

G0 X4.615

Z1.05

X2.7729

G32 Z-10.35 F2.

G0 X4.615

Z1.05

X2.7689

G32 Z-10.35 F2.

G0 X4.615

Z1.05

X2.7649

G32 Z-10.35 F2.

G0 X4.615

Z1.05

X2.7609

G32 Z-10.35 F2.

G0 X4.615

Z1.05

X2.7569

G32 Z-10.35 F2.

G0 X4.615

Z1.05

X2.7529

G32 Z-10.35 F2.

G0 X4.615

Z1.05

X2.7489

G32 Z-10.35 F2.

G0 X4.615

Z1.05

X2.7449

G32 Z-10.35 F2.

G0 X4.615

Z1.05

X2.7408

G32 Z-10.35 F2.

G0 X4.615

Z1.05

X2.7368

G32 Z-10.35 F2.

G0 X4.615

Z1.05

X2.7328

G32 Z-10.35 F2.

G0 X4.615

Z1.05

X2.7288

G32 Z-10.35 F2.

G0 X4.615

Z1.05

X2.7248

G32 Z-10.35 F2.

G0 X4.615

Z1.05

X2.7208

G32 Z-10.35 F2.

G0 X4.615

Z1.05

X2.7168

G32 Z-10.35 F2.

G0 X4.615

Z1.05

X2.7128

G32 Z-10.35 F2.

G0 X4.615

Z1.05

X2.7088

G32 Z-10.35 F2.

G0 X4.615

Z1.05

X2.7048

G32 Z-10.35 F2.

G0 X4.615

Z1.05

X2.7008

G32 Z-10.35 F2.

G0 X4.615

Z1.05

X2.6968

G32 Z-10.35 F2.

G0 X4.615

Z1.05

X2.6928

G32 Z-10.35 F2.

G0 X4.615

Z1.05

X2.6888

G32 Z-10.35 F2.

G0 X4.615

Z1.05

X2.6848

G32 Z-10.35 F2.

G0 X4.615

Z1.05

X2.6808

G32 Z-10.35 F2.

G0 X4.615

Z1.05

X2.6768

G32 Z-10.35 F2.

G0 X4.615

Z1.05

X2.6728

G32 Z-10.35 F2.

G0 X4.615

Z1.05

X2.6688

G32 Z-10.35 F2.

G0 X4.615

Z1.05

X2.6648

G32 Z-10.35 F2.

G0 X4.615

Z1.05

X2.6608

G32 Z-10.35 F2.

G0 X4.615

Z1.05

X2.6568

G32 Z-10.35 F2.

G0 X4.615

Z1.05

X2.6527

G32 Z-10.35 F2.

G0 X4.615

Z1.05

X2.6487

G32 Z-10.35 F2.

G0 X4.615

Z1.05

X2.6447

G32 Z-10.35 F2.

G0 X4.615

Z1.05

X2.6407

G32 Z-10.35 F2.

G0 X4.615

Z1.05

X2.6367

G32 Z-10.35 F2.

G0 X4.615

Z1.05

X2.6327

G32 Z-10.35 F2.

G0 X4.615

Z1.05

X2.6287

G32 Z-10.35 F2.

G0 X4.615

Z1.05

X2.6247

G32 Z-10.35 F2.

G0 X4.615

Z1.05

X2.6207

G32 Z-10.35 F2.

G0 X4.615

Z1.05

X2.6167

G32 Z-10.35 F2.

G0 X4.615

Z1.05

X2.6127

G32 Z-10.35 F2.

G0 X4.615

Z1.05

X2.6087

G32 Z-10.35 F2.

G0 X4.615

Z1.05

X2.6047

G32 Z-10.35 F2.

G0 X4.615

Z1.05

X2.6007

G32 Z-10.35 F2.

G0 X4.615

Z1.05

X2.5967

G32 Z-10.35 F2.

G0 X4.615

Z1.05

X2.5927

G32 Z-10.35 F2.

G0 X4.615

Z1.05

X2.5887

G32 Z-10.35 F2.

G0 X4.615

Z1.05

X2.5847

G32 Z-10.35 F2.

G0 X4.615

Z1.05

X2.5807

G32 Z-10.35 F2.

G0 X4.615

Z1.05

X2.5767

G32 Z-10.35 F2.

G0 X4.615

Z1.05

X2.5727

G32 Z-10.35 F2.

G0 X4.615

Z1.05

X2.5687

G32 Z-10.35 F2.

G0 X4.615

Z1.05

X2.5646

G32 Z-10.35 F2.

G0 X4.615

Z1.05

X2.5606

G32 Z-10.35 F2.

G0 X4.615

Z1.05

X2.5566

G32 Z-10.35 F2.

G0 X4.615

Z1.05

X2.5526

G32 Z-10.35 F2.

G0 X4.615

Z1.05

X2.5486

G32 Z-10.35 F2.

G0 X4.615

Z1.05

X2.5446

G32 Z-10.35 F2.

G0 X4.615

Z1.05

X2.5406

G32 Z-10.35 F2.

G0 X4.615

Z1.05

X2.5366

G32 Z-10.35 F2.

G0 X4.615

Z1.05

X2.5326

G32 Z-10.35 F2.

G0 X4.615

Z1.05

X2.5286

G32 Z-10.35 F2.

G0 X4.615

Z1.05

X2.5246

G32 Z-10.35 F2.

G0 X4.615

Z1.05

X2.5206

G32 Z-10.35 F2.

G0 X4.615

Z1.05

X2.5166

G32 Z-10.35 F2.

G0 X4.615

Z1.05

X2.5126

G32 Z-10.35 F2.

G0 X4.615

Z1.05

X2.5086

G32 Z-10.35 F2.

G0 X4.615

Z1.05

X2.5046

G32 Z-10.35 F2.

G0 X4.615

Z1.05

X2.5006

G32 Z-10.35 F2.

G0 X4.615

Z1.05

X2.4966

G32 Z-10.35 F2.

G0 X4.615

Z1.05

X2.4926

G32 Z-10.35 F2.

G0 X4.615

Z1.05

X2.4886

G32 Z-10.35 F2.

G0 X4.615

Z1.05

X2.4846

G32 Z-10.35 F2.

G0 X4.615

Z1.05

X2.4806

G32 Z-10.35 F2.

G0 X4.615

Z1.05

X2.4765

G32 Z-10.35 F2.

G0 X4.615

Z1.05

X2.4725

G32 Z-10.35 F2.

G0 X4.615

Z1.05

X2.4685

G32 Z-10.35 F2.

G0 X4.615

Z1.05

X2.4645

G32 Z-10.35 F2.

G0 X4.615

Z1.05

X2.4605

G32 Z-10.35 F2.

G0 X4.615

Z1.05

X2.4565

G32 Z-10.35 F2.

G0 X4.615

Z1.05

X2.4525

G32 Z-10.35 F2.

G0 X4.615

Z1.05

X2.4485

G32 Z-10.35 F2.

G0 X4.615

Z1.05

X2.4445

G32 Z-10.35 F2.

G0 X4.615

Z1.05

X2.4405

G32 Z-10.35 F2.

G0 X4.615

Z1.05

X2.4365

G32 Z-10.35 F2.

G0 X4.615

Z1.05

X2.4325

G32 Z-10.35 F2.

G0 X4.615

Z1.05

X2.4285

G32 Z-10.35 F2.

G0 X4.615

Z1.05

X2.4245

G32 Z-10.35 F2.

G0 X4.615

Z1.05

X2.4205

G32 Z-10.35 F2.

G0 X4.615

Z1.05

X2.4165

G32 Z-10.35 F2.

G0 X4.615

Z1.05

X2.4125

G32 Z-10.35 F2.

G0 X4.615

Z1.05

X2.4085

G32 Z-10.35 F2.

G0 X4.615

Z1.05

X2.4045

G32 Z-10.35 F2.

G0 X4.615

Z1.05

X2.4005

G32 Z-10.35 F2.

G0 X4.615

Z1.05

X2.3965

G32 Z-10.35 F2.

G0 X4.615

Z1.05

X2.3925

G32 Z-10.35 F2.

G0 X4.615

Z1.05

X2.3884

G32 Z-10.35 F2.

G0 X4.615

Z1.05

X2.3844

G32 Z-10.35 F2.

G0 X4.615

Z1.05

X2.3804

G32 Z-10.35 F2.

G0 X4.615

Z1.05

X2.3764

G32 Z-10.35 F2.

G0 X4.615

Z1.05

X2.3724

G32 Z-10.35 F2.

G0 X4.615

Z1.05

X2.3684

G32 Z-10.35 F2.

G0 X4.615

Z1.05

X2.3644

G32 Z-10.35 F2.

G0 X4.615

Z1.05

X2.3604

G32 Z-10.35 F2.

G0 X4.615

Z1.05

X2.3564

G32 Z-10.35 F2.

G0 X4.615

Z1.05

X2.3524

G32 Z-10.35 F2.

G0 X4.615

Z1.05

X2.3484

G32 Z-10.35 F2.

G0 X4.615

Z1.05

X2.3444

G32 Z-10.35 F2.

G0 X4.615

Z1.05

X2.3404

G32 Z-10.35 F2.

G0 X4.615

Z1.05

X2.3364

G32 Z-10.35 F2.

G0 X4.615

Z1.05

X2.3324

G32 Z-10.35 F2.

G0 X4.615

Z1.05

X2.3284

G32 Z-10.35 F2.

G0 X4.615

Z1.05

X2.3244

G32 Z-10.35 F2.

G0 X4.615

Z1.05

X2.3204

G32 Z-10.35 F2.

G0 X4.615

Z1.05

X2.3164

G32 Z-10.35 F2.

G0 X4.615

Z1.05

X2.3124

G32 Z-10.35 F2.

G0 X4.615

Z1.05

X2.3084

G32 Z-10.35 F2.

G0 X4.615

Z1.05

X2.3043

G32 Z-10.35 F2.

G0 X4.615

Z1.05

X2.3003

G32 Z-10.35 F2.

G0 X4.615

Z1.05

X2.2963

G32 Z-10.35 F2.

G0 X4.615

Z1.05

X2.2923

G32 Z-10.35 F2.

G0 X4.615

Z1.05

X2.2883

G32 Z-10.35 F2.

G0 X4.615

Z1.05

X2.2843

G32 Z-10.35 F2.

G0 X4.615

Z1.05

X2.2803

G32 Z-10.35 F2.

G0 X4.615

Z1.05

X2.2763

G32 Z-10.35 F2.

G0 X4.615

Z1.05

X2.2723

G32 Z-10.35 F2.

G0 X4.615

Z1.05

X2.2683

G32 Z-10.35 F2.

G0 X4.615

Z1.05

X2.2643

G32 Z-10.35 F2.

G0 X4.615

Z1.05

X2.2603

G32 Z-10.35 F2.

G0 X4.615

Z1.05

X2.2563

G32 Z-10.35 F2.

G0 X4.615

Z1.05

X2.2523

G32 Z-10.35 F2.

G0 X4.615

Z1.05

X2.2483

G32 Z-10.35 F2.

G0 X4.615

Z1.05

X2.2443

G32 Z-10.35 F2.

G0 X4.615

Z1.05

X2.2403

G32 Z-10.35 F2.

G0 X4.615

Z1.05

X2.2363

G32 Z-10.35 F2.

G0 X4.615

Z1.05

X2.2323

G32 Z-10.35 F2.

G0 X4.615

Z1.05

X2.2283

G32 Z-10.35 F2.

G0 X4.615

Z1.05

X2.2243

G32 Z-10.35 F2.

G0 X4.615

Z1.05

X2.2203

G32 Z-10.35 F2.

G0 X4.615

Z1.05

X2.2162

G32 Z-10.35 F2.

G0 X4.615

Z1.05

X2.2122

G32 Z-10.35 F2.

G0 X4.615

Z1.05

X2.2082

G32 Z-10.35 F2.

G0 X4.615

Z1.05

X2.2042

G32 Z-10.35 F2.

G0 X4.615

Z1.05

X2.2002

G32 Z-10.35 F2.

G0 X4.615

Z1.05

X2.1962

G32 Z-10.35 F2.

G0 X4.615

Z1.05

X2.1922

G32 Z-10.35 F2.

G0 X4.615

Z1.05

X2.1882

G32 Z-10.35 F2.

G0 X4.615

Z1.05

X2.1842

G32 Z-10.35 F2.

G0 X4.615

Z1.05

X2.1802

G32 Z-10.35 F2.

G0 X4.615

Z1.05

X2.1762

G32 Z-10.35 F2.

G0 X4.615

Z1.05

X2.1722

G32 Z-10.35 F2.

G0 X4.615

Z1.05

X2.1682

G32 Z-10.35 F2.

G0 X4.615

Z1.05

X2.1642

G32 Z-10.35 F2.

G0 X4.615

Z1.05

X2.1602

G32 Z-10.35 F2.

G0 X4.615

Z1.05

X2.1562

G32 Z-10.35 F2.

G0 X4.615

Z1.05

X2.1522

G32 Z-10.35 F2.

G0 X4.615

Z1.05

X2.1482

G32 Z-10.35 F2.

G0 X4.615

Z1.05

X2.1442

G32 Z-10.35 F2.

G0 X4.615

Z1.05

X2.1402

G32 Z-10.35 F2.

G0 X4.615

Z1.05

X2.1362

G32 Z-10.35 F2.

G0 X4.615

Z1.05

X2.1322

G32 Z-10.35 F2.

G0 X4.615

Z1.05

X2.1281

G32 Z-10.35 F2.

G0 X4.615

Z1.05

X2.1241

G32 Z-10.35 F2.

G0 X4.615

Z1.05

X2.1201

G32 Z-10.35 F2.

G0 X4.615

Z1.05

X2.1161

G32 Z-10.35 F2.

G0 X4.615

Z1.05

X2.1121

G32 Z-10.35 F2.

G0 X4.615

Z1.05

X2.1081

G32 Z-10.35 F2.

G0 X4.615

Z1.05

X2.1041

G32 Z-10.35 F2.

G0 X4.615

Z1.05

X2.1001

G32 Z-10.35 F2.

G0 X4.615

Z1.05

X2.0961

G32 Z-10.35 F2.

G0 X4.615

Z1.05

X2.0921

G32 Z-10.35 F2.

G0 X4.615

Z1.05

X2.0881

G32 Z-10.35 F2.

G0 X4.615

Z1.05

X2.0841

G32 Z-10.35 F2.

G0 X4.615

Z1.05

X2.0801

G32 Z-10.35 F2.

G0 X4.615

Z1.05

X2.0761

G32 Z-10.35 F2.

G0 X4.615

Z1.05

X2.0721

G32 Z-10.35 F2.

G0 X4.615

Z1.05

X2.0681

G32 Z-10.35 F2.

G0 X4.615

Z1.05

X2.0641

G32 Z-10.35 F2.

G0 X4.615

Z1.05

X2.0601

G32 Z-10.35 F2.

G0 X4.615

Z1.05

X2.0561

G32 Z-10.35 F2.

G0 X4.615

Z1.05

X2.0521

G32 Z-10.35 F2.

G0 X4.615

Z1.05

X2.0481

G32 Z-10.35 F2.

G0 X4.615

Z1.05

X2.0441

G32 Z-10.35 F2.

G0 X4.615

Z1.05

X2.04

G32 Z-10.35 F2.

G0 X4.615

Z1.05

X2.036

G32 Z-10.35 F2.

G0 X4.615

Z1.05

X2.032

G32 Z-10.35 F2.

G0 X4.615

Z1.05

X2.028

G32 Z-10.35 F2.

G0 X4.615

Z1.05

X2.024

G32 Z-10.35 F2.

G0 X4.615

Z1.05

X2.02

G32 Z-10.35 F2.

G0 X4.615

Z1.05

X2.016

G32 Z-10.35 F2.

G0 X4.615

Z1.05

X2.012

G32 Z-10.35 F2.

G0 X4.615

Z1.05

X2.008

G32 Z-10.35 F2.

G0 X4.615

Z1.05

X2.004

G32 Z-10.35 F2.

G0 X4.615

Z1.05

X2.

G32 Z-10.35 F2.

G0 X4.615

Z1.05

X2.

G32 Z-10.35 F2.

G0 X4.615

Z1.05

M9

G28 U0. W0. M05

T100

M30

# 13. Appendix D: CVAP Reactor Process Flow Diagram
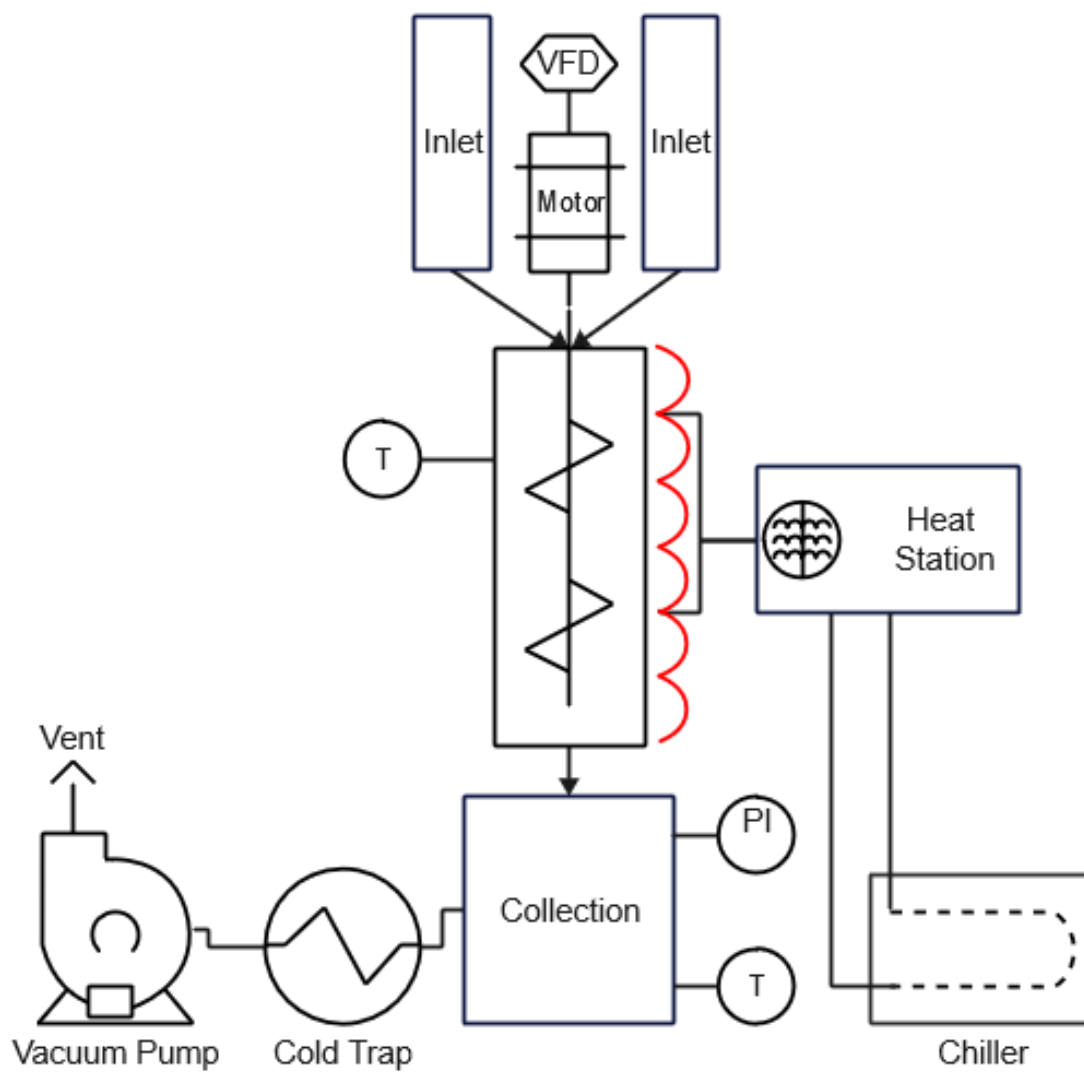
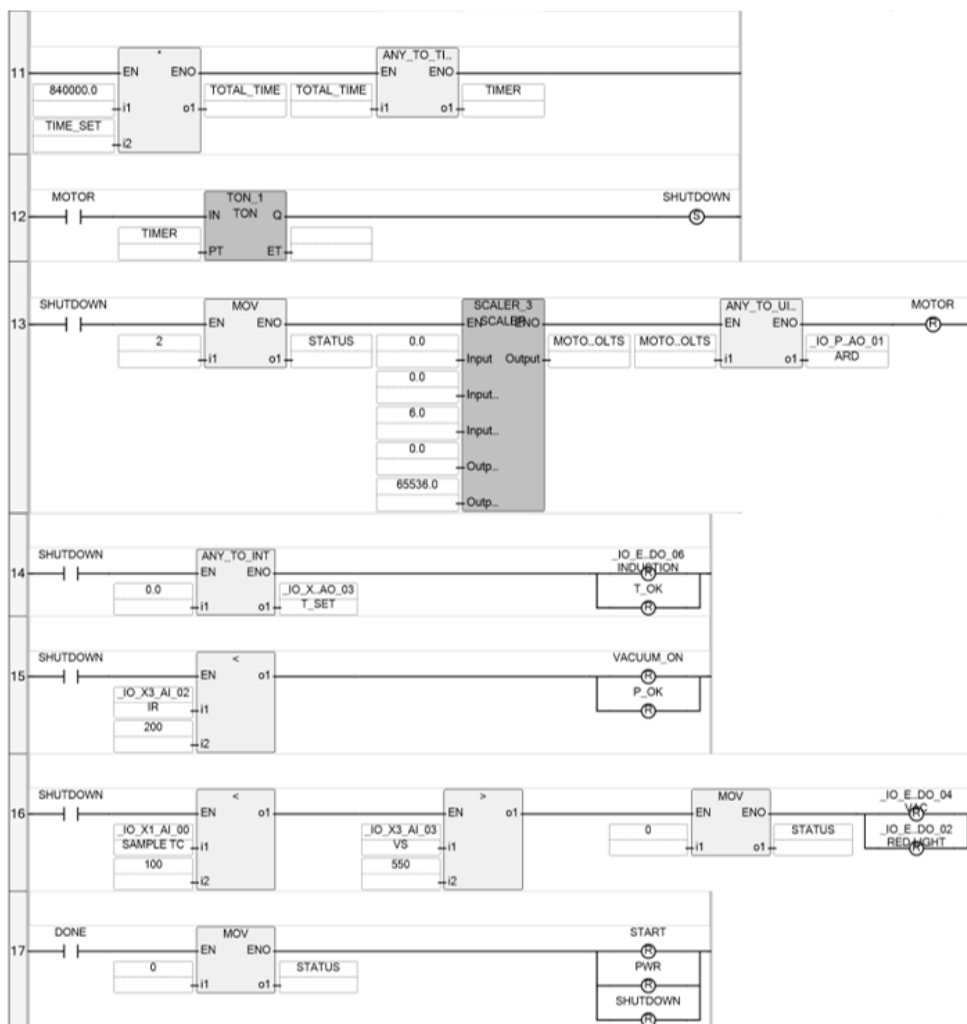# 14. Appendix E: CVAP Reactor Wiring Diagram
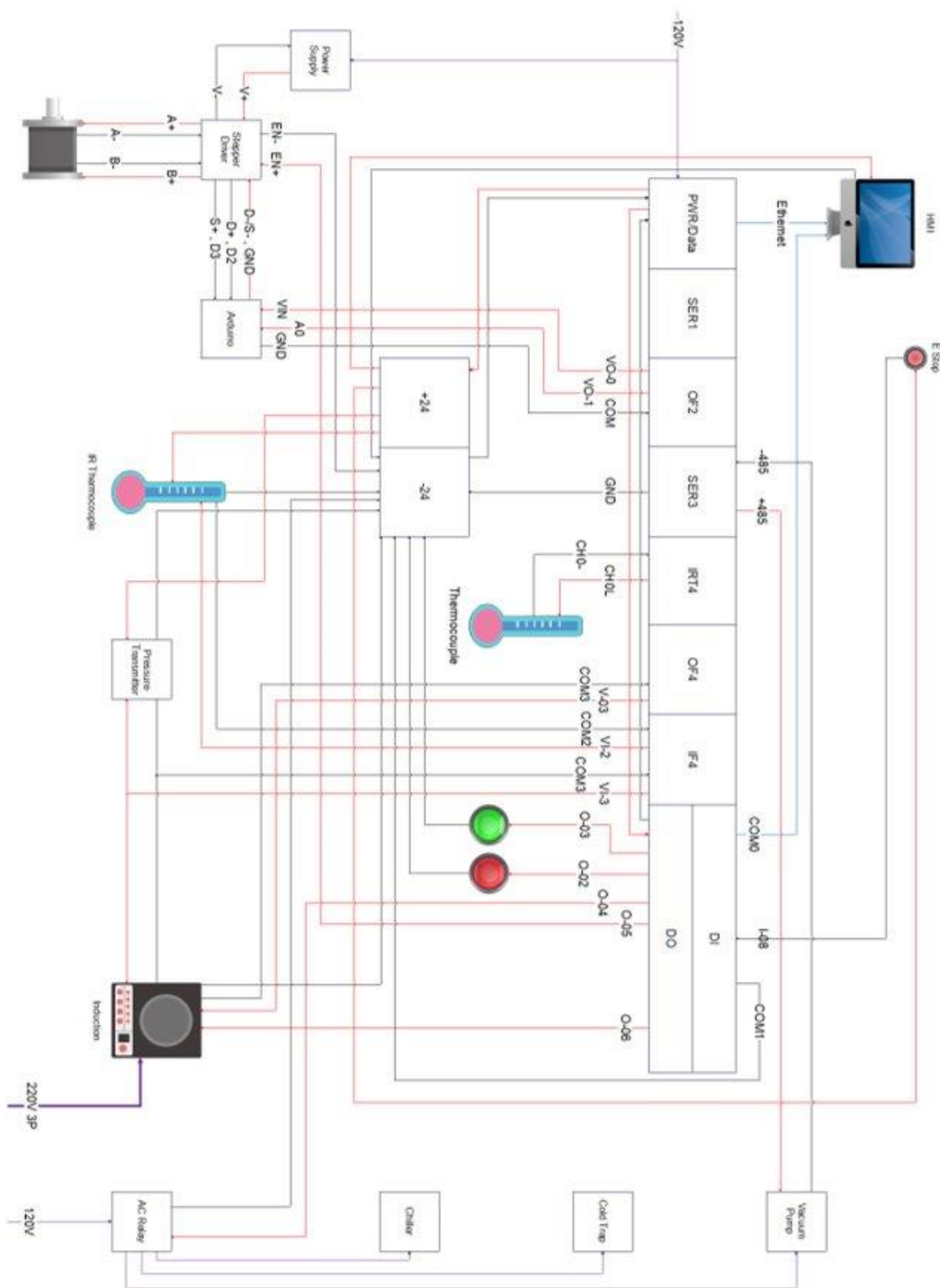
15. Appendix F: CVAP Reactor Automation Logic

Automation logic for the CVAP reactor was formulated in the open-source program

Connected Components Workbench. Two ladder logic diagrams were constructed to facilitate

the operation of the sensing components and furnace components, respectively.
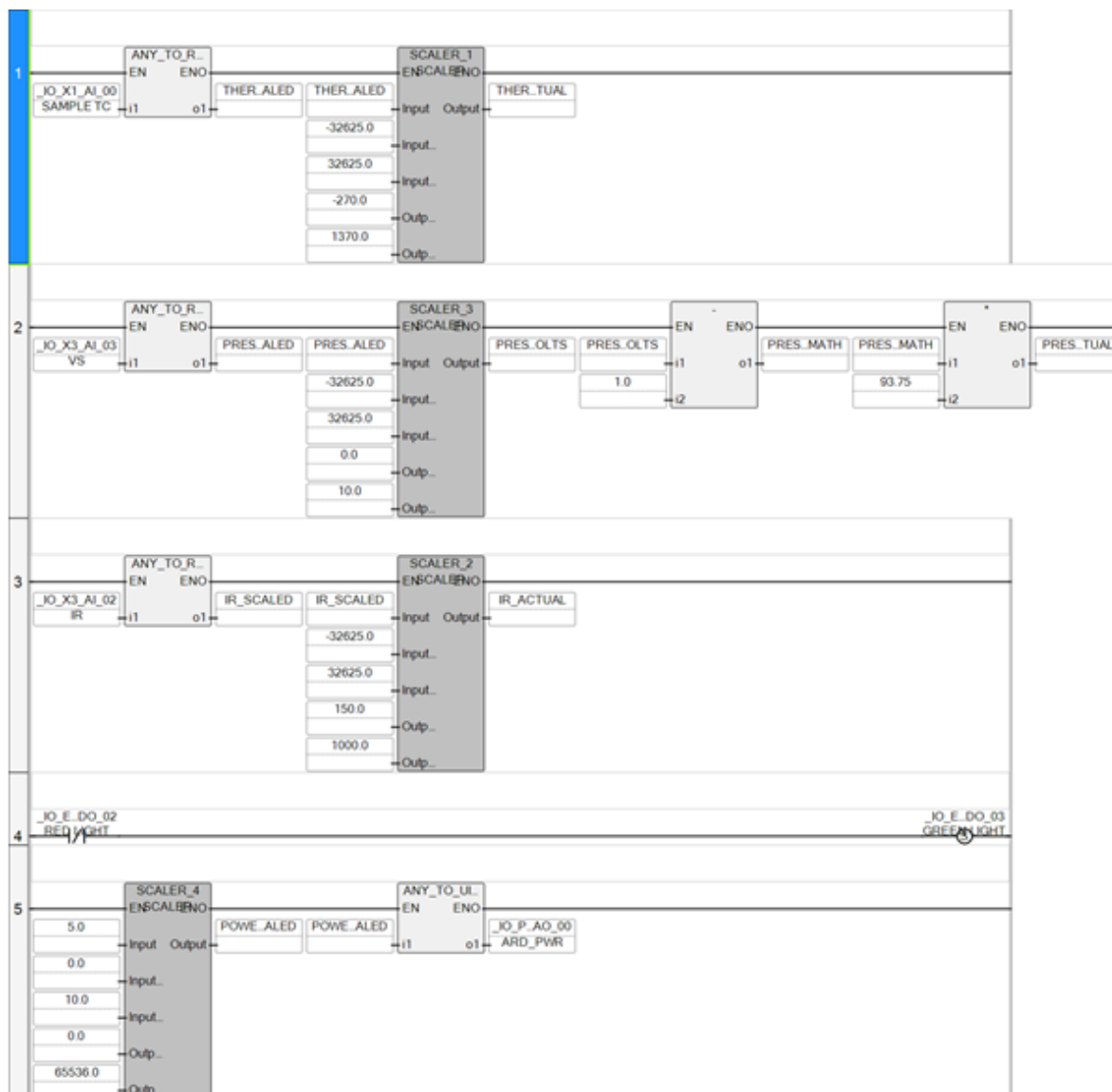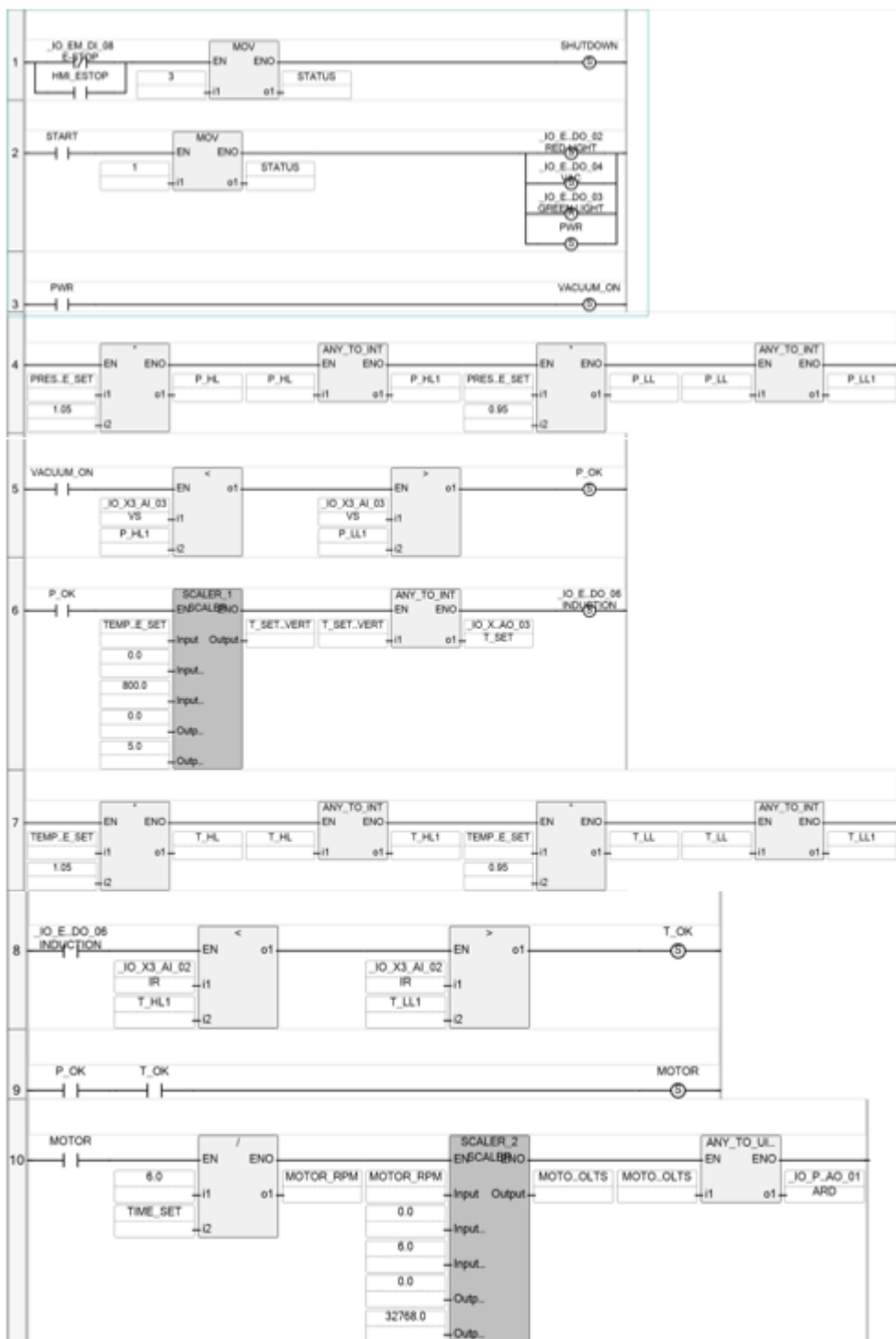
16.   Appendix G: CVAP Reactor Standard Operating Procedure

CVAP Reactor Operation Manual

Rev. June 30, 2023

HMI process data readings are in Celsius (temperature), Torr (pressure), and minutes (time).
Please wear safety glasses and rubber gloves when operating the furnace or changing sample.

1. Ensure that the GREEN status light is illuminated before proceeding.
2. Open the front door of the fume hood and the hinged panel above the inlet hoppers.
3. Fill the inlet hoppers equally to the fill line.
4. Close the inlet hopper lids, latching in numerical order and ensuring a uniform coating of vacuum grease on the gaskets.
5. Remove the front panel of the collection bin, placing a suitable vessel inside for collection.
6. Close the collection, tightening the sealing nuts and ensuring a uniform coating of vacuum grease on the gasket.
7. Ensure that the fluid level in the recirculating chiller is to the FULL mark.
8. Ensure that the coil in the cold trap bath is fully submerged in ethylene glycol.
9. Ensure that the glass cold traps are empty and sealed.
10. Close and latch the front door of the fume hood, then close the hinged panel above the inlet hoppers.
11. Enter the desired operating conditions into the HMI parameter screen.
12. Press the POWER button to start the furnace program.

     Depress the physical or virtual E-STOP buttons in the event of an emergency

13. During operation, the system status is displayed in the dialog box at the bottom of the HMI.
14. When the furnace program has ended, the dialog box will display "SYSTEM IDLE" and the GREEN status light will illuminate.
15. Open the front door of the fume hood and the hinged panel above the inlet hoppers.
16. Open the inlet hopper lids and remove any excess feedstock with a vacuum or compressed air.
17. Open the collection bin and remove the sample.
18. Close the collection bin and inlet hoppers, ensuring that all residues from the process are removed.
19. Remove all collected material from the glass cold traps.
20. Inspect the plumbing for blockages and/or solid buildup.
21. Ensure that the fume hood is clean and dust-free before closing the front door and hinged panel.
22. Record operating conditions, date, approximate solid yield and other pertinent experimental data in the instrument logbook.
23. If maintenance is required, please inform the instrument manager.
24. Press the FINISH and DONE buttons to reset the automation code.